Role of Surface Plasmon Resonance in Solar Light Harvesting

Thesis Submitted to AcSIR For the Award of the Degree of
DOCTOR OF PHILOSOPHY
In Chemical Sciences

By
Kshirodra Kumar Patra
Registration Number **10CC12J26021**

Under the guidance of
Dr. Chinnakonda S. Gopinath

Catalysis Division
CSIR-National Chemical Laboratory
Pune-411008, India.

Certificate

This is to certify that the work incorporated in this Ph.D. thesis entitled "***Role of Surface Plasmon Resonance in Solar Light Harvesting***" submitted by Mr. ***Kshirodra Kumar Patra*** to Academy of Scientific and Innovative Research (AcSIR) in fulfillment of the requirements for the award of the Degree of **Doctor Of Philosophy** in Chemical Sciences embodies original research work under my supervision. I further certify that this work has not been submitted to any other University or Institution in part or full for the award of any degree or diploma. Research material obtained from other sources has been duly acknowledged in the thesis. Any text, illustration, table etc., used in the thesis from other sources, have been duly cited and acknowledged.

Kshirodra K Patra
(Student)

Kshirodra Kumar Patra

C. S. Gopi
(Supervisor)

Dr C. S. Gopinath

DECLARATION

I hereby declare that the thesis entitled "***Role of Surface Plasmon Resonance in Solar Light Harvesting***" submitted for the degree of **Doctor of Philosophy** in **Chemical Science** to the Acedemy of Scientific and Innovative Research (AcSIR) has been carried out by me at the Catalysis Division of CSIR – National Chemical Laboratory, Pune under the guidance of **Dr. Chinnakonda. S. Gopinath**. Such material as has been obtained by other sources has been duly acknowledged in this thesis. The work is original and has not been submitted in part or full by me for any other degree to any other Institution or University.

Kshirodra Kumar Patra

CSIR – National Chemical Laboratory

Pune - 411008

Kshirodra Kumar Patra

Dedicated to my mother

Sarojinee

Acknowledgments

I wish to express my profound obligation and deepest gratitude to my supervisor Dr. Chinnakonda S. Gopinath, a true gentleman who inspire me to dream more, learn more and do more. Without his supervision and constant help this thesis would not have been possible.

I would like to thanks my Doctoral Advisory Committee Members Dr. T. G. Ajithkumar, Dr. S. Mayadevi, Dr. S. A. R. Mulla and Dr. E. Balaraman for their timely help and suggestions.

I would like to thank Dr. C. P. Vinod and Dr. T. Raja for their encouragement and support. I am also thankful to Dr. D. Srinivas, Chairman, Catalysis Division and Dr. A. P. Singh, (former Chairman, Catalysis Division) for their extended support.

I thank Prof. A. K. Nangia, Director, and Dr. S. Pal, Former Director, CSIR-National Chemical Laboratory for their approval to carry out my research work, and extending all infrastructural facilities. I am also thankful to Academy of Scientific and Innovative Research (AcSIR) for giving me a chance to submit this work in the form of a thesis for the award of PhD degree.

I thank all the nonteaching staffs of CSIR-NCL for their assistance on various occasions. I also thank all divisional staff members, particularly Mr Madhu for his support.

I wish to thank all my friends and cooperative labmates Drs. Edwin, Sivaranjani, Kanak (Bhai), Deva (the dangerous), Thushara, Anjani, Sanjay, RajaAmbal, Ashwin, Sadhu, Anand, Naresh (Swati mam), Sheetal, Ashok Patil, Naveen, Pradnya, Ruchi, Manoj, Prabhu,Jino, Kavya, Jyoti, Manisha, Hasna, Femi, Madhu bhai, Shilpa, Sreejith, Maheshwari, Nitin, Ravi and Himanshu. They were extremely supportive as well as helpful during my tenure. Especially I am very much thankful to project students, particularly Bela, Sreeya, Vanshika, Swati and Sharan who helped me in various projects.

A very special gratitude goes to Ms. Ruchi Jain, who helped me a lot during my PhD.

I would like to thanks Ashok, Sunil, Vysakh, Manikandan, Yogita, Aswathy, Preeti and Sharad for the association in an extended group.

I express my heartfelt thanks to my friends from Orissa Raju, Chaka, Jitu, Mandakini, Puspanjali, Siva, Manoj Sumanta, Prajna, Sibaddatta, and Gitanjali.

I would like to thank Sudhakar, Rangarajan, Arunava and Ramsunder for helping me in various characterization techniques like IPCE, PL, Electrchemical and UV measurement.

I always cherish the memories of the times spent in TT room with my friends Manoj Sharma, Kundan, Arun, Anup (TT man), Raju, Chaka, Jitu, Deepak, Deepak Kumar, and Anil.

I do not have words to express my feelings to my Maa, sister Pinky, dada Tulu and family members. Their blessing, love and inspiration provide me through moral and emotional support in my life.

I am grateful to UGC, New Delhi, for awarding the research fellowship. Also I thank the TAPSUN program (NWP-0056 project) for providing many facilities.

Finally I dedicated everything to lord Siva for his enormous blessings.

Kshirodra Kumar Patra

Lists of Abbreviations

QuAL	Quasi Artificial Leaf
XPS	X-ray Photoelectron Spectroscopy
UVPES	Ultraviolet Photoelectron Spectroscopy
APPES	Ambient Pressure Photoelectron Spectroscopy
LSPR	Localized Surface Plasmon Resonance
SPR	Surface Plasmon Resonance
SPP	Surface Plasmon Polarization
SWS	Solar Water Splitting
DET	Direct Electron Transfer
PIRET	Plasmon Induced Resonance Energy Transfer
DSSC	Dye Sensitized Solar Cell
PEC	Photo-Electrochemical Measurement
SEM	Scanning Electron Microscope
TEM	Transmission Electron Microscope
SAED	Selected Area Electron Diffraction
AQY	Apparent Quantum Yield
PL	Photoluminescence
XRD	X-ray diffraction
HER	Hydrogen Evolution Rate
GO	Graphene oxide
mGO	mildly Oxidized Graphite
IPCE	Incident Photon to Current Conversion Effeciency
PEC	Photon to Energy Conversion
QD	Quantum Dot

CONTENTS

CHAPTER 1 1

1.1 Photocatalytic water splitting 2

1.2 Plasmonic nanostructures for solar water splitting 5

1.2.1. Schottky junction and direct electron transfer (DET) 7

1.2.2. Near field electromagnetic and scattering mechanism 8

1.2.3. Plasmon resonant energy transfer 10

1.3 Role of co-catalyst in solar water splitting 11

1.3.1. Fundamentals of electrocatalytic HER 11

1.3.2. Parameters for catalyst activity comparison 14

1.4 Thin film approach for solar water splitting 15

1.5 Quasi-artificial leaf approach for solar hydrogen generation 17

1.6 Objective of thesis 20

1.7 Outline of the thesis 21

References 22

CHAPTER 2 25

2.1 Introduction 26

2.2 Synthesis of catalyst 26

2.2.1 Preparation of AgAuT composite 26

2.2.2 Preparation of AgT-AuNR 27

2.2.3 Synthesis of $AuTiO_2$ by deposition precipitation method 28

2.2.4 Synthesis of $AuTiO_2$ by physical mixture method 28

2.2.5 Synthesis of NiCu bimetallic nanoparticles 28

2.2.6 Synthesis of MoS_2-mGO composite 29

2.3 Fabrication of Devices 29

2.3.1 Fabrication of $AuTiO_2$ base DSSC 29
2.3.2 Fabrication of $AuTiO_2$/PbS/CdS photoanode for for QuAL device 30
2.3.3 Fabrication of wireless photochemical cell for TiO_2/PbS/CdS with NiCu catalyst 32
2.4 Structural Characterization Methods 32
2.5 Photochemical (PEC) measurements 33
2.6 Electrochemical Characterization 34
2.6.1 Electrochemical characterization of $AuTiO_2$ based DSSC 34
2.6.2 Electrochemical characterization of NiCu catalyst 34
2.6.3 Electrochemical characterization of MoS_2-mGO catalyst 34
2.7 H_2 evolution in the wired and wireless configuration 35
2.8 H_2 evolution in wireless device with NICu 35
References 35

CHAPTER 3 37

Part A: Bimetallic and Plasmonic Ag-Au on TiO_2 for Solar Water Splitting: An Active Nanocomposite for Entire Visible Light Region Absorption
3.1 Introduction 38
3.2 Results and Discussion 39
3.2.1 UV-Visible absorption studies 39
3.2.2 PEC measurement 41
3.2.3 Photocatalytic Hydrogen evolution 42
3.2.4 Photoluminescene studies 45
3.2.5 Raman studies 46
3.2.6 TEM Studies 47
3.2.7 XPS 50
3.3 Mechanism 51
3.4 Conclusion 52
Part B: Harnessing Near IR and Visible Light Photons Through Plasmon Effect of Gold Nanoroads with $AgTiO_2$
3.5 Introduction 53
3.6 Result and Discussion 55

3.6.1 UV-Vis Spectra 55
3.6.2 TEM Analysis 57
3.6.3 Raman Spectroscopy 60
3.6.4 XPS 61
3.6.5 Photocatalytic activity 62
3.6.6 PEC Measurement 66
3.7 Mechanism 67
3.8 Conclusion 68
Part C: Well interconnected $AuTiO_2$ an potential candidate for high efficiency Dye sensitized Solar cell: Role of Au LSPR on the efficiency of DSSC
3.9 Introduction 70
3.10 Result and Discussion 71
3.10.1 UV-VIS Spectra 71
3.10.2 TEM Studies 72
3.10.3 Raman Spectroscopy 73
3.10.4 DSSC Measurement 74
3.10.5 Impedance Spectroscopy 75
3.11 Conclusion 76
References 77

CHAPTER 4 81

Part A: Possibly scalable Solar Hydrogen generation with Quasi-Artificial leaf approach
4.1 Introduction 82
4.2 Result and Discussion. 83
4.2.1 Structural and Spectral characterization 83
4.2.2 UV-Visible Spectroscopy 87
4.2.3 Photocatalytic H_2 evolution from QuAL device 88
4.2.4 Photoelectrochemical measurement 90
4.3 Mechanism 94
4.4 Conclusion 95

Part B: Quasi Artificial Leaf for Solar Hydrogen Generation with Earth Abundant Co-Catalyst

4.5 Introduction 97

4.6 Results and Discussion. 98

4.6.1 XRD 98

4.6.2 X-ray photoelectron spectroscopy 99

4.6.3 Ultra-Violet photoelectron spectroscopy 100

4.6.4 Electrochemically- measured HER activity 101

4.6.5 Photocatalytic Hydrogen evolution 102

4.7 Conclusion 104

Part C: The Photocatalytic and Co-Catalytic behavior of MoS_2-mild oxidized Graphite (MoS_2-mGO) nanocomposite on a TiO_2/PbS/CdS Quasi Artificial leaf for Solar Hydrogen production: The dula role MoS_2-mGO

4.8 Introduction 105

4.9 Results and Discussion 106

4.9.1 Optical properties of MoS_2-mGO composite 106

4.9.2 XRD 108

4.9.3 Raman spectroscopy 109

4.9.4 XPS 110

4.9.5 TEM 112

4.9.6 Electrocatalytic HER Activity of MoS_2-mGO composites 112

4.9.7 Photocatalytic HER activity of MoS_2-mGO composites 114

4.10 Mechanism of photocatalytic HER 115

4.11 Conclusion 116

References 116

CHAPTER 5 119

Conclusions and future scope of work 120

PREFACE

***Chapter 1*:** Solar energy conversion to chemical energy or power generation is and will be very likely to remain as one of the attractive and sustainable solutions to the global energy problems. It is expected that photocatalytic water splitting will become a promising method for solar light harvesting towards the production of carbon free or carbon neutral clean fuel such as hydrogen, and reduction of CO_2 to fuels/chemicals. Among many semiconductors TiO_2 is the most extensively studied semiconductor due to it wide band gap nature and well positioned valence and conduction band for oxidation and reduction half reaction of water, respectively. The recent development of plasmonic metal semiconductor nano composite has given a new direction to the photovoltaic and photocatalytic application where charge carrier can be generated on semiconductor surface through decay of localized surface plasmon. Recently nanocrystal of Au, Ag, Cu which interact strongly with visible light photon due to localized surface plasmon resonance (LSPR) has been considered as a photosensitizer. It has been proved that charge carrier can be either injected directly to the conduction band of semiconductor through decay of surface plasmon, which formed hot electron or some part of energy may be transferred through radiative energy transfer, thereby improving the performance of semiconductor in the visible region. Another attraction of plasmonic NPs which makes them so special from other class of material is the shape and size dependent optical properties.

Chapter 2: Various methods employed to prepare nanogold, nanosilver, titania and several other semiconductors are described in this chapter. SILAR (successive ionic layer adsorption and reaction) is an important method to prepare chalcogenide semiconductors within the pores of titania. Relevant characterization methods have been employed to understand the structural, spectroscopy, microscopy and electronic structure aspects. These methods are briefly described in this chapter.

***Chapter 3a*:** A combination of Ag + Au nanoclusters would broaden the visible light absorption at least between 400 and 650 nm. This hypothesis was evaluated through solar water splitting (SWS) activity of Au-TiO_2, Ag-TiO_2 and Ag on Au-TiO_2 (AgAuT) composites. AgAuT bimetal nanocomposite shows the maximum apparent quantum yield (AQY) of 3.3 % with hydrogen generation (718 μmol/h.g) from aqueous methanol, and overall water splitting activity (7

μmol/g.h, AQY= 0.04%) under one sun conditions. Enhanced photocatalytic activity of AgAuT is partly attributed to the formation of hot electrons. Thin layer of Ag coating on Au particles makes it as core-shell morphology with Au in the core. Fermi level equilibration between metal and titania, and Schottky junction formation is directly demonstrated. The strong electronic interaction between Ag and Au, and with TiO_2 is evident from its electron rich character and ascertained from Raman spectroscopy, XPS, photoluminescence, and HRTEM measurements

***Chapter 3b*:** Longitudinal plasmon resonance of AuNR in AgT-AuNR was observed and it induces photocatalytic hydrogen generation between λ = 550- 800 nm; whereas TiO_2-AuNR shows no activity in this wavelength range .The key aspect for achieving high photocatalytic activity in the visible light is the electronic integration among metal NPs and with TiO_2, and the heterojunctions among them. The utilization of the blue, green and red light for solar water splitting has been reported in a single plasmonic nanocomposite.

***Chapter 3c*:** The role of LSPR on the efficiency of dye sensitized solar cell (DSSC) was investigated..Highly interconnected 4 μm-thick Au-TiO_2 photo anode was demonstrated to show power conversion efficiency of 7.2 % with open-circuit photovoltage (V_{oc}) of 686 mV and a current density (J_{sc}) of 14.1 $mAcm^{-2}$.

***Chapter 4a*:** Here we report a wireless device comprising Au-TiO_2 electrode sensitized by a PbS/CdS quantum dots (QDs).The direct coupling of the gold nanoparticles (Au NPs) to TiO_2 surface enhance the hydrogen production in QDs sensitized photoanode. The LSPR effect of the AuNPs and QDs sensitization lead to a photocurrent of 4.3 mA/cm^2 at 0 V (vs Ag/AgCl), leading to 12 ml H_2 h^{-1} g^{-1} generation in a wireless configuration. The photo anode produces power conversion efficiency (PCE) of 5.6 % in the wireless configuration.

***Chapter 4b*:** In this part, we report a TiO_2-PbS/CdS based wireless electrochemical device, sensitized by PbS/CdS quantum dots; NiCu bimetallic nanoparticles as a cocatalyst was demonstrated to show significant H_2 generation activity in artificial leaf system .

***Chapter 4c*:** Recently, the implantation of non-noble-metal electrocatalysts into photocatalysts has dramatically improved hydrogen evolution activity. In this work we have introduced MoS_2-

RGO both as a cocatalyst and visible light photocatalyst in the quasi artificial leaf device. Here we have shown that it is the electrocatalytic process on MoS_2-RGO combine with light absorbing quantum dots, which plays the critical role for efficient solar H_2 production.

Chapter 5: Conclusions reached from chapters 3 and 4 are briefly described. In our opinion, significant fundamental understanding as well as large amount of applied research is required to reap the full benefit of solar harvesting through water splitting.

List of Publication

1. **Patra, K. K**.; Bhuskute, B. D.; and Gopinath, C. S., Possibly Scalable Solar Hydrogen Generation with Quasi-Artificial Leaf Approach. *Sci Rep* 2017, *7*, 6515.
2. **Patra, K. K** and Gopinath, C. S., Bimetallic and Plasmonic Ag-Au on TiO_2 for Solar Water Splitting : An Active Nanocomposite for Entire Visible Light Region Absorption, ChemCatChem., 2016, 8, 3294 - 3311
3. **Patra, K. K** and Gopinath, C. S., Harnessing Near IR and Visible Light Photons through Plasmon Effect of Gold Nanorods with $AgTiO_2$(submitted)
4. **Patra, K. K** , Bharad P. A. and Gopinath, C. S Quasi Artificial Leaf for Solar Hydrogen Generation with Earth Abundant Co-Catalyst. (To be submitted)
5. **Patra, K. K,** Kattungal S. R., and Gopinath, C. S Photocatalytic and Cocatalytic Behavior of MoS_2-mild Oxidized Graphite (MoS_2-mGO) Nanocomposite on a TiO_2/PbS/CdS Quasi Artificial Leaf for Solar Hydrogen Production: Dual Role of MoS_2-mGO. (To be submitted)

Introduction

Introduction

1.1 Photocatalytic water splitting

It is indispensable to find out a way for generating clean energy to solve the energy and environmental issues. In this regard, undoubtedly, hydrogen is the ultimate source of clean energy. Presently hydrogen produced from fossil fuel by steam reforming in petrochemical industries and in this process, invariably, a large amount of CO_2 is added to the environment, which is already at the level of more than 400 ppm CO_2. Therefore, if we consider the energy and environmental issues, hydrogen has to be produced from the natural (or renewable) sources of energy such as sunlight, biomass. There are many ways for solar hydrogen production such as

(1) Photoelectrochemical water splitting
(2) Electrolysis of water using solar cell
(3) Photocatalytic water splitting (Artificial photosynthesis).

Many metal oxides are well known for photocatalysis reaction. Among all transition metal oxide, TiO_2 is widely used, due to its stability and environmental friendly nature.[1,2] It has been extensively used in a variety of application such as photovoltaic, photocatalytic water splitting, water purification, white pigment in paints and cosmetics.[3] Titanium dioxide exist in three different types of crystal structures namely a) anatase b) rutile and c) brookite. The unit cell crystal structure of TiO_2 is shown in Figure 1.1.[4]

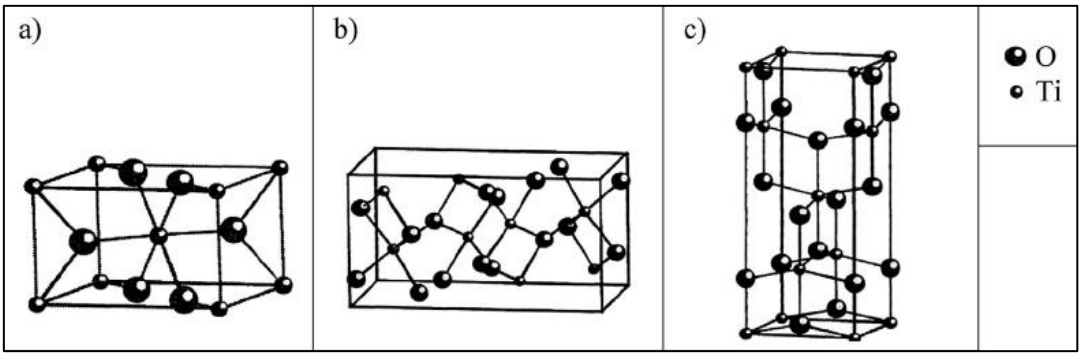

Figure 1.1: Unit cell crystal structures of a) rutile, b) anatase, and (c) brookite TiO_2. (Reproduced with permission from Elsevier, Netherlands).

The brookite structure is built up of distorted octahedra with a titanium ion at the center and oxygen ions at each of the six vertices. Each octahedron shares three edges with adjoining octahedra, forming an orthorhombic structure. Brookite is the least stable crystal form in TiO_2 and shows an orthorhombic crystal structure. Anatase and rutile is the stable form of TiO_2 and shows distorted octahedron crystalline structure. It is also to be noted that while rutile is thermodynamically stable, anatase phase is not so. Rutile shows slight orthorhombic octahedral distortion, whereas in anatase the distortion is more. In rutile structure, each octahedron is surrounded with 10 neighboring octahedron with two edge sharing oxygen pairs and eight corner sharing oxygen atoms, whereas in anatase it is eight neighbors with four edge sharing and four corner sharing oxygen. It is also to be mentioned that rutile is compact with high density (), while anatase () is significantly lower in density. Both anatase and rutile are stable in water and hence perfectly suitable for water splitting photocatalysis.

Water splitting reaction, where hydrogen and oxygen are evolved, is an attractive and highly challenging reaction due to large positive Gibbs free energy change associated with it.[5] In photoelectrochemical water splitting we need external potential and in electrolysis of water, we need a solar cell to split the water. However in photocatalytic water splitting, sunlight or simulated sunlight shines on the photocatalyst dispersed in water and then hydrogen is liberated from the solution as shown in Figure 1.2.[5] Hence photocatalytic water splitting will be advantageous for large scale production of hydrogen. The reaction is similar to photosynthesis by plants and therefore regarded as artificial photosynthesis. The photocatalyst are mostly semiconductor and TiO_2 has been extensively studied for this reaction.

Honda and Fujishima, first demonstrated the water splitting using TiO_2 as a working electrode and Pt as the counter electrode in an electrochemical system under an applied potential.[6] When TiO_2 is irradiated with UV light, electron and hole pairs generated at the respective conduction band valence band, respectively. The photogenerated electron flows towards the counter electrode to reduce water to hydrogen and holes oxidized water to form oxygen by applied external potential. However materials which execute both half reactions efficiently under sunlight or visible light irradiation at no applied potential is yet to be discovered. Hence search for visible light active water splitting catalyst with high efficiency and sustainability is very much open.

An efficient photocatalyst (Fig. 1.2b) need to meet the following requirements: (1) absorb solar light in the entire UV-Visible and possibly near IR regions of the solar spectrum; (2) suitable band edge position to perform oxidation and reduction half reactions; (3) easy separation of electron-hole pairs and their transfer to semiconductor-liquid junction where they perform the half reactions; (d) catalyst also should exhibit high efficiency of at least 10 % quantum yield and sustainability for year or at least months.[7] However, unfortunately none of the semiconductor satisfies all the property as shown in Figure 1.3.[8] For example, many n-type semiconductors, like

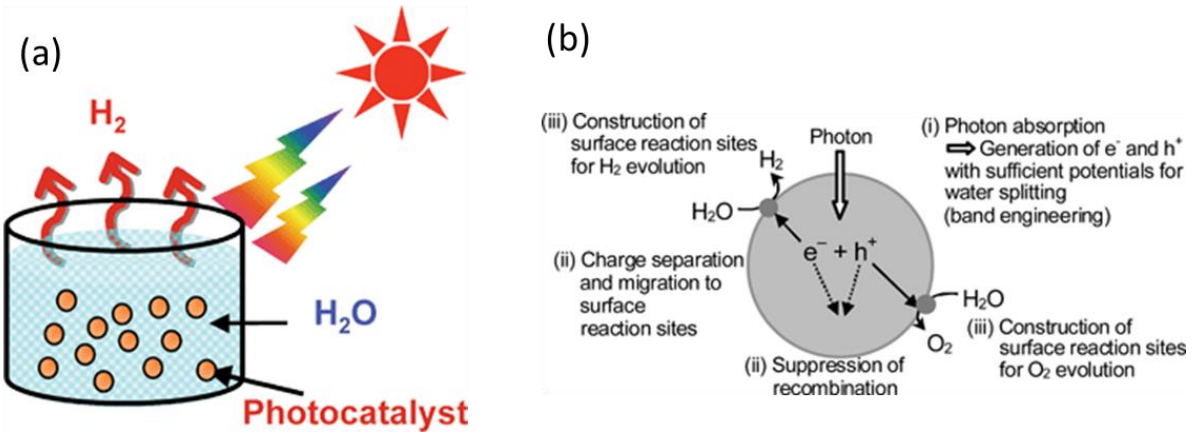

Figure 1.2: (a) Photocatalytic hydrogen evolution from water using a powder photocatalyst with sunlight. (b) Three steps involved in any typical photocatalysis, and the figure explains the water splitting photocatalysis. (Reproduced with permission from RSC).

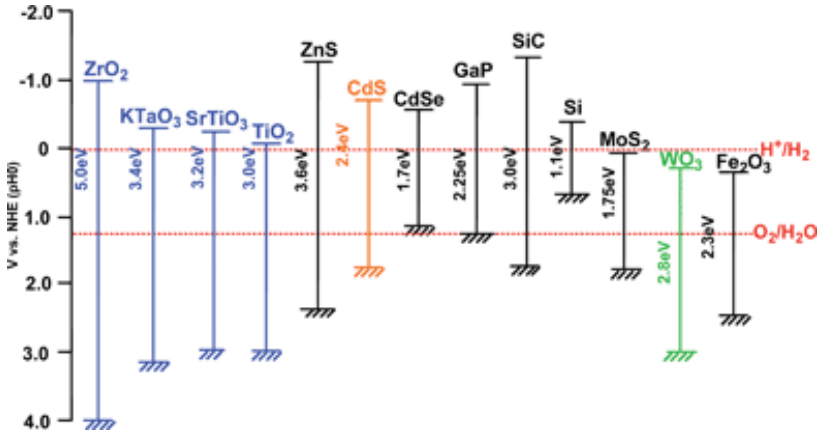

Figure 1.3: Band edges potential of various semiconductors with respect to NHE. (Reproduced with permission from RSC).

TiO_2, exhibit suitable band edge potentials for water reduction, but the light absorption is limited to only UV region of the solar spectrum due to wide band gap of 3.2 eV. Semiconductors, like Si and GaN nanowires, absorb in the visible region and show excellent mobility of charge carries, however, exhibits poor catalytic activity.[9]

Many strategies have been developed to modify the semiconductor such as semiconductor cocatalyst system, where cocatalyst provides the active sites for the reaction. Pt is the well-known cocatalyst due to it low over potential for hydrogen evolution reaction (HER).[10] Although semiconductor/cocatalyst system exhibited improved catalytic activity as compared to only semiconductor, this approach does not address the problems of (1) absorption limited to only high energy photons and (2) minority charge carrier diffusion length.[7] Recently it has been demonstrated that, this problems can be partially resolved by using plasmonic nanostructure embedded in semiconductor matrix. A number of reports showed that the plasmonic metal NPs/semiconductor composites exhibited higher photocatalytic activity as compared to its only semiconductor counterparts.[11] The unique characteristic of this composite, which is responsible for enhanced photocatalytic activity, is the metal surface plasmon resonance (SPR). At least for the last one decade, it has been demonstrated that metal nanostructure of mainly Ag and Au shows SPR effect in the presence of visible light.[12,13]

1.2. Plasmonic nanostructures for solar water splitting

Surface plasmon is an optical phenomenon and it was first demonstrated by Michael Faraday in 1857.[14] However, it did not attract any significant attention from the scientific community at that time. Recently the concept of surface plasmon re-appeared and has been used in many applications, such as catalysis, imaging, sensing, solar cell and electronic.[15,16] Plasmon effect also enhances the intensity of Raman modes of molecules adsorbed on plasmonic metal surfaces.[17] Among a variety of applications, recently plasmonic nanostructure has been used extensively in photocatalytic water splitting. Surface plasmon can be described as the coherent oscillation of conduction band electrons in a metal particle surface which are excited by the electromagnetic field of the incident light. In surface plasmon resonance, metal nanostructures serve as antennas to convert light to localized electric fields at the metal-dielectric interface as shown in Figure 1.4.[17,18]

There are two modes of SPR based on the geometry of the metal surface, namely, surface plasmon polaritons (SPP) and localized surface plasmon resonance (LSPR).[17b] SPP occurs in the case of metal foil and nanowires, where the metal nanostructure is much larger than the wavelength of the incident light. This plasmon usually propagates tens of hundreds micrometers along the metal surface.[19] LSPR occurs in the case of metal nanostructures where the size is

Figure 1.4: Surface plasmon resonance in the presence of visible light.

much smaller than the wave length of incident light (Figure 1.5). In the presence of external electromagnetic field, the electron clouds in the conduction band of metal nanostructure oscillate with certain frequency due to the polarization of the electron cloud. When the electrons cloud oscillation frequency resonate with a certain frequency-range of incident light, a strong oscillation of electrons will be observed as shown in Figure 1.5. This is due to light absorption by plasmon surfaces. Much of interest has been given to Au and Ag nanostructure because their LSPR occurs in the visible light of the solar spectrum.[20] The LSPR effect depends on many factors like, (1) density of conduction band electrons, (2) refractive index of the surrounding medium, and (3) shape and size of the metal nanostructure.[21] Hence by manipulating the composition, shape and size of the plasmonic nanostructure, it is possible to design such plasmonic nanocomposite which will harvest the maximum solar light from UV, visible and possibly near IR region.

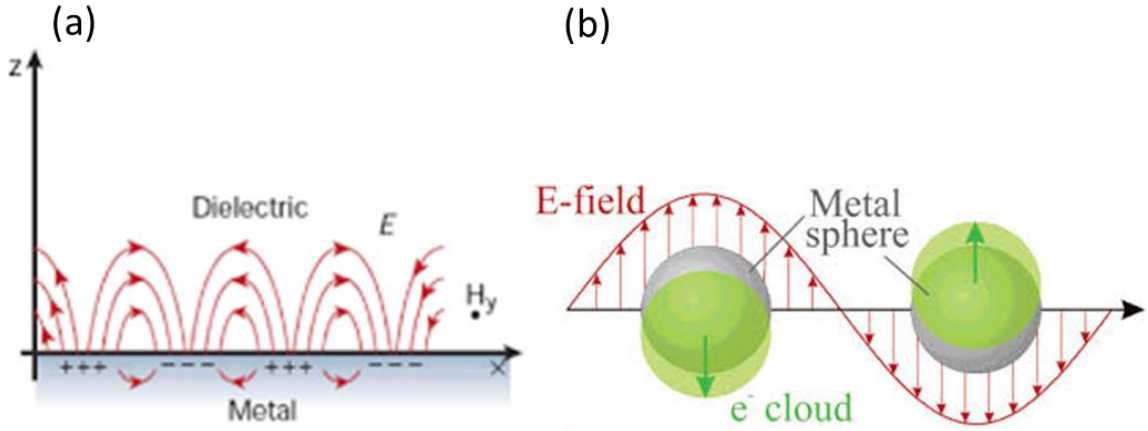

Figure 1.5: (a) SPP occurs where the metal nanostructure is much larger than the wavelength of incident light. (b) LSPR occurs in the case of metal nanostructures where the size is much smaller than the wave length of incident light.

Generally SPR refers to LSPR in the plasmonic photocatalysis or solar light harvesting applications, unless it is noted. A unique characteristic of semiconductor/plasmonic nanostructure composite photocatalyst is the wavelength dependent photocatalytic activity. Many studies have been carried out in numerous semiconductors for oxygen evolution and hydrogen evolution half reactions, where enhancement in activity was observed in the metal nanostructure SPR region. This indicates that SPR plays an important role in enhancing the rate of photocatalytic reaction on nearby semiconductors. Cronin and co-workers studied the oxygen evolution reaction on an $AuTiO_2$ composite and achieve fivefold enhancement in photocurrent density as compared to TiO_2 under visible light.[22] The metallic SPR enhance the photocatalytic activity in the nearby semiconductor by transferring energy associated with SPR to the semiconductor, which increase the concentration of charge carriers in the semiconductors. There are three exclusive energy transfer mechanism, by which the charge carriers concentration increases on the semiconductor adjacent to plasmonic nanostructures and are discussed below.

1.2.1. Schottky junction and direct electron transfer (DET)

When an n-type semiconductor like TiO_2 is in contact with metal nanoparticles of Ag or Au, it forms a Schottky junction at the interface.[11a,c] Generally, noble metals like Ag and Au have high work function and the Fermi levels of these metals NPs is located below the conduction band of TiO_2. In composites material of $AuTiO_2$ or $AgTiO_2$, a Schottky junction (or

barrier) is formed, when the metal NPs is in direct contact with TiO_2. Thus electrons diffuse from TiO_2 to Au and forms a positively charge region in TiO_2. Meanwhile a negatively charged region is created on the Au side. Hence an electric field is created at the interface, which prevents the electro-hole pairs from recombination upon irradiated with visible light. As the Au and titania are brought together, the bands in the titania bend such that the titania's work function (Φ) matches that of gold. The bands retain their bending upon contact. In direct electron transfer (DET) process the charge carriers are directly injected into the semiconductor conduction band at the Schottky junction and it is analogous to the dye sensitization process.[23] In dye sensitization process, dye molecules anchored on TiO_2 surface absorb the light and transfer the electron to the TiO_2 conduction band. The plasmonic nanoparticles act as a sensitizer and transfer the energetic electron to the nearby semiconductor through the excitation of SPR. Another important characteristic feature of plasmonic nanostructure of Ag and Au are excellent mobility of charge carriers and high absorption cross section. It has been calculated that, the absorption cross section of a plasmonic NPs is around 10^5 times higher than that up a typical dye molecule.[24] It is worth noting that, most of the semiconductor used for water splitting have conduction band at a potential around -1.0 to 0 V with respect to the normal hydrogen electrode (NHE), as shown in Figure 1.3. The SPR energy for plasmonic NPs lies between 1 to 4 eV with respect to Fermi level.[7] In other words, the energetic electron formed during SPR excitation will be in this energy window. The Fermi level of metal NPs is around 0 V vs NHE. Hence the alignment of SPR state and conduction band potential is suitable for the transfer of energetic electrons from metal to semiconductor. A schematic representation of the DET has been shown in Figure 1.6.

1.2.2. Near field electromagnetic and scattering mechanism

The enhancement in photocatalytic activity was also observed in many semiconductor/plasmonic nanostructure, where the metal is not in direct contact with semiconductor. In this type of composite materials, the activity increases due to radiative energy transfer from metal SPR to semiconductor, which take place through a near field electromagnetic and scattering mechanism. This mechanism is based on the interaction of the SPR induced electric field with the nearby semiconductor. Generally the magnitude of SPR induced electric field is much higher than the electric field of photons. The intensity of the electric field is highest at the surface of NPs and

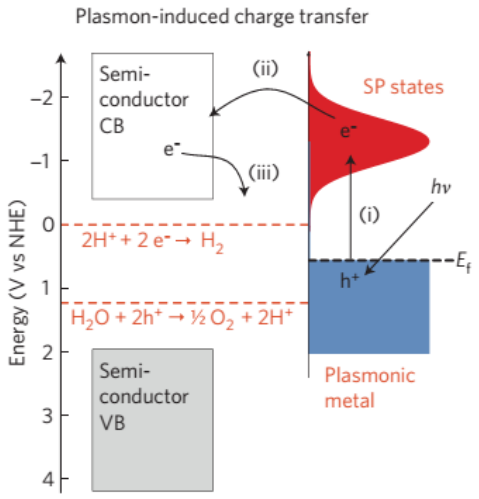

Figure 1.6: Mechanism of SPR induced direct electron transfer from plasmonic metal NPs to semiconductor conduction band. (Reproduce with permission from Nature publication).

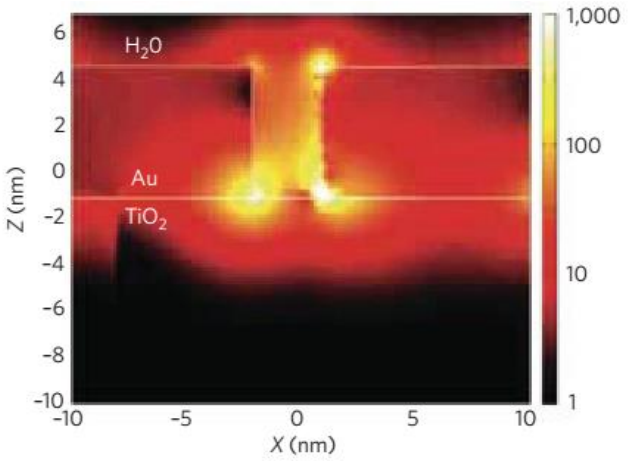

Figure 1.7 Optical simulation shows the interaction of SPR induced electric field with nearby TiO_2 NPs. (Reproduce with permission from Nature publication).

decreases exponentially with distance from the surface. Hence, when a semiconductor is brought in to the proximity of photo excited plasmonic nanostructure, it encounters the intense field. As a result, electron-hole pair formation take place on the semiconductor surface because of the intense electric field. The concentration of the charge carriers depends on the intensity of the induced electric field. Another advantage of using plasmonic nanostructure is that the SPR induced electron-hole pair formation is the highest at the semiconductor/liquid interface, where the half reactions take place. The concept of the near field effect can be understood by optical simulation method. Figure 1.7, shows the optical simulation of $AuTiO_2$, where the Au LSPR interacts with the TiO_2 surface.[25,26,7] The near field effect of the Au LSPR decreases drastically as the distance increases from the surface .

The scattering of resonant photons, which generally occurs in plasmonic nanostructures of more than 50 nm, also plays a role in enhancing the photoctatalytic activity. The scattering of photons results in the increase in average photon path length in the plasmonic nanostructure composites.

1.2.3. Plasmon resonant energy transfer

Resonant energy transfer (RET) refers to a non-radiative energy transfer process, whereas near field enhancement mechanism is a radiative process. When the dipole moment of the electron-hole pair of the semiconductor, coupled with the plsmonic dipole moment of the excited noble metal, results in the plasmon resonant energy transfer. Hence the necessary condition for the RET process is, the bandgap of the semiconductor should overlap with the LSPR band of the plasmonic nanostructure. The near field enhancement mechanism occurs, only when the energy of the SPR state is higher than the band gap energy. The PIRET process can generate electron-hole pair on the nearby semiconductor below and above the band gap due to non-radiative coupling. Unlike DET, RET is not affected by, whether the semiconductor is in direct contact with the plasmonic nanostructure or not. RET process directly excite the electron- hole pair in the nearby semiconductor through the relaxation of localize surface plasmon dipole and it is very similar to Forster resonance energy transfer (FRET) process. Cushing et al has demonstrated the PRET process in Au@SiO_2@Cu_2O nanocomposite.[23] The Au LSPR features matches with the absorption features of Cu_2O. Although SiO_2 layer is in between the Au and Cu_2O, the RET process can still generate electron-hole pair in the Cu_2O as shown in Figure 1.8. The SiO_2 (an insulator) interlayer effectively blocks the DET process, while still allowing the RET process.

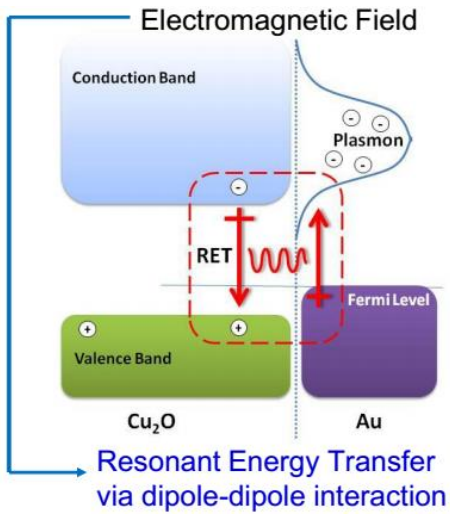

Figure 1.8: Resonance energy transfer from Au LSPR dipole to Cu_2O via dipole-dipole interaction.

1.3. Role of co-catalyst in solar water splitting

Overall water splitting can be achieved when the semiconductor is modified with suitable co-catalyst. Generally cocatalyst doesn't absorb any solar light and it provides the active sites for the half reactions. Therefore it is important to develop cocatalyst to improve the photocatalytic hydrogen and oxygen evolution from water. Noble metals, such as Pt and Rh, are well known cocatalysts for hydrogen evolution reaction. RuOx, NiO and CoOx are the well known cocatalyst for oxygen evolution reaction.[27] Cocatalyst decreases the activation energy for the hydrogen and oxygen evolution. A schematic diagram of the role of cocatalyst has been shown on Figure 1.9. Electrons (holes) in the conduction (valence) band is effectively transferred to the respective co-catalyst, which is the critical step before the reduction or oxidation occurs.

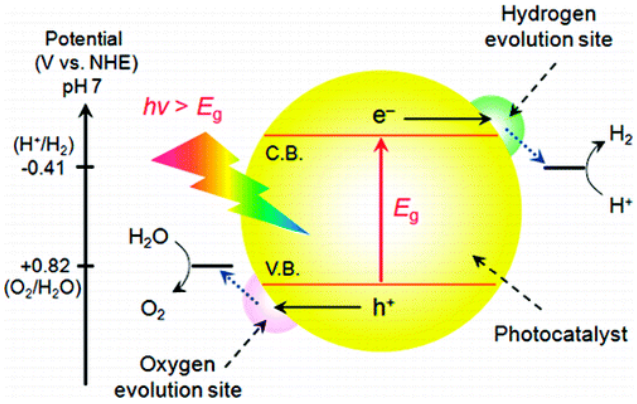

Figure 1.9: Schematic diagram of Overall water splitting in a semiconductor photocatalyst in presence of oxygen and hydrogen evolution cocatalyst. (Reproduce with permission from ACS).

Electrochemical methods are the best way to characterize the cocatalytic activity of any material.[28,29] In this thesis, we mostly concentrate on the electrocatalytic and photocatalytic HER. Herein, we demonstrate that electrocatalytic process is a strong tool to understand the complex reaction system involves in photocatalysis.

1.3.1. Fundamentals of electrocatalytic HER

The HER and OER occurs at the cathode and anode of an electrochemical cell. The other two important energy conversion processes are the hydrogen oxidation reaction (HOR) and

oxygen reduction reaction (ORR). The HER and HOR is in equilibrium with each other and OER is in equilibrium with ORR, as shown in the polarization graph in Figure 1.10. The equilibrium potential for HER and HOR is 0 V vs RHE, whereas the equilibrium potential for ORR and OER is 1.23 V vs RHE.

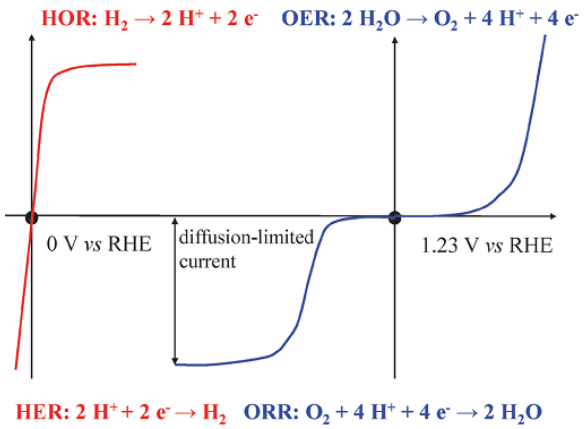

Figure 1.10: Polarization curves for two pairs of the key energy-related electrochemical reactions and their overall reaction equations. (Reproduce with permission from RSC).

HER and OER generally obey the Butler-Volmer model even with very high overpotentials, while the HOR and ORR approach a constant current at a certain overpotential due to the limitation in mass transfer.[30] The kinetics of this reaction is influenced by the overall performance of the catalyst. The most critical factor is how to effectively catalyze these reactions (HER and OER) to achieve higher current density but at low overpotential. The kinetic of the HER and HOR reaction is facile due to the two electron transfer process. However, the multistep proton-coupled and four electrons transfer process, makes the ORR and OER kinetically sluggish. For example, the main reason behind the decrease in efficiency of proton exchange membrane fuel cells (PEMFC) is the poor catalytic performance of the cathodic ORR electrode.[31] Therefore these reactions are generally catalyzed by precious metals such as Pt, Ru-based catalyst to achieve favorable reaction kinetics. However, due to their high costs and scarcity of these metals prevents them to move towards practical applications. In this regard, finding an alternative solution for electrocatalyst made of inexpensive and earth abundant material is highly necessary.

The HER involves three possible reaction steps as shown below

1 Volmer step $H^+ + e^- \rightarrow H_{ad}$

2 Heyrovsky $H^+ + H_{ad} \rightarrow H_2$

3 Tafel step $2H_{ad} \rightarrow H_2$

The HER may occurs through a Volmer-Heyrovsky mechanism or Volmer-Tafel mechanism. In both the process, the first step is the hydrogen adsorption and hence the overall rate of reaction is influenced by the free energy of hydrogen adsorption (ΔG_H). If the hydrogen binds weakly to the surface of catalyst, the adsorption step will limit the overall reaction rate. If the hydrogen bind too strongly to the catalyst surface, then desorption step will be hindered, which will limit the overall reaction rate. Hence the optimum condition for a good HER catalyst is that, it should have ΔG_H close to zero, i.e. binding energy of hydrogen to the catalyst surface, neither to weak nor too strong. Based on the DFT calculation and experimental results, this principle gives rise to the volcano relationship as shown in Figure 1.11.[30b] The Volcano plot is a relation between exchange current density (a measure of catalytic activity) versus ΔG_H. The catalyst, which is having high exchange current density and ΔG_H close to zero, is the most active catalyst for HER. In this regard, Pt is the most active catalyst for HER as shown in Figure 1.11. In this work, keeping in mind on volcano plot, an attempt has been made to synthesize a Ni-Cu alloy and MoS_2-mGO (mildly oxidized graphite) catalyst. These catalysts were studied for both photocatalytic and electrocatalytic HER.

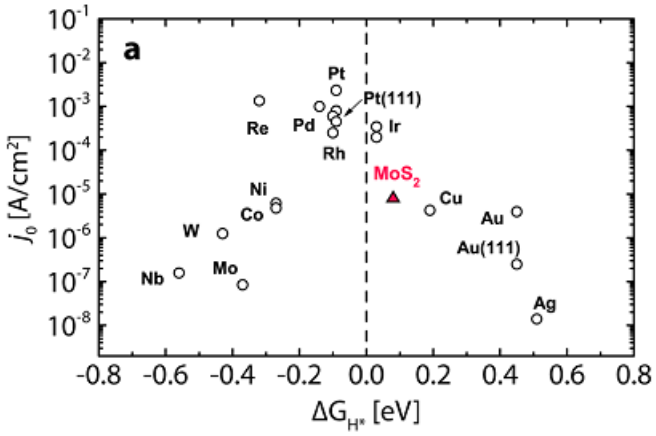

Figure 1.11: Volcano plot for various HER catalysts. Pt shows the highest exchange current density with slightly negative free energy of hydrogen adsorption, has the highest HER activity. (Reproduce with permission from ACS).

1.3.2. Parameters for catalyst activity comparison.

The first step in characterizing HER catalyst is the activity measurement. These measurements are generally performed by supporting the catalyst on a conducting substrate and performing cyclic voltammetry (CV) or linear sweep voltammetry (LSV) measurements. In these measurements, the catalytic current is plotted against the applied voltage. For water splitting reaction, the voltage usually refers with respect to reversible hydrogen electrode (RHE). Onset potential is the most important characteristic feature of the catalyst where the catalytic current starts as shown in Figure 1.12. Catalyst with lower onset potential value is highly active for HER.[30b] However, it is highly desirable to carry out the reaction without applying any external potential.

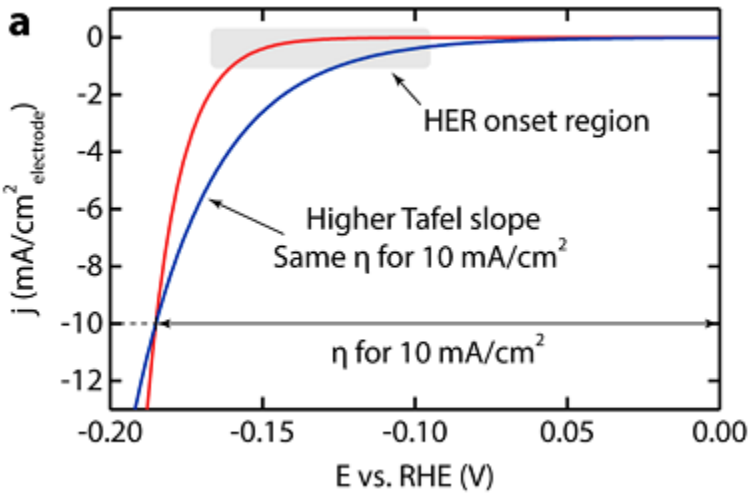

Figure 1.12: Schematic presentation of linear sweep voltammograms and the HER onset region. (Reproduce with permission from ACS).

The onset potential should always be described with respect to a certain current density. A more relevant way to represent the catalytic activity is the potential required to achieve a 10 mA cm^{-2} current density. In solar water splitting, generally the 10 mA cm^{-2} current density refers to an efficiency of 12.3 % in a solar to hydrogen conversion devices. Another way to represent

the catalytic activity is through Tafel slope and exchange current density. Tafel plots provide the information on how much increase in the overpotential is required to increase the reaction rate by a factor of 10. A simple representation of the Tafel plot is given in Figure 1.12. The exchange current is the current at equilibrium, i.e. the rate at which oxidized and reduced species transfer electrons with the electrode. In other words, the exchange current density is the rate of reaction at the reversible potential (when the overpotential is zero by definition). At the reversible potential, the reaction is in equilibrium directly hinting the forward and reverse reactions progress at the same rates. This rate is the exchange current density. By transferring the knowledge of electrocatalytic HER in to photocatalysis, we have made an attempt to design a new cocatalyst made from earth abundant material for solar hydrogen generation.

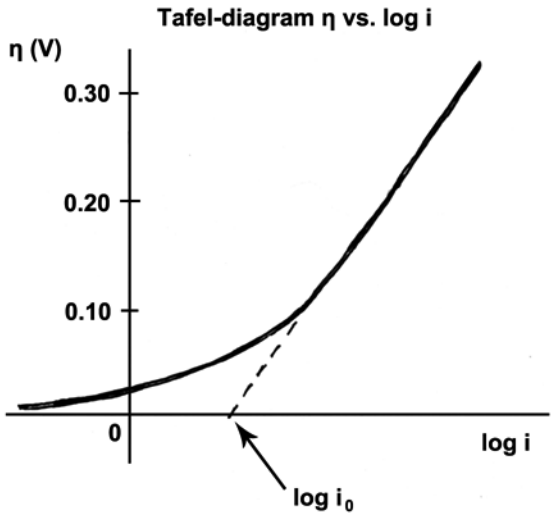

Figure 1.12: A schematic representation of the Tafel plot and exchange current density. (Adopte from Wikipedia).

1.4. Thin film approach for solar water splitting.

The use of powder catalyst is the simplest way to generate hydrogen from solar water splitting. However, powder catalyst has many disadvantages like, grain boundaries, large amount of surface defects, poor charge separation and migration to the active sites.[7] The efficiency of powder catalyst is very less with low irradiation condition, while thin film retains the activity. A

critical aspect to be considered is the charge diffusion and the utilization of those charges for redox reactions at the respective sites. On the contrary, the powder nature of photocatalyst materials helps for charge recombination or trapping due to the large number of defects on the surface of semiconductors. Especially, when the surface area is high, number of defects also high and it helps towards decreasing extent of charge utilisation. Although there are some success with powder form of photocatalysts,[32] in general, the powder nature of photocatalysts is likely to be the biggest hurdle for utilizing the charge carriers. A possible strategy to improve the charge diffusion and charge utilization is to connect the redox reaction sites to charge generation (or light absorption) sites in a seamless manner.

Above issues can be partially solved by thin film approach. The key advantages of thin film approach are (a) small amount of catalyst required, (b) better performance even under low irradiation condition, (c) large area exposure is practicable, and (d) can be custom designed for production. There are very limited solar energy utilization technologies are available for water splitting (Fig. 1.13a). Artificial photosynthesis through thin film approach is the fourth solar utilization technique after photovoltaic, solar heat and biomass. As shown in Figure 1.13, water electrolysis process using solar photovoltaic setup shows the highest efficiency for water splitting reaction. However, it is not cost effective and involves complex fabrication method. Although, powder based photocatalyst system is cost effective and involves simple fabrication methods, low efficiency limits its practical applications. Hence, there is a necessity to find out a suitable solution to achieve good efficiency with less complex and cost effective system. In this regard, artificial photosynthesis is the best technique to solve the above mentioned issues. It is also to be underscored that the reported efficiency with overall water splitting, till to date, is very low because of the kinetically sluggish OER. Nocera et al has demonstrated an artificial photosynthetic device; consist of Si solar cell with 2.5% efficiency (in wireless condition).[33a] In this device, a Co catalyst and NiMoZn catalyst was used for OER and HER respectively (Fig. 1.13 b). The Co catalyst was photodeposited on one side of the Si solar cell and the NiMoZn catalyst was electodeposited on the other side of solar cell. On light illumination, O_2 generated from Co catalyst surface and H_2 generated from NiMoZn catalyst surface. The device exhibited 4.7 % efficiency in wired configuration , where NiMoZn catalyst was deposited on a Ni mesh and acts as the counter electrode. The device is highly stable in both wired and wireless

configuration. In this particular device, the potential required for overall water splitting is generated from a parallel Si solar cell. Hence it is highly desirable to make photosynthetic devices at low cost, which also should exhibit high efficiency at zero applied potential (or wireless configuration).

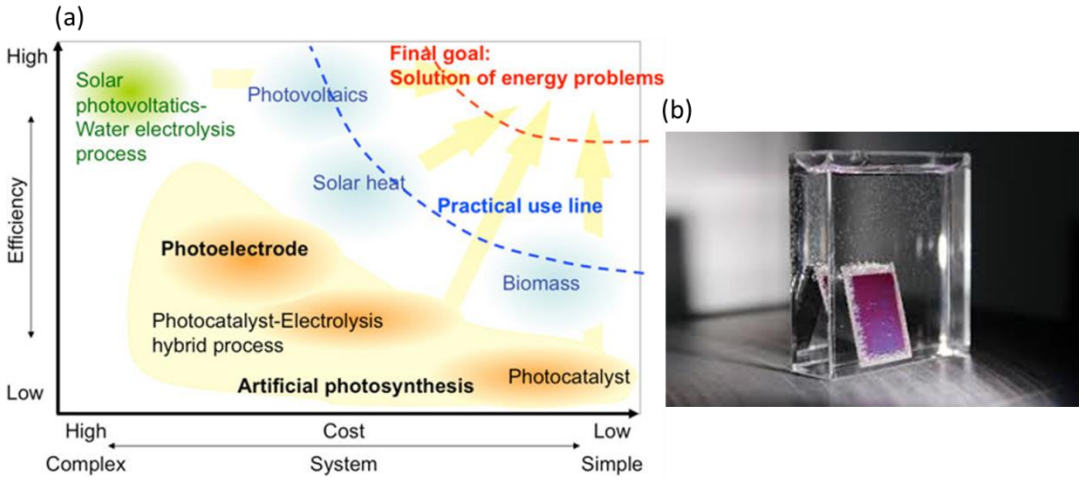

Figure 1.13: (a) Comparison of various solar energy technology (Adopted from www.nanowerk.com), and (b) artificial leaf made of Si solar cell and earth abundant catalyst producing H_2 and O_2 from water splitting.

1.5. Quasi-artificial leaf approach for solar hydrogen generation.

In natural photosynthesis, the leaf converts the solar energy in to chemical energy by water splitting (basically electrolysis of water to hydrogen and oxygen with sunlight and hydrogen gets consumed for CO_2 reduction to carbohydrates) through photosynthesis process. The primary step for water splitting in natural system involves the absorption of light by photosystem-II (PSII) and subsequent separation of electron hole pair. The active unit in PSII in natural photosynthesis is a somewhat ill-defined Mn_4O_5Ca cluster with a $[Mn_4O_4]$ cubic unit as the core housed in a protein environment. The holes in the PSII oxidize water to oxygen with the release of four electrons and four protons. Hydrogen formed in the form of NADPH in photosystem-I, where ferridoxin provides the active sites for reduction reaction. A schematic diagram of water splitting reaction takes place in natural system is shown in Figure 1.13.[33]

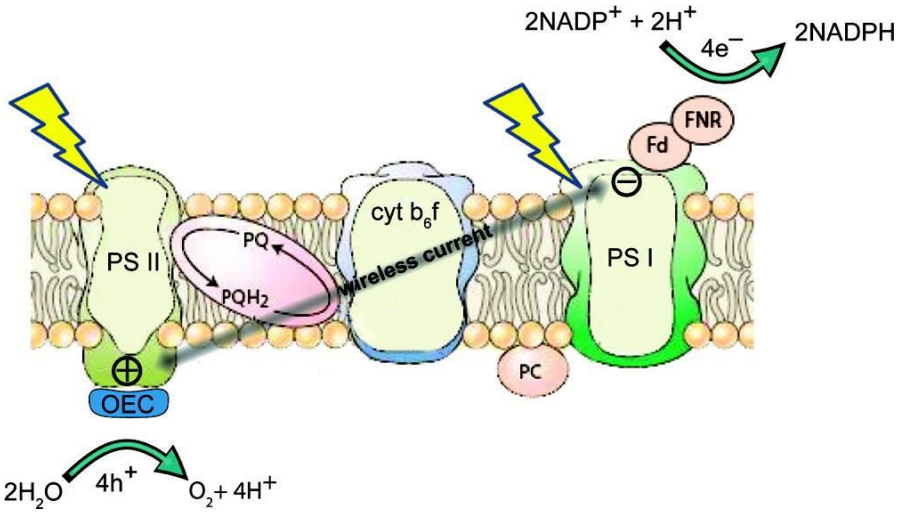

Figure 1.14: A simple schematic presentation of the sun light driven photosynthesis process. (Reproduce with permission from ACS).

Current generated flows from the photosystem-II to photosystem-I in a wireless architecture during the overall process. This concept is known and practiced by few well-known researchers like, Nocera.[33a,b] Inspired by the natural photosynthesis process, in this current study, we have designed a photochemical device which is similar to leaf and consists of $AuTiO_2$/PbS/CdS as light absorption unit and Pt as cocatalyst for H_2 evolution over FTO plate. Unlike natural system, photocurrent generated in the artificial system flows from the light absorption unit to cocatalyst unit, through the FTO plate. This is the reason why such system being named as artificial leaf. However, instead of generating oxygen (as in photosynthesis), holes are injected into the solution to oxidize sulfide+sulfite to thiosulfate as side product. Hence we get wet hydrogen as the only product. The word quasi in quasi artificial leaf (QuAL) is for selectively using one of the charge carriers (electrons) for hydrogen generation in the whole process.

Semiconductors quantum dots (QDs) sensitization is another way to improve the light absorption capacity of wide band gap semiconductor like TiO_2.[34] QDs possess high visible light absorption coefficient and can be used in QuAL device for improved hydrogen generation. The interaction of photons with bulk semiconductor QDs are very less, whereas small size QDs interact strongly with photons due to quantum size effect.[8] The key advantage of quantum size

effect is the tuneablity of optical band by varying the size of QDs which open up new ways to harvest photons in the entire solar spectrum. The band gap increases significantly with decrease in size of QDs and as a result the colour associated with QDs change gradually on

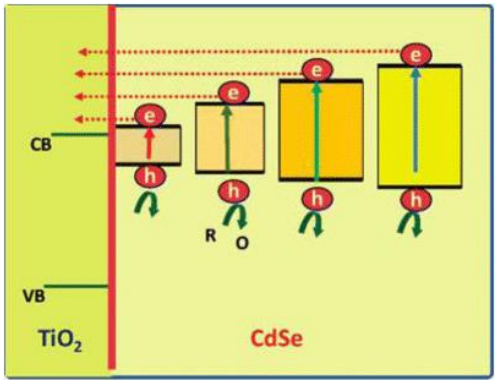

Figure 1.15: Size quantization effect on CdSe QDs and the electron transfer from conduction band of QDs to TiO_2 conduction band (Reproduced with permission from ACS).

decreasing the size as shown in Figure 1.15. In addition to the tunable optical absorption, the electron transfer to semiconductor is also feasible in small size QDs. As the size of the QDs decreases, the conduction band shifted to more negative potential which facilitated the electron transfer in the composite system.[35] It is to be noted that high negative potential associated with CB (compared hydrogen reduction potential) enhances the hydrogen generation. Charge separation is another advantage exhibited by QDs. The above discussed advantage of QDs makes them a potential candidate for solar water splitting. In the quantum dot sensitized semiconductor, the charge transfer take place at the hetero junction formed at the interface of QDs and semiconductor. Figure 1.16 shows the schematic representation of the charge transfer process, where QDs absorb the light and transfer electron to semiconductor through heterojunction.[8] The sensitization by QDs is very similar to dye sensitization process (DSSC). Good photon conversion efficiency has been observed with QDs even at lower wave length. By using this concept, a wireless photochemical cell or quasi artificial leaf (QuAL) was prepared to generate hydrogen without applying any potential. Success of this approach possibly would help to design better light harvesting synthetic architectures to produce solar fuels.

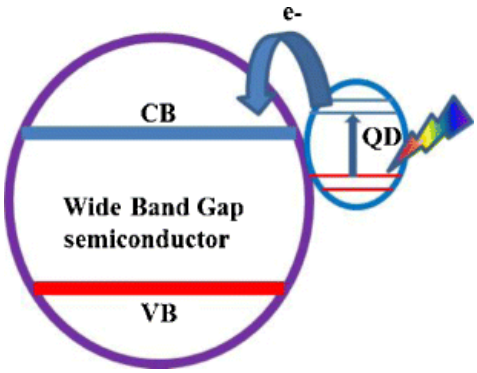

Figure 1.16: A simplified scheme of quantum dots sensitized wide band gap semiconductor.

1.6. Objective of the thesis

The main objective of the current thesis is to address the issues related to the maximum solar light absorption (including NIR and UV), designing relevant co-catalyst with an emphasis to replace the currently practiced Pt and made of earth abundant material for HER. Taking in to the consideration of the above mentioned issues, a systematic approach was adopted to improve the light absorption capacity of the catalyst by using plasmonic nanostructures. The utilization of the red-green-blue (RGB) and near IR photons for solar hydrogen evolution has been discussed in a single plasmonic nanocomposite of $AgTiO_2$-AuNR. It is also realized that the longitudinal plasmon resonance of AuNR in AgT-AuNR induces solar hydrogen evolution between 550 and 800 nm, whereas TiO_2-AuNR or $AgTiO_2$ shows no activity in this wavelength range. An emphasis was made on the electrocatalytic activity evaluation of NiCu and MoS_2-mGO new co-catalysts and incorporating the same for the evaluation of HER activity in the photochemical devices. Extensive characterization has been carried out to understand the correlation between activity and the nature of surface of HER catalysts. An unique hydrothermal assisted intercalation method was introduced to fabricate exfoliated MoS_2-mGO composite, which also acts as cocatalyst for H_2 production. Finally, new co-catalysts were successfully integrated with the light absorbing photoanode to make a QuAL. Detailed spectroscopic technique like XPS, UVPES, combined with electrocatalytic studies were made and correlated the results with photocatalysis, which gives an indication for new pathways towards designing better solar light harvesting architectures.

1.7. Outline of the thesis

Chapter 1 presents a brief introduction to photocatalytic water splitting reaction. Also this chapter describes the importance of plasmonic nanostructure/semiconductor composite for solar light harvesting. The role of cocatalyst and how it is essential to design cocatalyst made from earth abundant material for solar water splitting has been described here. A brief introduction in to the electrochemical method to characterize the catalytic activity of cocatalst has been described. Moreover the quasi artificial leaf approach for solar hydrogen production is also discussed here.

Chapter 2 deals with the synthesis of gold-silver-titania (AgAuT) composite by photodeposistion method. This chapter also describes the synthesis of different aspect of gold nanorods (AuNR) and Ag-TiO_2-AuNR (AgT-AuNR) composite. The synthesis of NiCu and MoS_2-mGO is discussed in this chapter. SILAR (successive ionic layer adsorption and reaction) is an important method to prepare chalcogenide semiconductors in the form of QDs. Relevant characterization methods such as, Raman spectroscopy, UV-visible spectroscopy and transmission electron microscopy (TEM) aspects are briefly described in this chapter.

Chapter 3a deals with the detailed characterization of AgAuT composites and its application towards photocatalytic hydrogen evolution. Enhanced photocatalytic activity of AgAuT is partly attributed to the formation of hot electrons. A thin layer of Ag coating on Au particles leads to a core–shell morphology with Au in the core. Fermi level equilibration between metal and titania, and Schottky junction formation are directly demonstrated.

Chapter 3b deals with the detailed characterization of AgT-AuNR composite. Near IR-light driven photocatalytic hydrogen evolution is achieved with this catalyst and discuss in this chapter. It is demonstrated that the longitudinal plasmon resonance of AuNR in AgT-AuNR induces solar hydrogen evolution between 550 and 800 nm, whereas TiO_2-AuNR or AgT shows no activity in this wavelength range. The key aspect of achieving the high photocatalytic activity of AgT-AuNR in the solar spectrum is the electronic integration among metal NPs as well as with TiO_2, and the heterojunctions among them. Gold nanorods also exhibits field effect and further enhances light harvesting. Although the absolute amount of energy harvested only from

near IR photons is low, when combined with high energy visible light photons within one sun conditions, it shows a multiplier effect rather than a simple additive effect.

Chapter 3c describes the role of LSPR in DSSC. In this chapter the performance of $AuTiO_2$ based DSSC device is discussed.

Chapter 4a describes the quasi artificial leaf approach with $AuTiO_2$/PbS/CdS photochemical cell with Pt as cocatalyst for solar hydrogen production. It focusses on using the AuNPs as a plasmonic sensitizer along with PbS/CdS QDs for designing wireless photochemical cell at no applied potential. It is also demonstrated that quasi-artificial leaf in wireless configuration harvests the solar light and converts it to H_2 very efficiently than the wired configuration. A direct coupling of all components among themselves enhances the light absorption in the entire visible and NIR region and charge utilization. Thin film approach, as in DSSC, combined with porous titania enables networking of all the components of the device, and efficiently converts solar to chemical energy in a sustainable manner.

Chapter 4b deals with the quasi artificial leaf approach with TiO_2/PbS/CdS photochemical cell with NiCu as cocatalyst for sustainable solar hydrogen production.

Chapter 4c describes the solar hydrogen production in TiO_2/PbS/CdS photochemical cell with MoS_2-mGO (mildly oxidized graphene) as co-catalyst. In this chapter we discuss the dual role of MoS_2-mGO composite (i.e. the cocatalytic and photocatalytic activity in the QuAL device).

Chapter 5 summarizes the conclusions derived based on the observation and results obtained from the entire study. Possible future outlook of the present research work, such as extending the present approach to overall water splitting, is described at the end.

References

1. A. Fujishima, T. N. Rao and D. A. Tryk, *J. Photochem. Photobiol*, C, **2000**, 1, 1.
2. A. Fujishima, X. Zhang and D. A. Tryk, *Int. J. Hydrogen Energy*, **2007**,32,2664.
3. K. Hashimoto, H. Irie, A. Fujishima, *Jap. J. Appl. Phys.*, **2005**, 44, 8269.

4. S. Bagheri, Z. A. M. Hir, A. T. Yousefi, S. B. A. Hamid, *Microporous and Mesoporous Mater*., **2015**, 218, 206-222.
5. A. Kudo and Y. Miseki, *Chem. Soc. Rev.*, **2009**, 38, 253–278.
6. A. Fujishima and K. Honda, *Nature*, **1972**, 238, 37.
7. S. Linic, P. Christopher and D. B. Ingram. *Nature Mater.,* **2011**, 10, 911-921.
8. S. RajaAmbal, K. Sivaranjani and C. S. Gpinath, *J. Chem. Sci.*, **2015**, 127, 33-47.
9. (a) J. R. Maiolo, B. M. Kayes, M. A. Filler, M. C. Putnam, M. D. Kelzenberg, H. A. Atwater, and N. S. Lewis, *J. Am. Chem. Soc.*, **2007**, 129, 12346-12347.(b) J. Goldberger, *Nature*, **2003**, 422**,** 599–602.
10. V. Subramanian, E. E. Wolf and P. V. Kamat, *J. Phys. Chem. B*, **2001,**105, 11439–11446. (b) V. Subramanian, E. E. Wolf and P. V. Kamat, *J. Am. Chem. Soc*, **2004**, 126**,** 4943–4950.
11. (a) K. K. Patra, C. S. Gopinath, *ChemCatChem* **2016**, *8*, 3294–3301. (b) K. K. Patra, B. D. Bhuskute, C. S. Gopinath, *Sci. Rep.* **2017**, *7*, 6515. (c) K. Sivaranjani, S. RajaAmbal, T. Das, K. Roy, S. Bhattacharyya, C. S. Gopinath, *ChemCatChem*, **2014**, *6*, 522-530.
12. (a) P. Hernley, S. Chavez, J. Quinn and S. Linic, *ACS Photonics*, **2017**, 4, 979–98. (b) C. Boerigter, U. Aslam and S. Linic, *ACS Nano*, **2016**, *10*, 6108–6115.
13. S. Linic, U. Aslam, C. Boerigter and M. Morabito, *Nat. Mater*., **2015**, *14*, 567-676. (b) U. Aslam, S. Chavez and S. Linic, Nature Nanotech. 2017, doi:10.1038/nnano.2017.131
14. M. Faraday , *Philos. Trans. R. Soc. London* **1857**, 147, 145-181 .
15. S. A. Maier , *Plasmonics: Fundamentals and Applications*, Springer , Berlin, Germany, 2007.
16. (a) A. Kabashin , P. Evans , S. Pastkovsky , W. Hendren , G. Wurtz ,R. Atkinson , R. Pollard , V. Podolskiy , A. Zayats , *Nat. Mater.,* **2009**, 8, 867-871. (b) J. P. Camden , J. A. Dieringer , J. Zhao , R. P. Van Duyne , *Acc. Chem. Res.* **2008**, 41, 1653-1661.
17. P. L. Stiles, J. A. Dieringer, N. C. Shah, and R. P. Van Duyne Annu. *Rev. Anal. Chem.,* **2008**. 1, 601–26.
18. (a) M. Rycenga , C. M. Cobley , J. Zeng , W. Li , C. H. Moran , Q. Zhang, D. Qin , Y. Xia, *Chem. Rev,* **2011**, 111, 3669-3712. (b) Z. Li , F. Hao ,Y. Huang , Y. Fang , P. Nordlander , H. Xu , *Nano Lett.*, 2009, *9*, 4383-8386. (c) W. L. Barnes, A. Dereux, T. W. Ebbesen, *Nature.*, **2003**, 424, 824-830 .
19. A. W. Wark, H. J. Lee, R. M. Corn, *Anal. Chem.*, **2005**, 77, 3904-3907.

20. U. Kreibig, M. Vollmer, *Optical Properties of Metal Clusters*, Springer, Berlin, Germany, 1995. b) S. Lal, S. Link, N. J. Halas, *Nat. Photonics*, 2007, 1, 641-648.
21. (a) K. L. Kelly, E. Coronado, L. L. Zhao and G. C. Schatz, *J. Phys. Chem. B,* **2003**, 107**,** 668–677. (b) P. K. Jain, K. S. Lee, I. H. El-Sayed, M. A. El-Sayed, *J. Phys. Chem. B*, **2006**, 110, 7238-7248.
22. Z. Liu, W. Pavaskar, M. Aykol and S. B. Cronin, *Nano Lett.* **2011**, 11, 1111-1116.
23. S. K. Cushing, J. Li, F. Meng, T. R. Senty, S. Suri, M. Zhi, M. Li, A. D. Bristow, and N. Wu, *J. Am. Chem. Soc.*, **2012**, 134, 15033-15041.
24. P. K. Jain, K. S. Lee, I. H. El-Sayed and M. A. El-Sayed, *J. Phys. Chem. B*, **2006**, 110, 7238–7248.
25. A. Primo, A. Corma and H. Garcia, *Phys. Chem. Chem. Phys.* **2011**,13**,** 886–910.
26. P. Christopher, D. B. Ingram and S. Linic, *J. Phys. Chem. C*, 2010, 19, 9173-9177.
27. K. Maeda and K. Domen, *J. Phys. Chem. Lett*. **2010**, 1, 2655–266.
28. W. Bi, L. Zhang, Z. Sun, X. Li, T. Jin, X. Wu, Q. Zhang, Y. Luo, C. Wu and Y. Xie, *ACS Catal*. **2016**, 6, 4253−4257.
29. E. Nurlaela, T. Shinagawa, M. Qureshi, D. S. Dhawale, and K. Takanabe, *ACS Catal*. **2016**, 6, 1713−1722.
30. Y. Jiao, Y. Zheng, M. Jaroniecb and S. Jiao, Y. Zheng, M. Jaroniecb and S. Z. Qiao *Chem. Soc. Rev.*, **2015**, 44, 2060-2086. (b) J. D. Benck, T. R. Hellstern, J. Kibsgaard, P. Chakthranont, and T. F. Jaramillo, *ACS Catal.*, **2014**, 4, 3957−3971.
31. (a) M. K. Debe, *Nature*., **2012**, 486, 43-51. (b) B. C. H. Steele and A. Heinzel, *Nature.*, **2001**, 414, 345–352.
32. Z., Huafei Zheng, J. Li and P. Du, *Ene. Environ. Sci*., **2015**, 8, 2668-2676.
33. (a) S. Y. Reece, J. A. Hamel, K. Sung, T. D. Jarvi, A. J. Esswein, J. J. H. Pijpers, and D. G. Nocera *Science.*, **2011**, 334, 645-648. (b) D. G. Nocera, *Acc. Chem. Res..*, **2012**, 45, 767–776. (c) U. Maitra, S. R. Lingampalli and C. N. R. Rao, *Curr. Sci*., 2014, 106, 518-527.
34. P. Sheng, W. Li, J. Cai, X. Wang, X. Tong, Q. Cai and C. A. Grimes, *J. Mater. Chem. A.*, 2013, **1**, 7806-7815.
35. A. Kongkanand, K. Tvrdy, K. Takechi, M. Kuno and P. V. Kamat, *J. Am. Chem. Soc.*, **2008**, 130, 4007-4015.

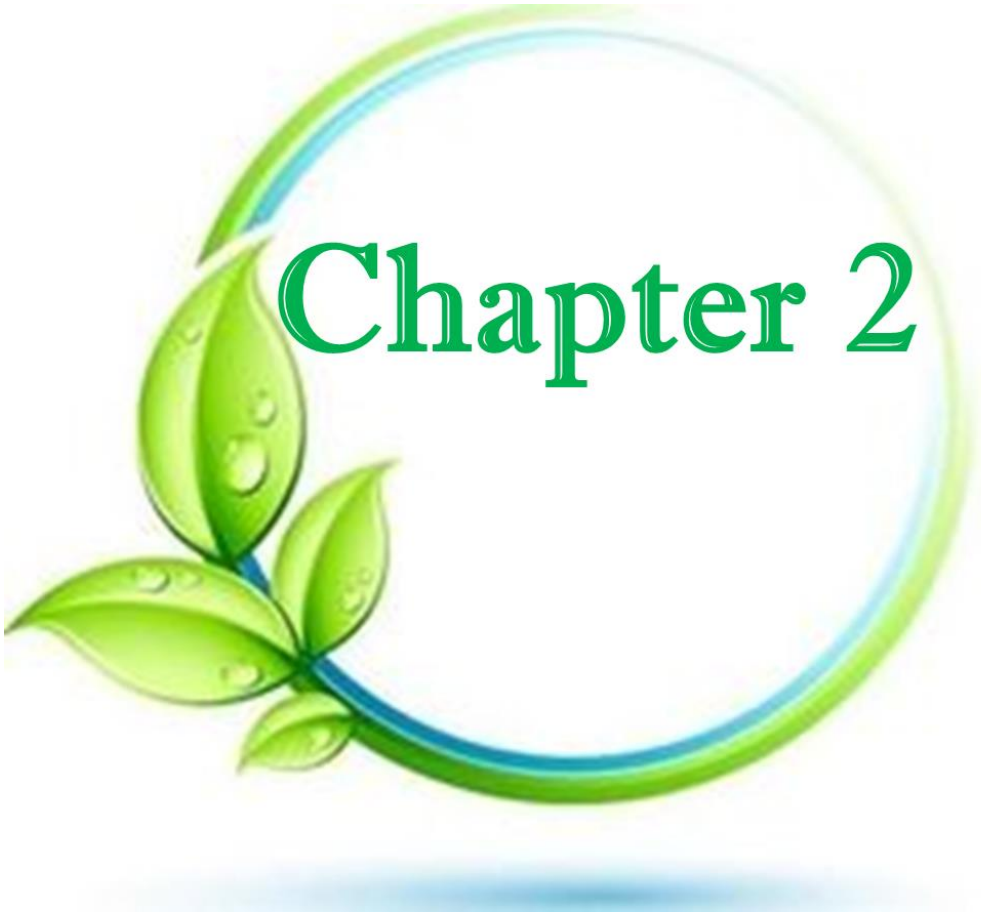

Experimental Methods

2. 1 Introduction

The unique properties of any material are mainly based on the synthetic procedures followed for the preparation of such materials. It is well-known that each step of the preparation procedure affects the catalytic properties of heterogeneous catalysts. Usually complex heterogeneous catalyst requires complex synthesis procedures. In the present thesis, many different methods were employed to prepare tio_2 based composite photocatalyst systems. Interestingly, porous nature of TiO_2 based material was retained even after composite formation with other metal/material deposition. Metal deposition on tio_2 was carried out by different procedures, such as photodeposition. Particularly, device fabrication was carried out in an efficient way to achieve better activity or photon to current conversion. Necessarily, variety of experimental methods was employed to understand the mechanism behind the successful material or composite formation attempts. Especially these methods helps to understand the working mechanism of the material or device and unique methods employed are briefly described. Introduction and theory of various physical, structural, textural, microscopy, and spectroscopic characterization techniques has been employed are also described in the present chapter.

2.2 Synthesis of catalyst

The synthesis of various compositions of AgT, AuT, AuNR, AgAuT, AgT-AuNR catalyst for solar water splitting (SWS) is discussed in this chapter. In the present case, the AgAuT composite was prepared by multi step photodeposition method. Interestingly, different aspect ratio of AuNR was synthesized and incorporated in to AgT. The complete device fabrications for quasi artificial leaf (QuAL) and synthesis of earth abundance catalyst like NiCu and MoS_2-mGO are describe in the present chapter.

2.2.1. Preparation of the AgAuT composite.

Au-TiO_2 (AuT) was prepared by photodeposition method. Different Au weight percent deposited catalysts were prepared by using required amount of $HAuCl_4$ as Au precursor.[1] For example, 0.25 wt % Au was deposited over TiO_2 (Degussa P25) by taking 500 mg of $HAuCl_4$ as Au precursor with 100 mL methanol in a 500 mL quartz RB and irradiated with 400 W UV lamp for 1 h.[2] After irradiation, the solution was centrifuged, washed with distilled water and dried at room temperature. Very similarly, AgT was also prepared with $AgNO_3$ as silver precursor.

For AgAuT, 500 mg of $AuTiO_2$ (containing 0.25 wt % Au) was taken with $AgNO_3$ as silver precursor and the same procedure was followed. Different AgAuT compositions was prepared by varying the Ag deposition time and denoted as 20AgAuT, 40AgAuT, 60AgAuT and 80AgAuT for 20, 40, 60, and 80 min Ag deposition time respectively. In terms of weight percent, 20, 40, 60 and 80 corresponds to 0.07, 0.14, 0.2, and 0.27 wt % of Ag, respectively.

2.2.2. Preparation of AgT-AuNR composite.

Synthesis of gold nanorods: AuNRs were prepared by seed mediated method, and based on the procedure reported by El-Sayed et al.[3] Seed solution was first prepared by adding aqueous CTAB (5 ml, 0.2 M) to 5 ml of 0.0005 M $HAuCl_4$ solution. 0.6 ml of ice-cold $NaBH_4$ solution (0.01 M) was added drop wise to the above solution under vigorous stirring condition, which results in the formation of brownish yellow colour. This indicates the formation of gold seed. Stirring was continued for 2 min to allow the hydrolysis of any unreacted $NaBH_4$. Nanorod growth solution was prepared by adding CTAB (5 mL, 0.02 M) to 50, 70, 90, 120 mL of 0.004 M $AgNO_3$ solution, followed by the addition of 5 ml of 0.0005 M $HAuCl_4$ solution. The above solution was stirred for 2 min. and then 10 µL of seed solution was added and the whole solution was kept undisturbed for 30 min. By changing the amount of $AgNO_3$ solution, four different aspect ratio of gold nanorod were prepared and used for catalyst preparation. Synthesis of AgT-AuNRs: First Ag-TiO_2 (AgT) was prepared by photodeposition method. 0.85 wt % Ag was deposited over TiO_2 by taking $AgNO_3$ as Ag precursor with 100 mL methanol in a 500 mL quartz RB and irradiated with 400 W UV lamp for 1 h. In the same manner, different Ag weight percent deposited catalysts were also prepared. After irradiation, the solution was centrifuged, washed with distilled water and dried at room temperature. 0.85 wt % of silver loaded titania exhibit the highest activity for solar hydrogen evolution and hence it was used for remaining AgT-AuNRs preparation.

The AuNRs colloidal solution was centrifuged, washed with water and then sonicated with $HClO_4$ solution to remove the surfactant from the surface of the gold nano rods.[4]The AuNRs with different aspect ratio was introduced on to $AgTiO_2$ by wetness impregnation method and the slurry was dried at 40 ^{0}C overnight. These catalyst are denoted as AgT-AuNR645, AgT-AuNR690, AgT-AuNR710, AgT-AuNR770; Numbers given in the material

code (645-770) corresponds to longitudinal absorption maximum wavelength at 645, 690, 710, 770 nm in the UV-visible absorption spectrum, respectively.[5]

2.2.3. Synthesis of $AuTiO_2$ by deposition precipitation method

The different composition of $AuTiO_2$ was prepared by deposition precipitation method using urea as a basification agent.[6] Briefly, 500 mg of TiO_2 (particle size 20 nm) was taken in 250 ml beaker followed by addition of 200 ml distilled water. Then 0.6 gm of urea was added to suspension under continuous stirring. Finally different weight percent of $HAuCl_4$ was added and increased the temperature up to 80°C .[7]The suspension was kept under stirring condition at 80°C for 12 h. Then the solution was centrifuged, washed with ethanol and dried at 60°C. After drying the material was calcined in muffle furnace at 450°C for 2 h at a ramping rate of 5°C min^{-1}. Then the calcined material was ground and used for further characterization.

2.2.4. Synthesis of $AuTiO_2$ by physical mixture method

First 2 nm AuNPs was synthesized by $NaBH_4$ reduction method using CTAB as surfactant. Briefly 0.364 g of CTAB was dissolved in 5 ml of millipore water in 50 ml beaker. Then 5 ml of 0.001 M $HAuCl_4$ solution was added drop wise to it. Then freshly prepared ice cold solution of $NaBH_4$ (60 µl, 0.01 M) was added to it. The solution color turned to light brown. The particle size of AuNPs was confirmed from TEM analysis .The $AuTiO_2$ (PM) was prepared by mixing directly the AuNPs to the TiO_2.

2.2.5. Synthesis of NiCu bimetallic nanoparticles.

The following procedure describes the synthesis of NiCu nanoparticles.. Required amount of nickel (II) nitrate hexahydrate, $Ni(NO_3)_2.6H_2O$ and copper (II) acetate monohydrate, $Cu(ac)_2.H_2O$ was added to 25 mL of oleylamine. The reaction mixture was magnetically stirred for an hour at 120 ℃ . The colour of the solution changed from green to black, indicating the formation of nanoparticles. The black solution was cooled to room temperature and then the nanoparticles formed were fully retrieved by centrifugation. Four different type of composition Ni_1, $Ni_5Cu_{1.25}$, $Ni_5Cu_{2.5,}$ $Ni_5Cu_{3.75}$, and Ni_5Cu_5 were prepared by varying the Cu:Ni ratio. For example, the $Ni_5Cu_{2.5}$ bimetallic NPs were synthesized by adding 5 mmol of $Ni(NO_3)_2.6H_2O$ and 2.5 mmol of $Cu(ac)_2.H_2O$ to oleylamine and heated to 120 °C. The reaction mixture was kept

under stirring for 30 min at 120 °C and then the temperature was increased fast to 180°C and then the reaction mixture was kept under stirring for 1 h. Then the as synthesized NiCu NPs were fully recovered by centrifugation.

2.2.6. Synthesis of MoS_2-mGO composite.

Synthesis of mGO: Graphene oxide (GO) with low degree of oxidation (or mildly oxidized GO (mGO) was prepared by a modified Hummers method.[8] 3 g of graphite powder was taken in a 250 ml beaker. A total of 0.5 mg $NaNO_3$ was added followed by addition of 23 ml concentration H_2SO_4. The entire solution was stirred for 30 min in an ice bath. Next, 300 mg of $KMnO_4$ was added slowly to the solution. Then the ice bath was removed and stirred for 30 min. Next, 46 mL of distilled water was added to the entire solution and kept 100 °C for 15 min. Then 140 mL distilled water was added to the solution followed by the addition of 10 mL 30 % H_2O_2. The entire solution was washed with 5 % HCl and dried in vacuum at 60 °C.

Synthesis of MoS_2-mGO: mGO (100 mg) was dispersed in 60 mL water containing $(NH_4)_2MoS_4$ and sonicated for 1 h. Various compositions of MoS_2-mGO X:1 and (X= 1, 2, 3, 4) was prepared by keeping the GO amount constant and vary the $(NH_4)_2MoS_4$ concentration. Then the mixture solution was transferred in to a 100 ml autoclave and heated at 120°C for 14 h in an oven. The amount of $(NH_4)_2MoS_4$ precursor was 0.27 g, 0.54 g, 0.81 g and 1.08 g for MoS_2-mGO synthesis with 1:1, 2:1, 3:1 and 4:1 composition respectively.[9]

2.3. Fabrication of Devices

2.3.1. Fabrication of $AuTiO_2$ based DSSC

The paste for fabricating solar cell was prepared by employing 3 g of $AuTiO_2$ power and 65 ml ethanol was added followed by 30 min. stirring and 30 min. sonication. Then 10 gm terpinol was added and again stirred for 30 min. Finally 1.5 g of ethyl cellulose was added and stirred for 30 min. Ethanol was removed by a rotavapor at $60^{.0}$C. A doctor-blade technique was utilized to fabricate photoanode films. Briefly, transparent conducting glass (SnO_2:F, FTO glass, 15 Ω^{-1}) was cleaned by sonication in ethanol, acetone and DI water for 20 min. Then 8 μm for TiO_2 and 4 μm for $AuTiO_2$ thick electrodes were doctor-bladed onto FTO surfaces for different

devices. The pastes were then kept for ageing at $40^{.0}$C for 12 h before heating at $450^{.0}$C for 60 min to remove polymers. Then a 4 μm thick scattering layer was applied by doctor-blade method onto FTO surface followed by the same drying at room temperature for 12 h and heating at $450^{.0}$C for 60 min. After cooling down to room temperature, the electrodes were immersed in 0.5 mM N719 dye in acetonitrile/tert-butyl alcohol (1:1, v/v) at room temperature for 24 h., followed by rinsing with ethanol.[10]

A Pt counter electrode was prepared by thermal decomposition of 0.01 M H_2PtCl_6 in an isopropyl alcohol solution on the FTO substrate followed by sintering at $500^{.0}$C for 30 min. The iodine based liquid electrolyte was injected into the sandwich cells through the drilled holes in the Pt electrode. After that, it was sealed by Surlyn (25 μm, Solaronix) film. The effective areas of all the photoanodes are 0.16 cm^2.[9,11,12]

2.3.2. Fabrication of $AuTiO_2$/PbS/CdS photoanode for QuAL device.

Different composition of $AuTiO_2$ was prepared by deposition precipitation method using urea as a basification agent. 500 mg TiO_2 (particle size ~20 nm) was taken in to 250 ml beaker followed by the addition of 200 ml distilled water. Then 600 mg urea was added to the suspension under continuous stirring. Finally different weight of $HAuCl_4$ was added and kept at $80^{.0}$C for 12 h under stirring condition. Then the solution was centrifuged, washed with ethanol and dried at $60^{.0}$C. After drying the material was calcined in muffle furnace at $450^{.0}$C for 2 h at a ramping rate of $5^{.0}$C min^{-1}. Then the calcined material was ground and used for any characterization. The paste, for fabricating photochemical cell was prepared by taking 3 g $AuTiO_2$ powder and 65 ml ethanol was added followed by 30 min stirring and 30 min sonication. Then 10 g terpenol was added and again stirred for 30 min. Finally 1.5 g of ethyl cellulose was added and stirred for 30 min. Then the ethanol was removed by a rotary evaporator at $60^{.0}$C. Large quantity of materials allows to make several photoanodes in one attempt with same/similar quality; however, smaller quantity can also be used to make fewer thin films. A doctor-blade technique was utilized to produce photoanode films. FTO glass was cleaned by sonication in ethanol, acetone and de-ionized water for 20 min. Then 8 μm thick $AuTiO_2$ electrodes were prepared by doctor-blade method onto FTO surfaces. The pastes were then kept at $40^{.0}$C for 12 h before heating at $450^{.0}$C for 60 min to remove polymers.[13]

The $AuTiO_2$ thin film was sensitized with PbS QDs by SILAR technique. 0.02 M aqueous solution of $Pb(NO_3)_2$ was used as a Pb^{2+} source and a 0.02M $Na_2S.9H_2O$ in methanol/ water (50/50 v/v) was used as a sulfide source. A schematic representation of the SILAR technique has been shown in Figure 2.1. A single SILAR consists of immersion of the electrode in to the lead precursor for 20 s and then rinsed with distilled water followed by immersion in to sulfide precursor for 20 s. For CdS SILAR deposition, 0.05 M $Cd(NO_3)_2$ was used as Cd^{2+} source and 0.02 M $Na_2S.9H_2O$ in methanol/water (50/50 v/v) was used as a sulfide source. Two and twelve SILAR cycles were applied for PbS and CdS sensitization, respectively. After PbS/CdS sensitization, the electrode was coated with three SILAR cycles of ZnS. For this purpose, the $AuTiO_2$/PbS/CdS electrode was dipped in 0.1 M aqueous solution of $Zn(CH_3COO)_2$ for 1 min., then rinsed with distilled water followed by dipping the electrode in Na_2S solution for 1 min. ZnS is transparent to visible light and it protects the device from photocorrosion. Various control photoanodes (such as $AuTiO_2$/PbS, $AuTiO_2$/CdS, $AuTiO_2$, TiO_2/PbS, and TiO_2/CdS) were also prepared by following the above method and evaluated for SWS. It is also to be mentioned that cells prepared with different precursors for Pb^{2+}, Cd^{2+} and Zn^{2+} and different immersion time was evaluated for SWS, and the above procedure provides the optimum parameters.[14]

The $AuTiO_2$/PbS/CdS was fabricated for $1cm^2$ area over the conducting surface of the FTO.[3] Pt NPs was deposited by drop casting 5 mmol of chloroplatinic acid (H_2PtCl_6) (from Dyesol) over 0.4x1 cm^2 area of FTO and calcined at $450^{\cdot 0}C$ for 15 min. However, hydrogen evolution occurs exclusively from the Pt at the chalcogenide-Pt interface.

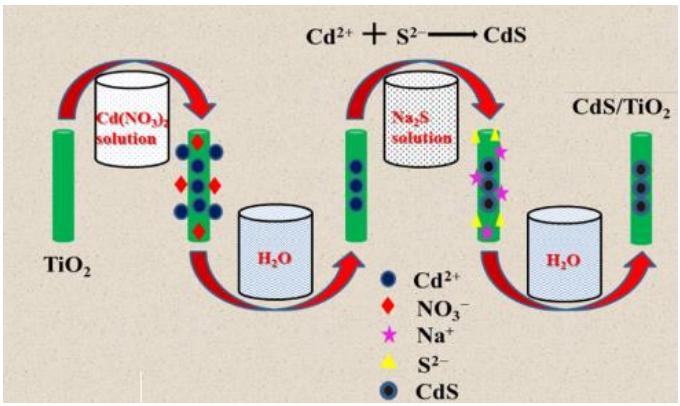

Figure 2.1: Single CdS SILAR deposition cycle.

2.3.3 Fabrication of the wireless photochemical cell for TiO_2/PbS/CdS with NiCu catalyst.

The TiO_2/PbS/CdS was fabricated for 1 cm^2 area over the conducting surface of the FTO. We prepared an ink of above NiCu NPs by adding 5 mg of catalyst to 1 ml of ethanol and sonicated for 30 min. 200 µL of ink was deposited near the photoanode on the FTO plate (0.4 cm^2). Pt NPs was deposited by drop casting 5 mmol of chloroplatinic acid (H_2PtCl_6) over 0.4x1 cm^2 area of FTO and calcined at $450^{\cdot 0}$C for 15 min.

2.4 Structural Characterization Methods

The structural property of the composite was characterized by relevant techniques such as high resolution transmission electron microscopy (HRTEM), UV-visible absorption and Raman spectroscopy. A FEI TECHNAI G2 S30 S-Twin electron microscope operating at 300 kV with a resolution of 0.17 nm was used for HRTEM analysis. The instrument is equipped with a field emission gun filament source. A FEI TECHNAI G2 20 S-Twin electron microscope equipped with Lab6 (Lanthanum hexa borate) filament was used for TEM analysis operating at 200 kV. The spectral resolution of this instrument is 0.214 nm. Horiba JY LabRAM HR 800 Raman spectrometer was used for Raman analysis. The spectra were recorded at room temperature in back scattering geometry using a 632.8 nm laser as excitation source. All the samples were placed over a glass plate in pellet form and the spectra was recorded. Photoluminescence (PL) measurement was conducted with a Horiba Jobin Yuon Fluorolog 3 spectrometer equipped with a 450 W xenon lamp. The instrument is equipped with double monochromator to provide the highest spectral resolution. Generally the double monochromator is recommended for power and thin film samples, where the scattered light can significantly interfere with signal. Diffuse reflectance UV-Vis measurement was performed using a Shimadzu spectrometer (model UV-2550) with spectral grade $BaSO_4$ as references material. Energy dispersive X-ray (EDX) measurements were performed on a SEM system (Leica, Model Stereoscan-440) equipped with EDX analyzer (Bruker, D451-10C Quantax 200 with X-fash detector) attachment. A small section of our QuAL device was coated with gold AuNPs with Emitech sputter coater (Supplied from sigma) with a applied voltage of 2 kV and a plasma current of 2 mA for 1 min before SEM analysis. However, for the gold containing sample, there was no gold coating was made. X-ray photoelectron spectra (XPS) of the samples were recorded with a custom built ambient pressure photoelectron spectrometer (APPES) (Prevac, Poland)

equipped with a VG Scienta's R3000HP analyzer and MX650 monochromator.[15] Monochromatic Al Ka X-rays were generated at 200 W and used for measuring the X-ray photoelectron spectrum (XPS) of the above mentioned samples. Base pressure in the analysis chamber was maintained in the range of 5 x 10^{-10} Torr. The energy resolution of the spectrometer was set at 0.7 eV at a pass energy of 50 eV. Binding energy (BE) was calibrated with respect to Au $4f_{7/2}$ core level at 84.0 eV. Samples were flooded with low energy electrons for efficient charge neutralisation.

2.5 Photoelectrochemical (PEC) measurements

All the photoelectrochemical measurements were performed in a three way electrode system with Pt as counter electrode and Ag/AgCl as the reference electrode. The chronoamperometry and LSV data was obtained by using a potentiostat (Gamry Reference 3000). A solar simulator coupled with AM 1.5 filter and 300 W Xe arc lamp (Newport instrument) was used as a light source for generating one sun condition. Indeed, this lamp source is common for all the experiments that employed one sun irradiation conditions. By replacing AM1.5 filter with any other filters radiation with certain above wavelength can be generated and used for measurements. For example, by using 510 nm filter, wavelengths below 510 nm is prevented and all the wavelengths above 510 nm is allowed for reaction/measurements.

Calculation of PEC and Faradaic efficiency was determined as given below. The PEC of the solar driven hydrogen generation efficiency was calculated by the following equation

$$\eta = \frac{2 \times 0.21(V) \times N_{H2}(mol) \times 96485(C.mol^{-1})}{I(W.cm^{-2}) \times A(cm^2) \times t(sec)} \times 100\%$$

Where N_{H2} is the amount of evolved H_2 gas, A is the area of the electrode exposed to the light, I is the intensity of light and t is the time of reaction and 0.21 V represents the thermodynamic reaction potential for oxidation of sacrificial reagent. The Faradaic efficiency was calculated by the following equation.[16,17]

$$\eta_{faradaic} = \frac{2 \times N_{H2}(mol) \times 96485\ (C.mol^{-1})}{Q(C)} \times 100\%$$

where Q is the total amount of charge passed through the external circuit and N_{H2} is the amount of hydrogen produced in the same period of time.

2.6. Electrochemical characterization

2.6.1 Electrochemical characterization of $AuTiO_2$ based DSSC.

Cyclic voltammetry of dye N719 bound to TiO_2 anode with or without Au NPs was performed in 0.1 M tetrabutylammonium hexafluorophosphate in acetonitrile electrolyte. An electrochemical workstation (Gamry Reference 3000) was used in a standard three way electrode, consisting of a modified TiO_2 electrode as working electrode, Pt gauze as counter electrode, and an Ag/AgCl as reference electrode. The scan rate was set to be 100 mV/s.

Electrochemical impedance spectroscopy (EIS) was recorded over a frequency range of 1 to 50000 Hz with an AC amplitude of 6 mV and a DC voltage of 0.7 V by using electrochemical workstation (Gamry Reference 3000). The parameters were calculated from Gamry Echem Analyst software.

2.6.2. Electrochemical characterization of NiCu catalyst

The catalyst ink was prepared by using 5 mg of NiCu catalyst and dispersed in 1 ml of ethanol- water solution (80/20 v/v). Next, 40 µl of nafion solution was added and ultra-sonicated for 30 min. Then 5 µl of the dispersion was transferred onto the glassy carbon electrode acting as a working electrode. All the electrochemical characterization was performed on Gamry Reference 3000 potentiostat. The references electrode was Ag/AgCl (saturated KCl) purchased from CH instruments and the counter electrode was a Pt foil. All potential reported in this paper for electrochemical methods were referenced to a reversible hydrogen electrode by adding a value of (0.197 + 0.059 x pH) V. Electrochemical impedance spectroscopy data were collected in a frequency range of 10^6 Hz - 1 Hz at an HER over potential of 130 mV vs RHE.

2.6.3 Electrochemical characterization of MoS_2-mGO catalyst

The catalyst ink was prepared by taking 5 mg of MoS_2-mGO catalyst and dispersed in 1 ml of ethanol- water solution (80/20 v/v). Next, 40 µl of nafion solution was added and ultra-sonicated for 30 min. Then 5 µl of the dispersion were transferred onto the glassy carbon electrode acting as a working electrode. All the electrochemical characterization was performed with Gamry Reference 3000 potentiostat. The references electrode was Ag/AgCl (saturated KCl) purchased from CH instruments and the counter electrode was a Pt foil. All potential reported in

this paper for electrochemical methods were referenced to a reversible hydrogen electrode by adding a value of (0.197 + 0.059 x pH) V. Electrochemical impedance spectroscopy data were collected in a frequency range of 10^6 Hz – 0.1 Hz at an HER over potential of 150 mV vs RHE.

2.7. H_2 evolution in the wired and wireless configuration.

In the wired configuration the photoanode was dipped in a 250 ml three neck RB flask containing 100 ml of 0.25 M Na_2S and 0.35 M Na_2SO_3 (50/50 v/v) as sacrificial hole scavenger and Pt acts as a counter electrodes, and the H_2 evolution was studied at 0 V. The evolved H_2 was measured using GC (Agilent 7890A). The electrolyte was purged with N_2 for 30 min. before every electrochemical experiment to remove the dissolved oxygen. For the wireless configuration, 8 ml of the electrolyte was used in a 50 ml RB and the photochemical cell was just dipped in to the electrolyte with the front side being exposed to the light.

2.8. H_2 evolution in the wireless device with NiCu catalyst.

The photochemical cell was dipped in to 30 ml of the electrolyte containing 0.25 M Na_2S and 0.35 M Na_2SO_3 (50/50 v/v) as sacrificial hole scavenger in a 50 ml quartz RB flask and the front side being exposed to the light. The evolved H_2 was measured by inverted burette and no other gas evolution was confirmed by using GC (Agilent 7890A). The electrolyte was purged with N_2 for 30 min. before every electrochemical experiment to remove the dissolved oxygen.

References

1. A. A. Melvin, K. Illath, T. Das, T. Raja, S. Bhattacharyya, C. S. Gopinath, *Nanoscale* **2015**, *7*, 13477-13488.
2. K. K. Patra, C. S. Gopinath, *ChemCatChem.*, **2016**, *8*, 3294–3301.
3. B. Nikoobakht, M. A. El-Sayed, *Chem. Mater*., **2003**, *15*, 1957-1962.
4. L. Liu, S. Ouyang, J. Ye, *Angew. Chem. Int. Ed.* **2013**, *52*, 6689–6693.
5. B. Wu, D. Liu, S. Mubeen, T. T Chuong, M. Moskovits, and G. D. Stucky, *J. Am. Chem. Soc*. **2016**, 138, 1114−1117.
6. A. G. Corte´s, G. Diaz, R. Zanella, H. Ramirez, P. Santiago, and J. M. Saniger, *J. Phys. Chem. C* **2009,** 113, 9710–9720.
7. M. Murdoch, G. I. N. Waterhouse, M. A. Nadeem, J. B. Metson, M. A. Keane, R. F. Howe, J. Llorca and H. Idriss, *Nature Chem.*, **2011**, 3, 489-492.
8. W. S. Hummers, and R. E. Offeman, *J. Am. Chem. Soc.*,.**1958**, 80,.1339-1339.

9. X. Zheng, J. Xu, K. Yan, H. Wang, Z. Wang, and S. Yang, *Chem. Mater.* 2014, **26**, 2344−2353.
10. K. Sivaranjani, S. Agarkar, S. B. Ogale, and C. S. Gopinath, *J. Phys. Chem. C*., **2012**, 116, 2581–2587
11. B. O. Regan and M. Grätzel, *Nature*, **1991**, 353, 737-740
12. X. Wu, G. Q. Lu and L. Wang, *Energy Environ. Sci.*, **2011**, 4, 3565-3572.
13. K. K. Patra, B. D. Bhuskute, C. S. Gopinath, *Sci. Rep.*, **2017**, *7*, 6515.
14. R. Trevisan, P. Rodenas, V. Gonzalez-Pedro, C. Sima, R. S. Sanchez, E. M. Barea, I. Mora-Sera, F. Fabregat-Santiago, S. Gimenez, *J. Phys. Chem. Lett.*.**2013**, *4*, 141-146
15. K. Roy, C. P. Vinod, C.S. Gopinath, *J. Phys. Chem. C* 2013, **117**, 4717-4726.

16. C. Liu, J. Tang, H. M. Chen, B. Liu, and P. Yang, *Nano Lett., 2013,* **13**, 2989-2992.
17. R. Raja, P.Sudhagar, A. Devadoss, C. Terashima, L. K. Shrestha, K. Nakata, R. Jayavel, K. Ariga and A. Fujishima, *Chem. Commun.*, **2015**, 51, 522-525.

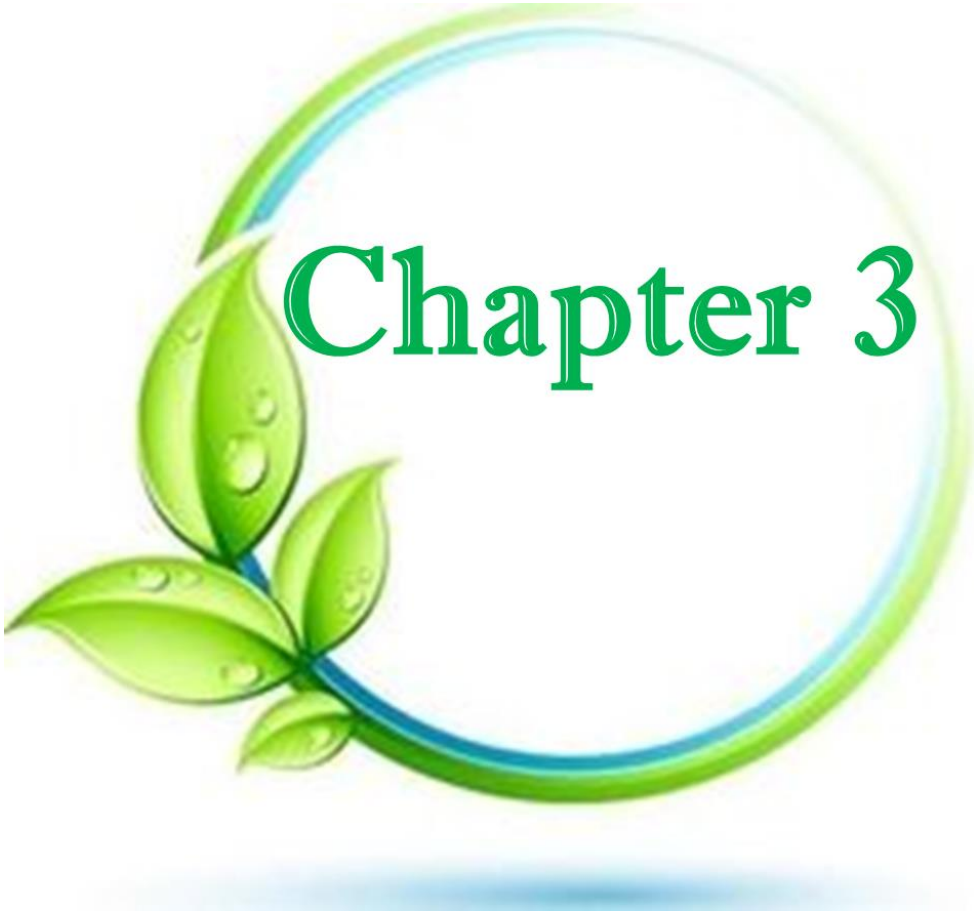

3A: Bimetallic and Plasmonic Ag-Au on TiO_2 for Solar Water Splitting : An Active Nanocomposite for Entire Visible Light Region Absorption

3B: Harnessing Near IR and Visible Light Photons through Plasmon Effect of Gold Nanorods with $AgTiO_2$

3C: Well Interconnected $AuTiO_2$ an Potential Candidate for High Efficiency Dye Sensitized Solar Cell: Role of Au LSPR on the Efficiency of DSSC

Part A: Bimetallic and Plasmonic Ag-Au on TiO_2 for Solar Water Splitting : An Active Nanocomposite for Entire Visible Light Region Absorption

3.1 Introduction

Solar energy conversion to chemical energy or power generation is and will be very likely to remain as one of the attractive and sustainable solutions to the global energy problems.[1-3] In spite of many efforts in the past few decades, we are yet to observe any breakthrough solution or advantage. It is known from the literature that some of the noble metal nanoclusters on semiconductors enhance the visible light absorption through surface plasmon resonance (SPR) and detailed mechanistic aspects has been addressed.[4,5] However, not many studies have been carried out to utilize the maximum visible light regime by using more than one noble metal simultaneously. According to literature reports, many bimetallic nanoclusters, where two different type of metals are present in a same particle, exhibited unique optical, catalytic and electronic properties.[6] This unique property makes them distinct from their monometallic counterparts. Therefore the photocatalytic activity of TiO_2, or any other suitable semiconductor, in the presence of visible light has been expected to enhance with bimetallic system, such as Ag-Au, Pt-Au. It is to be noted that both Ag and Au exhibit SPR at different wavelength regimes in the visible light. Although Pt-TiO_2 works in UV light due to appropriate conduction and valence band potential to split water, it does not work in direct/simulated sunlight due to high band gap (3.2 eV).[7] The charge carrier diffusion length is also one of the important limitations to achieve high photocatalytic activity. To address these two issues, fundamental requirement of solar light absorption in a broad range of visible light frequencies should be met along with electronic integration of light absorbing and redox site containing components. This could be possible by integrating plasmonic metal nanostructure, which is known to provide charge carriers through plasmonic effect to a suitable semiconductors, such as TiO_2.[8]

SPR or collective oscillation of electrons induced by visible light absorption is an optical property of nano particles such as Au, Ag, Cu and it depends on the shape, size, and dielectric constant of the surrounding medium.[9] These plasmonic NPs interact at different frequency of solar light and produce local electromagnetic field. The synthesis of bimetallic nanostructure provides an alternative pathway for enhancing the SPR wavelength regime. The Ag-Au bimetallic NPs absorb in a wide wavelength range of visible light.[10]Although many bimetallic

nanocomposite have been studied, Ag-Au system has particular advantage due to similar lattice constant (2.3/2.4 Å for Ag(111)/Au(111) facet), apart from SPR absorption features at different wavelength regime (around410-420 nm for Ag and 550 nm for Au NPs).[11] As a result of similar lattice constant they can form bimetallic nanostructures at wide range of compositions. However the integration of Ag-Au bimetallic NPs with TiO_2 is the crucial factor for photocatalysis or light harvesting applications. For the current study we evaluated an electronically integrated composite of Ag and Au with TiO_2, and particularly Ag-Au, to demonstrate the absorption of large fraction of solar light and solar water splitting (SWS). Ag-Au bimetallic system acts as a plasmonic nano antenna. Many studies have been made to enhance the photocatalytic activity of TiO_2 in the green (violet) region by the SPR absorption of Au NPs (Ag NPs) around 550 (420) nm;[12,13] however, the complementary wave length regime of solar spectrum was not utilized. Very likely, this is the first report to demonstrate an enhancement in photocatalytic activity by Au-Ag system.

Ag on Au-TiO_2 doubles the solar water splitting (SWS) activity (718 μmol/hg) than that of $AuTiO_2$ (366 μmol/h g) or $AgTiO_2$ (355 μmol/h g) for the same weight percentage of bimetal. Photocurrent measurement also shows an increase in the current density after silver deposition, indicating an improved light absorption capacity. Electronic integration among metal NPs and with TiO_2, and heterojunctions among them[14] is the key aspect for achieving high photocatalytic activity, and this has been fully supported by detailed studies.

3.2 Results and discussion

3.2.1 UV-Visible absorption studies

The UV-Vis absorption spectra of the silver deposited on $AuTiO_2$ and other relevant control materials are shown in Figure 3.1. x in xAgAuT indicates the Ag-content; 20, 40, 60 and 80 indicating photodeposition irradiation time in minutes resulting in 0.07, 0.14, 0.2, and to 0.27 wt % of Ag, respectively, in xAgAuT. The detail synthesis method has been discussed in experimental section 2.2.1 (chapter-2). Ag and/or Au-content were measured by ICP and EDX analysis. Inset photograph shows the change in color of AuT after Ag deposition to different extent. The AgAu bimetallic NPs shows one broad SPR band in the visible light range and the

wavelength at which maximum absorption (λ_{max}) occurs depends on Ag-Au composition. The visible light absorption between 500 and 650 nm is a result of SPR features of Au NPs. After silver deposition over $AuTiO_2$, peak broadening was observed towards the lower wavelength photons of violet-indigo-blue region. The SPR features of AgAuT composite cause more visible light absorption between 400 and 650 nm as compared to that of AgT or AuT. The broadening of the LSPR feature after silver deposition clearly shows an increase in the imaginary component of the

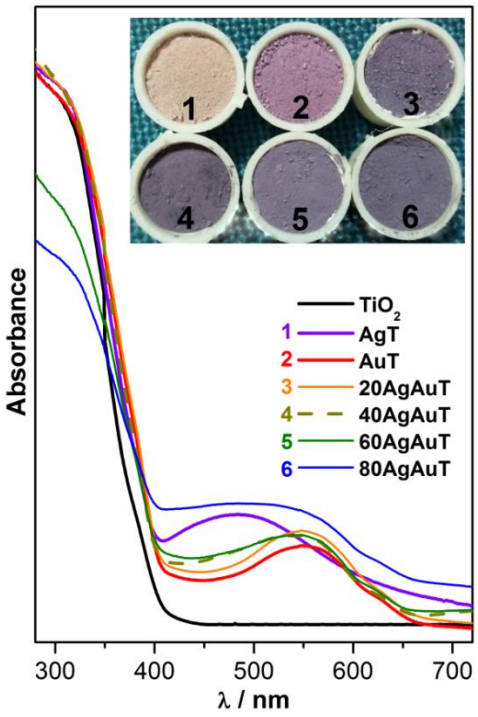

Figure 3.1. UV-visible absorption spectra of AgAuT as a function of Ag content with control composites. Change in spectral broadening with Ag-content in AgAuTis to be noted.Insetshows a digital photograph for the color associated with the composites (1) AgT, (2) AuT, (3) 20AgAuT, (4) 40AgAuT, (5) 60AgAuT, and (6) 80AgAuT.

dielectric function of metal. Hence silver deposition over AuT results in a faster rate of LSPR relaxation, which leads to the formation of hot electrons.[15] FWHM mostly associated with life time of the plasmonic excitation. High FWHM corresponds to rapid decay of surface plasmon excitation, which leads to formation of hot electron via Landau damping.[15] In addition, a careful comparison of the AgT, AgAuT and TiO_2 spectra reveals an overlap in light absorption by TiO_2 and Ag at 400 nm in the latter two composites hinting the light absorption below 400 nm by silver to a significant extent in AgAuT. Spectrum recorded for AgAuT confirms the same and

indicating a significant UV absorption by Ag. Absorption coefficient at 400 nm increases gradually with increasing Ag-content. Although light absorption is extended between 400 and 650 nm, more light absorption at 400 nm for 80AgAuT hinting the predominance of the Ag over Au at large amount of Ag deposition. It is also expected that by integrating with gold nanorod of appropriate aspect ratio, light absorption can be further extended up to 800-900 nm to utilize the entire visible and significant near IR regime.

3.2.2 PEC measurement

The PEC property of TiO_2, AuT, and 40AgAuT were studied in a three electrode system with Ag/AgCl as the references electrode and Pt as the counter electrode. Figure 3.2a shows the linear sweep voltammograms recorded in 1 M NaOH electrolyte solution under one sun condition (100 mW/cm^2). After silver deposition there is a significant increase in the current density of AuT. As compared to TiO_2 (25 $\mu A/cm^2$), and AuT (58 $\mu A/cm^2$), 40AgAuT electrodes achieved the highest photocurrent density of 95 $\mu A/cm^2$ at zero bias. Almost doubling of photocurrent generation after Ag-deposition on AuT, than AuT or AgT alone, highlighting the effective light harvesting by a combination of Ag and Au. This shows the positive role of AgNPs in enhancing the photoresponse of 40AgAuT composition.

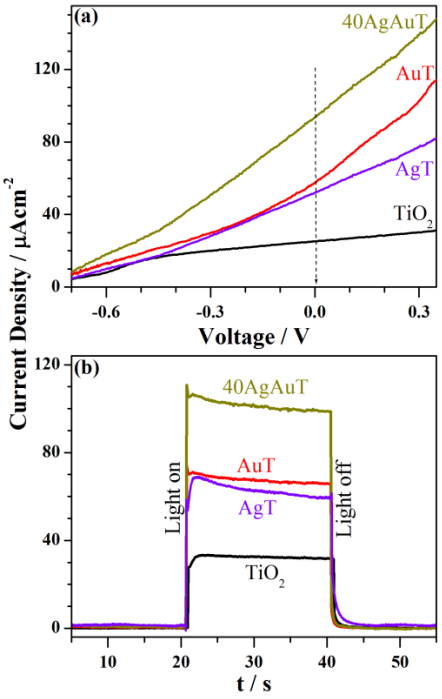

Figure 3.2. (a) Linear sweep voltammograms, and (b) chronoamperometry of bare TiO_2, AuT, AgT, and 40AgAuT electrodes measured in 1 M aqueous NaOH solution under one sun condition. Chronoamperometry was measured at zero bias.

The instant photoresponse of the AgAuT composite electrode was studied by chronoamperometry method. Figure 3.2b shows the water oxidation current with respect to time under chopped illumination at 0 V and the observed photocurrent density matches with that of values obtained from LSV. As shown in Figure 3.2b, after silver deposition on AuT, there is 150 % (300 %) enhancement in current density was observed as compared to that of AuT (TiO_2). AgT and AuT show very similar results in chronoamperometry and LSV. Generally the enhanced photocurrent is due to charge transfer from metal NPs to semiconductor. Moreover silver deposition over AuT increases the electron density around the AuNPs and the SPR excited form of bimetallic nanostructure enhances the electron transfer from bimetallic NPs to semiconductor.

3.2.3 Photocatalytic hydrogen evolution

The photocatalytic hydrogen evolution reaction was studied in 25 % aqueous methanol (v/v) solution under one sun conditions. Initially 0.1 to 0.5 wt % Au deposited on titania catalysts were prepared and evaluated for SWS and the results are shown in Fig. 3.3. The H_2 yield (HY) increases with increasing Au wt % up to 0.25 wt % and any further increase in Au-content decreases the HY. In view of this, 0.25 wt % Au on titania was chosen to be the optimum composition for all studies presented in this communication. Various amounts of Ag deposited catalysts were evaluated for SWS, and the results are shown in Figure 3.4. A gradual increase in (HY) from AuT to 40AgAuT was observed; further increase in Ag-content decreases the HY suggesting the necessity of an optimum Ag layer thickness for the best activity. Indeed, a marginal decrease in Au SPR intensity observed with 60 and 80 AgAuT composites (Fig. 3.1) suggest the light penetration might be a limiting factor. However, visible light penetration depth (or skin depth) calculation[16] indicates that it is of the order of microns for metal or bimetal, and much larger than the particle size shown in TEM results (see Fig. 3.9); this rules out the light penetration depth might be a limiting factor. Nevertheless, increasing particle size limits the metal-support interface, which in turn limits the number of Schottky junctions and hence a possible decrease in HY. Further, large loading of silver over Au-TiO_2 may increase the Ag deposition directly on TiO_2 and hence light absorption could be increasingly limited to the Ag

SPR at high Ag content. The highest HY was observed to be 718 μmolh^{-1}g^{-1} with 40AgAuT composite. HY observed with 40AgAuT is two times that of AuT or AgT. This represents the combined role of Ag + Au on AgAuT in solar light harvesting. However, a simple physical (1:1) mixture of AgT + AuT exhibits a HY 361 μmolh^{-1}g^{-1}, indicating the necessity of metal combination for high HY. The apparent quantum yield (AQY) was calculated using the formula given below:

$$\mathrm{AQY}(\%) = \frac{2 \times \text{number of H2 molecules}}{\text{number of incident photons}} \times 100 \qquad (1)$$

It is assumed that 21.5% of photons from 370 to 650 nm are incident on photocatalyst and possibly absorbed, which corresponds to 3.33 x 10^{19} photons per sec.[17,]It is also assumed that field effect and multiple exciton generation has no contribution to H_2 generation. According to equation (1) and with above assumptions, 40AgAuT shows the maximum AQY of 3.3 %.

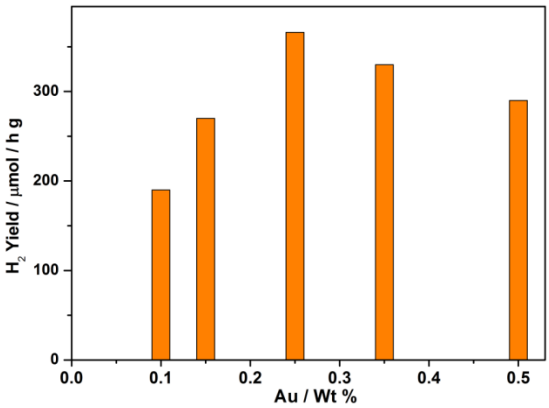

Figure 3.3: Au weight percent dependent hydrogen yield is shown for Au-TiO_2 composite catalysts.

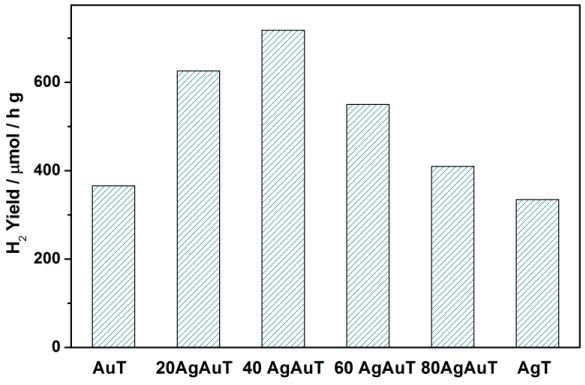

Figure 3.4.Photocatalytic H_2 evolution activity of AgAuT composite with different Ag loading in aqueous methanol solution under one sun condition measured by GC.

To study the plasmonic effect of Ag + Au on AgAuT, we measured the HY for 40AgAuT under different frequency range of visible light, and the results are shown in Figure 3.5a. This is also compared with that of AgT and AuT. In each experiment the water splitting reaction was continued for 4 h with periodical measurement. Illumination under one sun condition produces the maximum HY. However, surprisingly, HY decreases by 50-60 % with 400 nm cut-off filter ($\lambda \geq 400$ nm) compared to one sun conditions underscores the necessity to exploit the 4-5% of

UV-A available under one sun condition. The contribution from the silver SPR diminished fully for $\lambda \geq 500$ nm, while AuT and AgAuT shows very similar HY; Au SPR contribution towards SWS has been demonstrated with the above result.

Hydrogen evolution under one sun illumination as a function of time was measured and the results are shown in Fig. 3.5b.Experiment was conducted in 5 h cycles, and each cycle was followed by 30 min. degassing and 30 min. sonication to remove any dissolved gases. After 5 h of illumination, 40AgAuT produced about 3.6 mMol H_2. Same activity has been maintained for 24 h of irradiation. This underscores the photostability of nanocomposite.

Figure 3.6 shows the OWS activity of AuT and 40AgAuT without using any sacrificial agent. 70 and 16 µmol of H_2 was produced for 40AgAuT and AuT, respectively, after 10 hours of

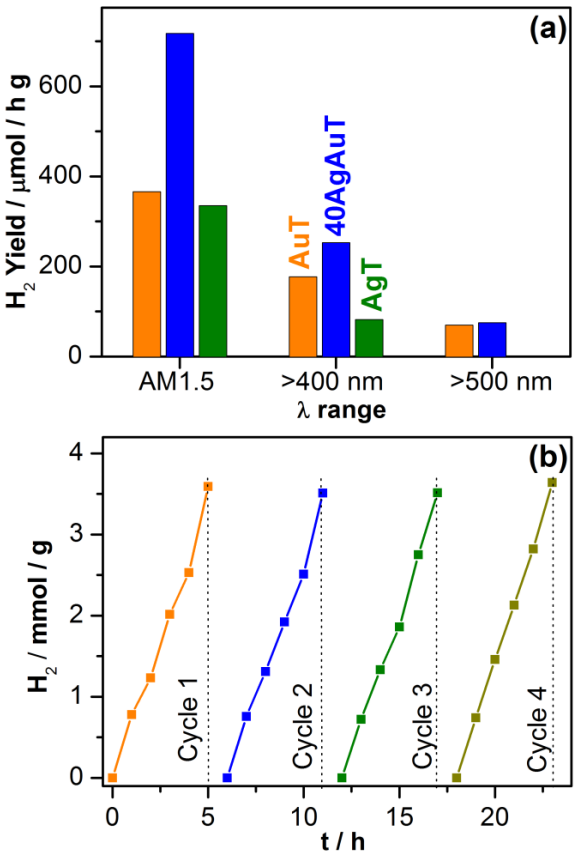

Figure 3.5. (a) Hydrogen yield with different frequency range of visible light. (b) Hydrogen production as a function of time for 40AgAuT under one sun condition.

irradiation under one sun condition. Although the HY observed was very poor, however, it demonstrates the activity without any sacrificial agent is to be underscored and its potential might be exploited. It is worth exploring similar catalyst with densely deposited nanoplasmonic clusters. Detailed characterization studies have been carried out to understand the nature of AgAuT nanocomposites for better SWS and PEC activity.

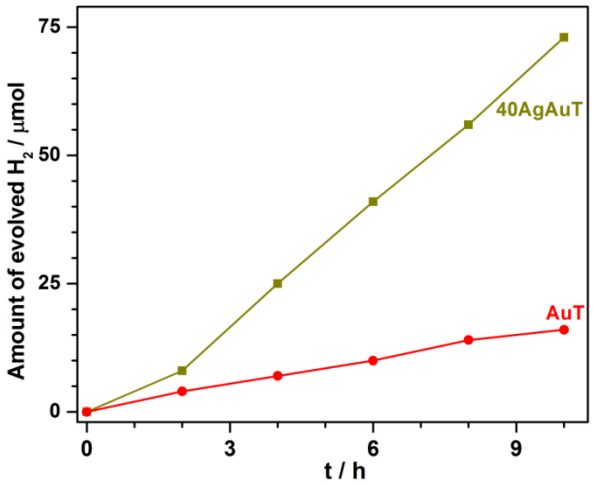

Figure 3.6: Hydrogen production from overall solar water splitting as a function time for 40AgAuT under one sun condition.

3.2.4 Photoluminescence studies

Figure 3.8 shows the PL spectra of TiO_2, AuT, AgT and AgAuT measured with an excitation wavelength of 350 nm. All the material shows the emission features around 415, 441 nm and a shoulder feature at 470 nm. The high intensity emission at 441 nm is a result of charge transfer from Ti^{3+} to the oxygen anion in $[TiO_6]^{8-}$ complex.[13] The free exciton emission of TiO_2 corresponds to the 415 nm emission feature. The PL intensity decreases to one third of TiO_2 after metal NPs deposition. AgT also show similar emission spectrum as that of AuT or 40AgAuT. Any electron or energy transfer from metal NPs due to near field to titania is expected to increase the emission intensity further. However lower emission intensity rules out the same. The decrease in emission intensity after metal NPs deposition is attributed to the result of easy separation of electron hole pair, which is likely to occur at the Schottky junction.[17] The presence of Schottky junction was further supported by detailed HRTEM studies.

3.2.5 Raman studies

The structural features of the composite were studied by Raman spectra. Figure 3.7 shows the Raman spectra of TiO_2, AuT, AgT and AgAuT. All the six Raman active modes are observed at 150 (E_g), 198 (E_g), 398 (B_{1g}), 516 ($A_{1g}+B_{1g}$) and 640 cm^{-1} (E_g), and they are characteristic features of anatase TiO_2. It is already well reported[14] that the crystalline anatase (101) facet interact with the Au NPs which leads to frequency shift in the Raman spectra.

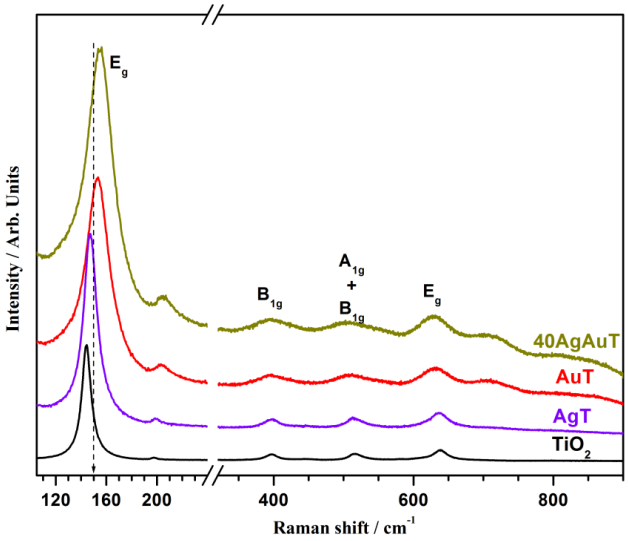

Figure 3.7. Raman spectra of TiO_2, AuT, AgT and AgAuT composites; latter three composite show blue shift with increased line broadening after metal deposition.

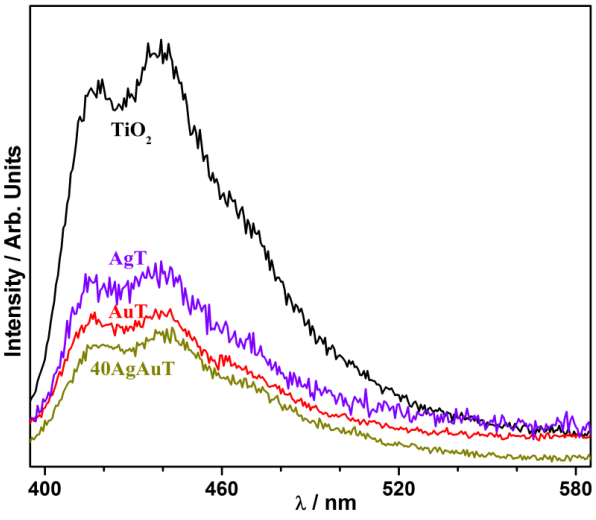

Figure 3.8. Photoluminescence (PL) spectra of TiO_2, AuT, AgT and AgAuT. The PL intensity drastically decreases after metal NPs deposition, indicating the electronic interaction between Au and TiO_2.

There are two modes of enhancement observed in the surface enhanced Raman scattering (SERS). The electromagnetic component is the major enhancement factor for SERS, which occurs through the excitation of the surface plasmons of metal nanoparticles; second factor is due to chemical enhancement which is attributed to molecular interaction between the metal surface and the adsorbed molecule. The strong interaction between metal surface and the molecule, results in change in the symmetry of the molecule due to bond formation on the metal surface. This leads to a frequency shift between SERS and the normal Raman spectra of the molecules.[18] TiO_2 show typical vibrational features at 145cm^{-1} for E_g band. As shown in Figure 3.7, peak shift as well as peak broadening was observed after gold deposition on TiO_2; this is attributed to a change in chemical environment around Au particles on TiO_2. A new broad feature was observed

between 690-720 cm^{-1}, after Au or AgAu deposition on titania. It is also to be noted that this new feature was not observed for TiO_2 or AgT.[19] We attribute the broad feature around 700 cm^{-1} may be due to overtone of B_{1g} feature; however, this needs further verification. The strong molecular interaction between gold NPs and TiO_2 can also be seen from the TEM images, where the Au NPs are in direct contact with TiO_2.The intensity of all Raman bands increase because of SPR of gold. The peak shift as well as broadening has been retained after silver deposition over AuT. Unlike AuT, AgT shows less broadening and marginal shift in Raman feature; however, intensity enhancement between 2-3 times due to SERS effect of Ag is evident. Large shift observed in AuT and AgAuT is predominantly due to Au and silver deposition over AuT is attributed to electronic integration of Ag and Au with TiO_2. The selective deposition of Ag over gold NPs is attributed to the bimetallic interaction because of similar lattice constant.[11]

3.2.6 TEM studies

The morphology and microstructural property of the AuT, AgT and 40AgAuT nanocomposites was studied by TEM (Figure 3.9).TEM image of AuT is shown in Fig. 3.9a. Fig. 3.9b shows HRTEM image centered around the single gold nanoparticle, shown in Fig. 3.9a. Uniform d = 0.24 nm value observed throughout the particle suggests the gold particle grew along (111) facet; nearby TiO_2 particle exhibits (101) facet. Indeed gold particle is embedded or flanked between two TiO_2 particles is abundantly evident from Fig. 3.9b. Ag particle shown in Fig. 3.9c from AgT exhibits irregular shape with d = 0.23 nm indicating the growth along (111) facet.

Fig. 3.9d shows a TEM image 40AgAuT. Indeed metal particle decoration occurs on few TiO_2 particles and many of them are bare particles. Total metal weight % $\leq$0.5 limits the metal particle decoration to limited number of titania particles. Enlarged and high resolution TEM image of a particle observed in Fig. 3.9d is shown in Fig. 3.9e and further amplified in Fig. 3.9f. Two distinct d-values were observed within a single particle; one in the middle of the NP where the particle grew in one direction and the other at the surface of the NP, where the top-layers are grown in different direction. This is attributed to the deposition of silver on the surface of AuNP. Thin layer of Ag coating on Au particles makes it as core-shell morphology with Au in the core. In fact, with best of our efforts, we did not find isolated Ag particles on 40AgAuT, although it is

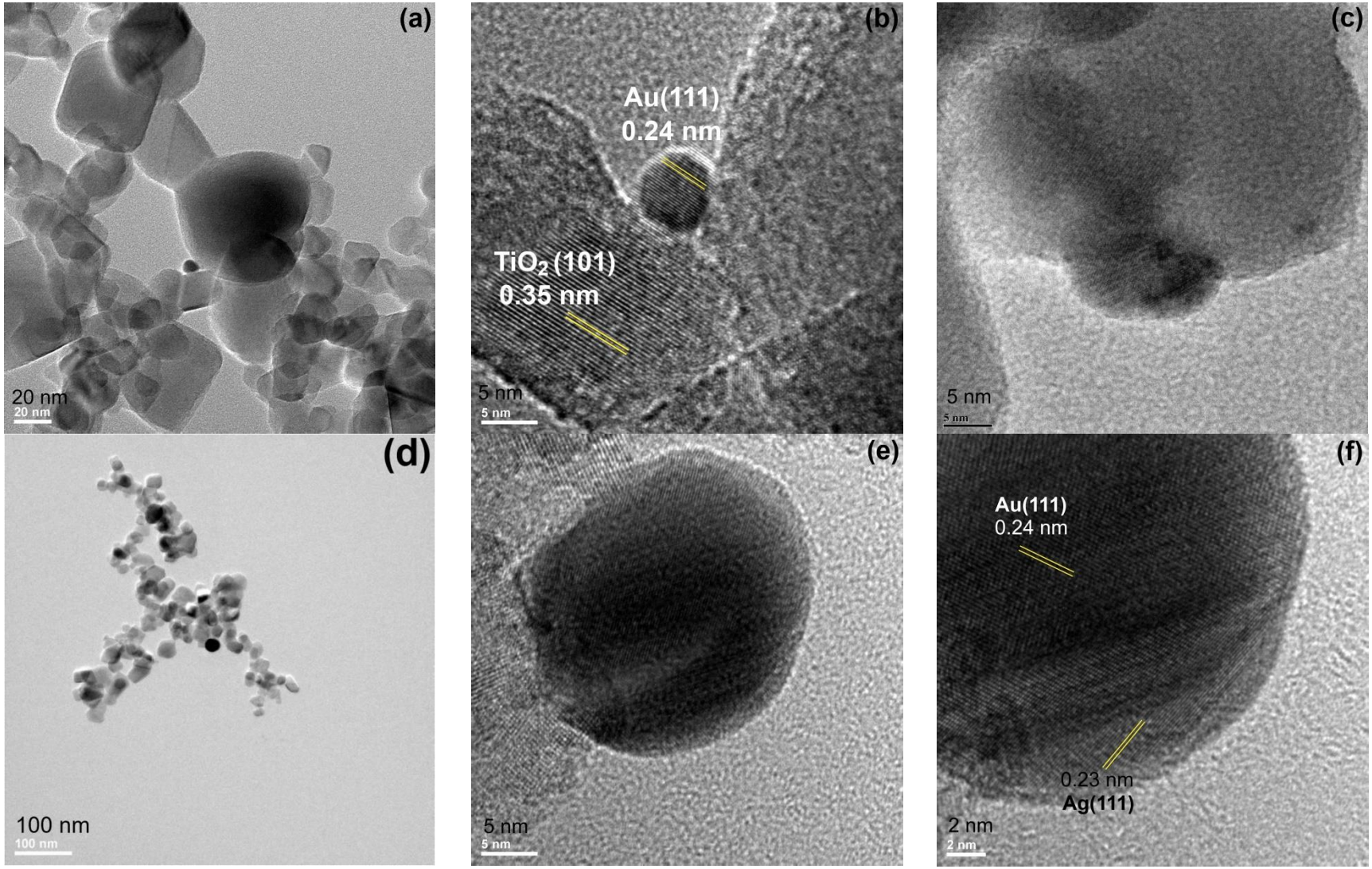

Figure 3.9. TEM image of (a) AuT, and (d) 40AgAuT composites are shown. HRTEM image of (b) AuT, (c) AgT, and (e and f) 40AgAuT composites are shown. Single Au particle observed in the center of the panel a is shown at high resolution in panel b. AuT shows spherical Au particles, whereas AgT shows irregular shape. Ag deposition on Au in 40AgAuT is evident from the different d-values observed in HRTEM images in e and f. Irrespective of single or bimetal, heterojunction was observed between metal and TiO_2.

possible statistically. From the literature it is well known that the binding of Au and Ag is highly favorable because of bimetallic or alloy interaction; such bimetal/alloy formation might be a driving force for predominant Ag deposition on Au. The measured d spacing at the center of the NP is 0.24 nm which corresponds to the (111) facet of Au, and the same at the edges is 0.23 nm (Fig. 3.9f), corresponding to (111) plane of Ag.

The energy dispersive x-ray (EDX) spectrum of the composite recorded (Fig 3.10) from the same region of the composite indicating the presence of both Au and Ag. It is somewhat difficult to distinguish Au and Ag from the d spacing value alone due to very similar structure; nevertheless, a combination of HRTEM and EDAX supports the bimetallic or alloy nature of Ag-Au. However the preparation method adopted to prepare the composite and the difference in crystal growth pattern shown in TEM image, indicates that Ag is interacting preferentially with Au in AgAuT composite. Consequently, the silver ions would be reduced on the surface of AuNPs which acts as a seed or active sites for its growth.[20] As shown in Figures 3.9b, 3.9c, 3.9e-f the metal-semiconductor heterojunction was observed with all composites, where the (111) facet of metal is in direct contact with (101) facets of several particles of anatase TiO_2. This heterojunction is an essential feature for easy separation of charge carrier at the metal-semiconductor interface. Another advantage of Au-TiO_2 heterojunction is the generation of charge carrier near the surface of TiO_2 through plasmonic effect, which helps for charge separation and charge utilization through redox reactions.

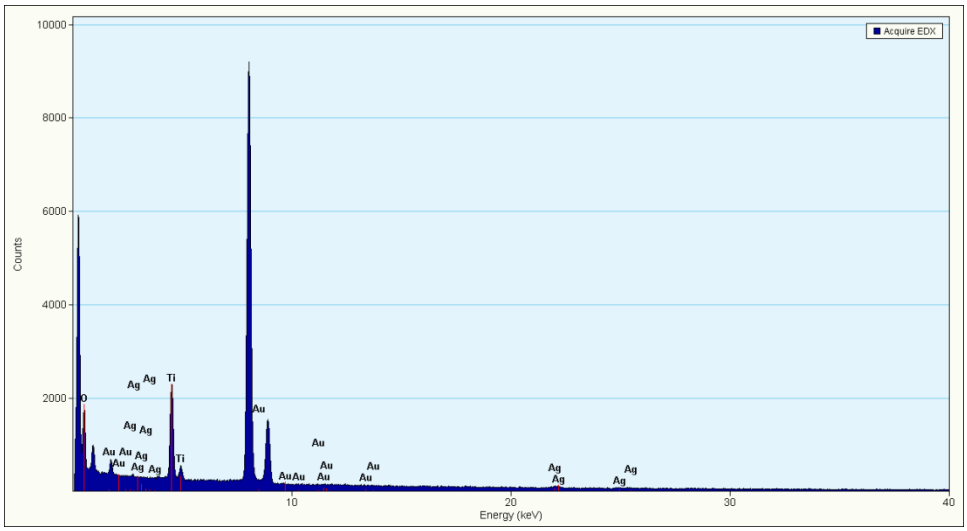

Figure 3.10: EDX spectrum measured on 40AgAuT composite demonstrates the presence of both Ag and Au along with titania.

3.2.7 XPS

The XPS spectra were recorded for Ti 2p, and Ag 3d core levels, and the results are shown in Fig. 3.11a and b, respectively. Ti $2p_{3/2}$ core level appears at 459.4 eV for TiO_2, which is in good correspondence with the earlier results.[21] however, there is a large shift by 1.0-1.2 eV to lower binding energy was observed with Au or AgAu deposited catalysts. Indeed, this observation fully demonstrates that there is Fermi level equilibration between metal or bimetal with titania. Very likely, this helps for an effective electron transfer between noble metal and conduction band of titania. Shift towards higher wavenumber and peak broadening observed in Raman results are in good agreement with the above electronic interaction. However, there is no significant change in the oxidation state of Ti in any of the catalysts and predominant Ti^{4+} was observed on all catalysts. Presence of any Ti^{3+} would show a feature around 457 eV,[5b,22] which is not the case with the present composites.

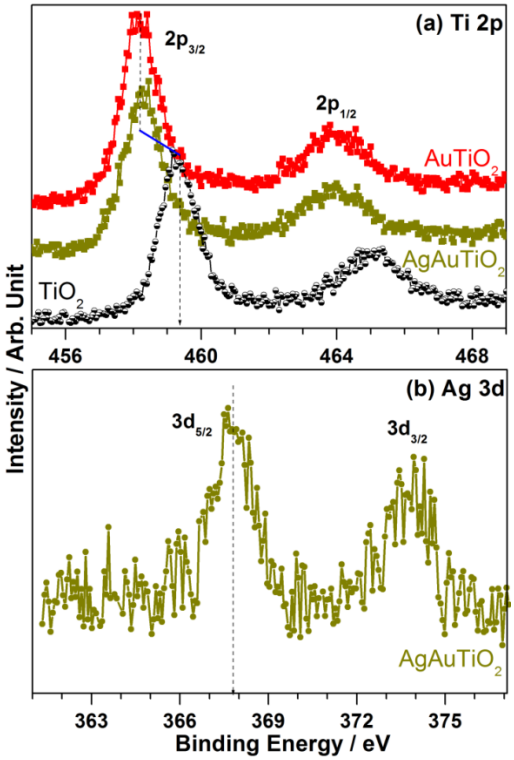

Figure 3.11: XPS results recorded for (a) Ti 2p, and (b) Ag 3d core levels for composites. Note a shift to lower binding energy observed with Ti 2p core level, after metal deposition.

Ag 3d core level recorded for AgAuT catalyst shows Ag $3d_{5/2}$ core level feature at 367.8 eV. This is very characteristic for metallic silver.[23] Metallic silver feature indicates that the silver in Ag-Au bimetal is less prone to oxidation. Catalyst that was used for water splitting measurement also shows no change in BE indicates that silver surface is robust against oxidation.

3.3 Mechanism

Based on the experimental data available for the AgAuT composite, and the mechanistic aspects discussed in the literature for noble metal composites,[24] possible mechanism is proposed in Fig. 3.12. There are two possible mechanisms reported in the literature for the plasmonic contribution towards enhancing water splitting activity. First one is through resonance energy transfer (RET) and other is the direct electron transfer (DET) from metal to semiconductor.[25]The RET mechanism takes place when the metal and semiconductor is not in direct contact with each other. This mechanism is mostly dominated in physical mixture of metal NP and semiconductor. DET is likely to occur, when metal and semiconductor is in direct contact with each other but we cannot rule out the energy transfer in this case. HRTEM and PL results show the direct contact between Au and TiO_2, which favor the DET from metal to semiconductor. Upon visible light absorption the bimetallic plasmonic nanostructure excite to its surface plasmon (SP) state, as shown in Figure 3.12. DET from SP state to the TiO_2 conduction band occurs, as its energy is

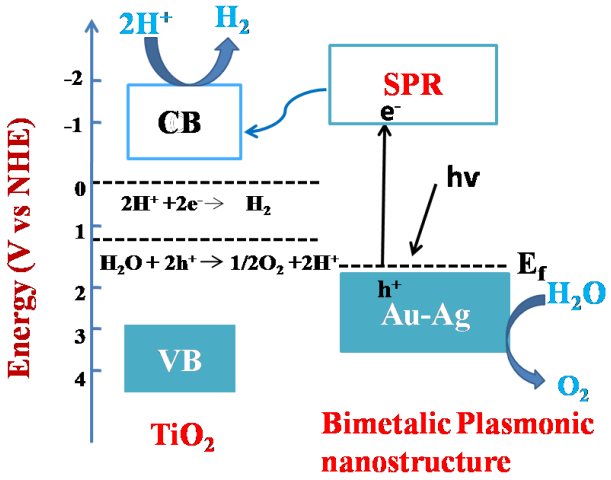

Figure 3.12: Possible mechanism of SPR induced charge transfer for the photocatalytic H_2 production from pure water in AgAuT composite. Energy level shown may be considered as guide on NHE scale.

lower than metal SPR state and deposition of silver over AuT enhances the electron transfer process. Finally the hydrogen evolution half reaction takes place at TiO_2 conduction band and oxidation occurs on Au or Au-Ag surfaces.

3.4 Conclusion

Present study shows that predominant absorption of visible light regime by using more than one plasmonic metal on titania for improved solar water splitting. It is to be emphasized that electronic integration among the constituent components is the key aspect for better solar light harvesting. The electronic integration of Au, Ag with TiO_2 was supported by the Raman spectroscopy and TEM analysis. As evident from TEM, the (111) facets of nano Au binds directly to the (101) facets of TiO_2, and forms a heterojunction, which favors charge separation and utilization. As a result of Ag deposition over AuT, the light absorption capacity of composite material increases and the electronic nature of the Au-TiO_2 heterojunction remain un-altered. The H_2 production activity doubles due to more light absorption between 400 and 500 nm due to Ag in 40AgAuT, compared to AuT. It is also to be emphasized that our attempts to increase the density of nanometal clusters does not work out, rather the particle size increases. However, more number and highly dispersed plasmonic metal particles on semiconductor could be a possible approach to increase the efficiency of solar water splitting and specific synthesis efforts are required in that direction. Different preparation methods might be adopted to increase the density of plasmonic nanometal clusters for improved SWS activity.[26]

Part B: Harnessing Near IR and Visible Light Photons through plasmon Effect of Gold Nanorods with $AgTiO_2$

3.5 Introduction

In the not-so-distant future, photocatalytic solar hydrogen evolution (SHE) could become one of the promising method for solar light harvesting towards the production of carbon free clean fuel such as hydrogen, and reduction of CO_2 to fuels/chemicals.[27,3] Among the many semiconductors, TiO_2 is the most extensively studied semiconductor due to its rightly positioned valence band (VB) and conduction band (CB) for oxidation and reduction half reactions of water, respectively.[1,28] However, TiO_2 has a critical limitation, which is the limited light absorption to UV region ($\leq$ 380 nm) and hence an effective utilization of sunlight was not possible.[7] Many strategies were developed to overcome this limitation, such as sensitizing wide band gap TiO_2 with a narrow band gap semiconductor, like CdS, CdSe, and by doping metal and non-metal ions.[29] Apart from this, very less work has been reported on the utilization of the visible light with high λ or low photon energy ($\lambda \geq 550$ nm) and near IR (up to 1000 nm), which constitute almost half of solar spectrum for photocatalytic solar water splitting (SWS) reaction. Cui et al has reported a WO_2-Na_xWO_3 hybrid material for IR driven photocatalytic hydrogen evolution.[30] This hybrid absorbs only near IR region and hence the activity is very low for SHE. Stucky et al. demonstrated 11.6 μmol $h^{-1}g^{-1}$ of H_2 in visible light with AuNR-TiO_2 nanocomposite system.[31] A direct utilization of the photons available (<1000 nm) in sun light has not been achieved so far with a single photocatalyst material. To overcome this limitation, design of composites which absorb both in the visible light and near IR region is highly desirable for SWS reaction.

The recent development of plasmonic metal with a semiconductor nanocomposite has given a new direction to the photovoltaic and photocatalytic applications, where charge carriers can be generated on semiconductor surface through decay of localized surface plasmon.[8] Nanoparticles of Au, Ag, Cu which interact strongly with visible light photons due to localized surface plasmon resonance (LSPR) has been considered as a photosensitizer. It has been proved that charge carrier can be either injected directly into the semiconductor surface through decay of surface plasmon, which formed hot electrons; alternatively, field effect observed due to LSPR could also transfer energy through radiative energy transfer. Both processes are known to improve the

performance of the semiconductor in the visible region.[8,32] In both cases, not only the light absorption but also an electronically integrated metal semiconductor interface is very much essential for effectively harvesting photons in plasmonic composite photocatalyst.[13,17,33,34] Another attraction of plasmonic NPs which makes them so special from other class of material is the shape and size dependent optical property.[35] By tuning the shape and size of the plasmonic NPs, especially the longitudinal component, it is possible to harvest longer λ photons of the solar spectrum.[36] Tremendous effort has been made in the recent past to improve the light absorption in the blue and green region of the solar spectrum, however, very less effort has been made to utilize the red and near IR region (630-1000 nm) for SWS.[37]

In the current study, we demonstrate the absorption of visible light and near IR photons and SHE with an electronically integrated $AgTiO_2$-AuNR composite. Silver is responsible for harvesting high energy photons in the violet-blue region, and AuNR is responsible for harvesting the low energy photons in green to near IR region. At present, the major hurdle in the AuNR-TiO_2 system, for the SWS application, is the surfactant removal from the AuNR surface without applying any high temperature calcination. The surfactant molecules at the interface of the AuNRs and TiO_2 is known to hinder the charge transfer (CT) property between metal NPs and semiconductor.[38] The CT is affected because of the low conductivity of organic component and the significant distance between AuNP and semiconductor due to the interleaving surfactant molecules; this decreases the intensity of LSPR induced electromagnetic field near to semiconductor and hence the full advantage of plasmon effect was not utilized for applications. These fields are nonhomogeneous in nature and the intensity is the maximum at the surface of the metal NPs and decrease exponentially with distance from the surface. Liu et al has proposed the surfactant removal by $HClO_4$ treatment without change in AuNR morphology.[38] Certainly calcination is the easy procedure to remove the surfactant completely; however, it cannot be applied to plasmonic metal nanoparticle of specific morphology, such as AuNRs, which undergoes thermal reshaping even at 50 ^{0}C.[39] More over a physical mixture of AuNR and TiO_2 is not a good option for achieving high photocatalytic activity due to the lack of junctions between them. However there are few reports, where photocatalytic hydrogen evolution has been reported with TiO_2-AuNR under one sun condition[31,40,41] nonetheless, there is no report available in the literature for hydrogen evolution with $\lambda \geq 550$ nm light irradiation.

It is well known that silver and gold can bind easily due to similar lattice constant. In this report, SHE has been achieved exclusively with low energy photons ($\lambda \geq 550$ nm) by using AgNPs as a medium for transfer of generated hot electrons in AuNR to TiO_2. Under one sun condition, the highest H_2 generation activity (1097 μmol $h^{-1}g^{-1}$) was achieved with AgT-AuNR690 composite, which shows absorption maximum for Au NR at 690 nm. The same catalyst under $\lambda \geq 550$ nm light irradiation show 7 μmol $h^{-1}g^{-1}$ of H_2 production. However TiO_2-AuNR shows no activity towards H_2 production with $\lambda \geq 550$ nm and this indicates the importance of silver deposition over TiO_2 for utilization of the low energy or high wavelength photons. Present report is a part of ongoing efforts in our laboratories to exploit a variety of materials, including plasmonics, for organic conversion[14,19a] and efficient SWS[13,17,33,34] and reactions.

3.6 Results and Discussion

3.6.1 UV-Vis Spectra

Au NR with four different aspect ratio (length to diameter ratio) was synthesized by seed mediated method (see experimental section 2.2.2). UV-Visible absorption spectrum recorded for Au NRs are shown in Fig. 3.13a. The asymmetrical nature of Au NR splits the plasmon resonance frequency in to two modes; one along the transverse axis and another along the longitudinal axis. The polarization along the transverse axis shows a narrow and low intensity plasmon resonance peak at 520 nm, and the polarization along the longitudinal axis shows a high intensity and broad plasmon resonance peak at higher λ, which strongly depends on the aspect ratio of NR. As shown in Fig. 3.13a, the longitudinal plasmon resonance shifted to the higher wavelength with increasing silver content. Cetyltrimethylammonium bromide (CTAB) molecules gets adsorbed rapidly on the (100) facets (periphery of nanorod), as compared to (111) facets at the tip of nanorods. Once the (100) facet is confined by CTAB micelle, it restricts the growth and further growth become faster on the (111) facets.[42] As a result growth takes place longitudinally and the length of the nanorod increases. Jana et al has proposed that Ag^+ adsorbed on the gold particle surface as AgBr and restrict the growth.[43] Hence different aspect ratio of AuNR can be generated by changing the Ag^+ concentration.

The as-prepared Au NR shows a colour change (inset in Figure 3.13a) with increase in silver ion concentration. With increasing aspect ratio, the emission (or colour) changes from blue to red from 1 to 4, respectively. Gold nanorods are denoted as AuNR645, AuNR690, AuNR710, AuNR770; numbers given in the material code (645-770) corresponds to the longitudinal. plasmon absorption maximum at 645, 690, 710, 770 nm, respectively. A change in colour from light pink to purple was observed after AuNR incorporation in to AgT, as shown in Figure 3.13.

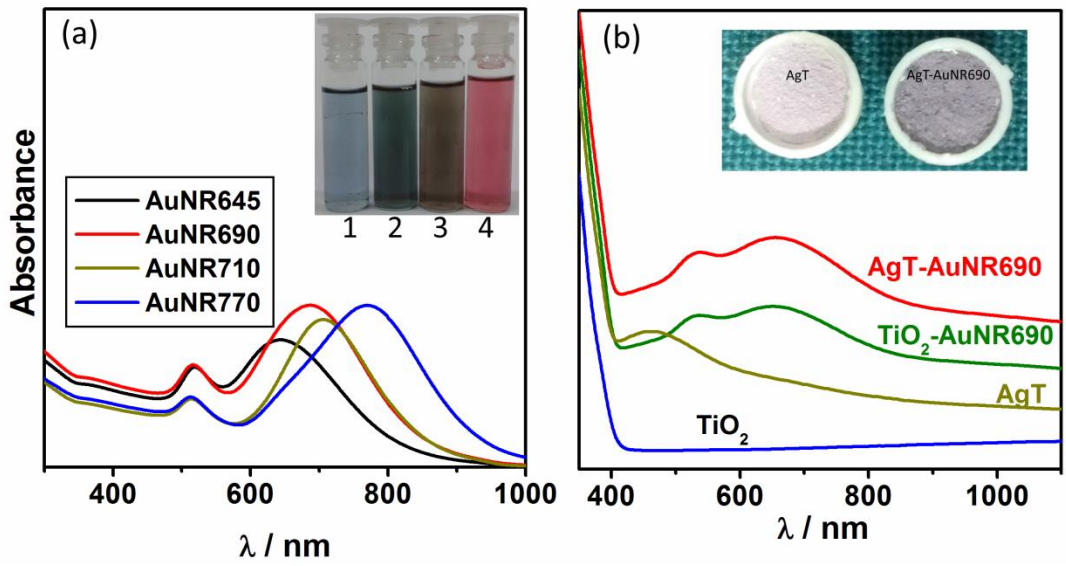

Figure 3.13. (a) UV-visible absorption spectra of different aspect ratio of AuNRs and inset displays a change in colour with increase in aspect ratio of Au NR. 1, 2, 3 and 4 in the inset correspond to the longitudinal absorption maximum of AuNRs at 645, 690, 710, and 770 nm, respectively. (b) UV-visible absorption spectra of TiO_2, AgT, TiO_2-AuNR690 and AgT-AuNR690. Composite colour of AgT and AgT-AuNR690 are given in inset.

Link and El-Sayed devised a method to calculate the aspect ratio of nanorods from the UV-Vis absorption maximum.[44] This method was adopted to calculate the aspect ratio in the present case; a gradual increase in aspects ratio was observed from 2.36 (AuNR645), 2.84 (AuNR690), 3.05 (AuNR710), to 3.68 (AuNR770). The UV-visible spectra of AgT show a broad plasmon absorption band between 400 and 480 nm (Figure 3.13b). Four TiO_2 and four AgT supported AuNR were prepared by loading different aspect ratio of NR. The longitudinal and transverse plasmon resonance of AuNR is also visible after incorporation of TiO_2 and AgT. Representative

results for TiO_2-AuNR690 and AgT-AuNR690 are shown in Figure 3.13b. However, the plasmonic features are broadened in the solid state, compared to liquid state spectra.

3.6.2 TEM analysis

TEM analysis of gold nanorods was made and the results are shown in Figure 3.14. A systematic increase in the aspect ratio from AuNR645 to 770 was observed. A careful analysis also reveals that the length of the NR increased from AuNR645 to AuNR690 with an increase in diameter too. However, thereafter, a marginal decrease in the diameter along with an increase in the length of the AuNR was observed.[44] A linear increase in aspect ratio was observed in TEM (2.23 to 3.86) as well as UV-visible spectral results (2.36 to 3.68) are to be noted. This hints the contribution from longitudinal component increases at the expense of transverse component. A simple comparison of area under the transverse and longitudinal absorption in Fig. 3.13a correlates well with the above observation. A significant decrease in the transverse absorption area was observed, while the same under longitudinal absorption increased from AuNR690 to 770. HRTEM analysis shows the (200) planes on the longitudinal axis of AuNRs.

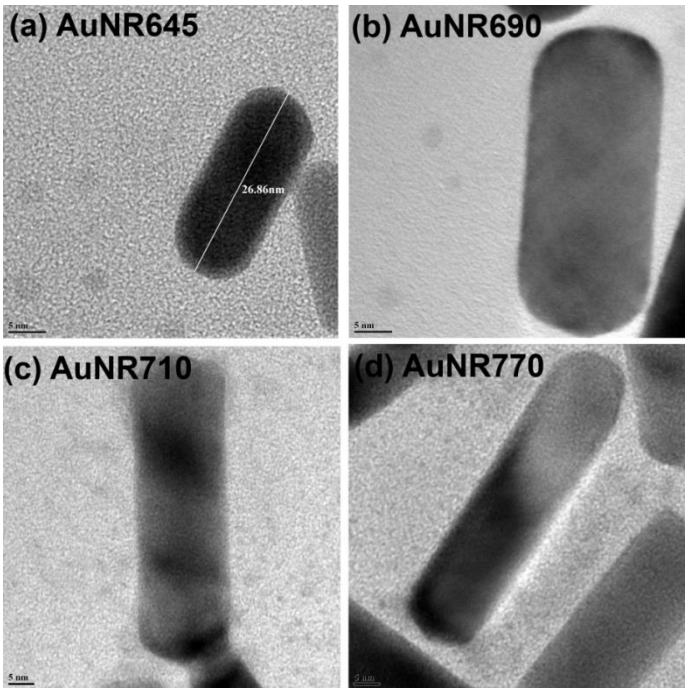

Figure 3.14: TEM images of AuNR are shown for four different aspect ratios, namely (a) AuNR645 (aspect ratio - 2.23), (b) AuNR690 (2.42), (c) AuNR710 (3.41), and (d) AuNR770 (3.86). Scale bar in all of the images is 5 nm.

The morphology and microstructural property of the AgT-AuNR-x (x = 645, 690, 710, 770, corresponding to longitudinal absorption maximum of AuNR) nanocomposites was explored by HRTEM and the results are shown in Figure 3.15. Fig. 3.15a, b shows the HRTEM image of AuNR, AgNP and TiO_2 particles in AgT-AuNR690. It is known that the (111) facets of Ag shows a favorable binding interaction with (101) planes of anatase TiO_2.[14,19a] AuNR morphology was found to be intact in the AgT-AuNR-x composites in the solid state (Fig. 3.15a) and exactly as that of the morphology found in solutions (Figure 3.15).. The formation of metal-semiconductor hetero junction (Schottky junction) was formed at the interface of AgNP and TiO_2, which is an essential feature for energy transfer in the plasmonic composite photocatalyst as shown in Fig. 3.15b.

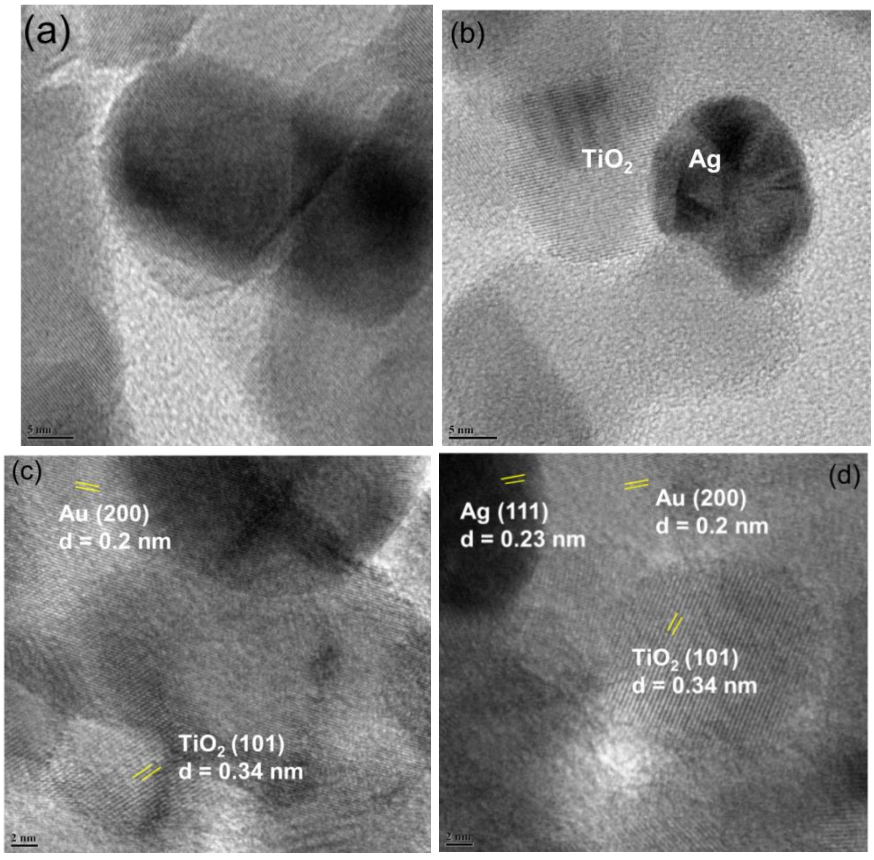

Figure 3.15: HRTEM image of (a) TiO_2-AuNR, and (b) AgT composites are shown. The heterojunction between AgNPs and TiO_2 is demonstrated from the TEM image. (c and d) AuNR deposited on AgT is evident from the d value shown in HRTEM images. Note the junctions observed between all three components of Ag, TiO_2 and AuNR in panel d.

The measured d-spacing of 0.2 nm corresponds to the (200) facet of AuNRs, and 0.23 nm (Fig. 3.15c, d) corresponding to (111) plane of AgNP. HRTEM images demonstrate the junctions

between Ag and Au as well as with titania and supports the integration aspects of all components. Figure 3.16 shows the energy dispersive x-ray (EDX) spectrum of the composite indicating the presence of both Au and Ag. The surface morphology of the AgT-AuNR was studied by scanning electron microscope (SEM), where the porous nature of the TiO_2 is clearly seen from the SEM image as shown in Figure 3.17.

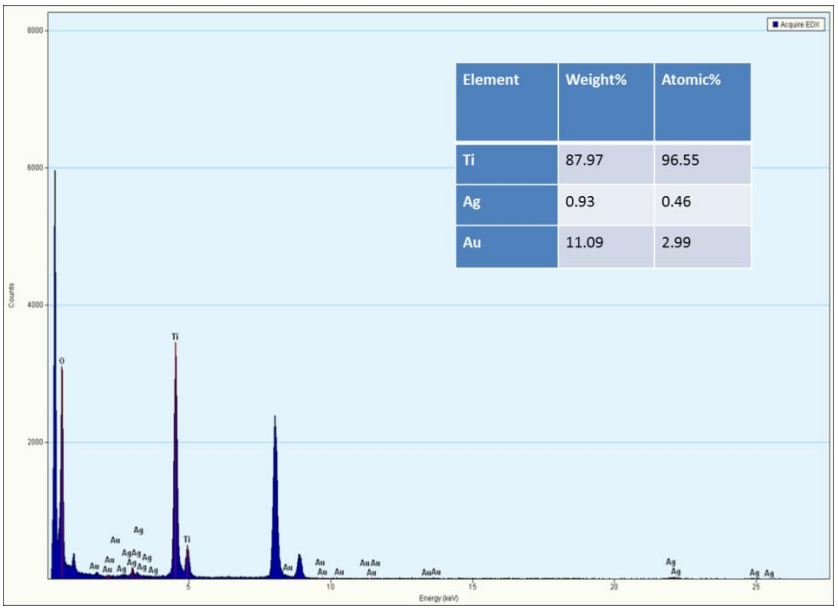

Figure 3.16: EDX spectrum measured on AgT-AuNR690 composite demonstrates the presence of both Ag and Au along with titania. Inset shows the atomic and weight% of different elements presents are given in the table.

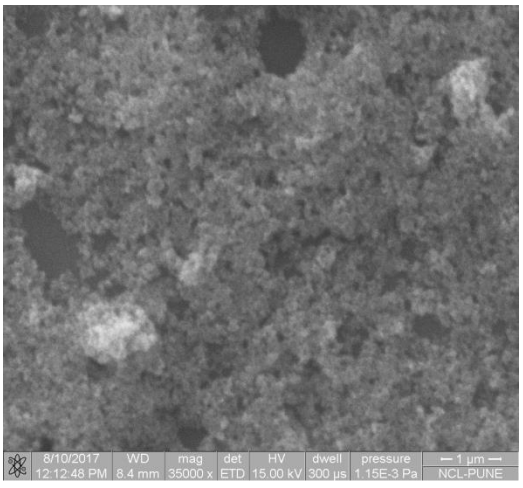

Figure 3.17: SEM analysis on AgT-AuNR690 composite demonstrates the porous nature of titania.

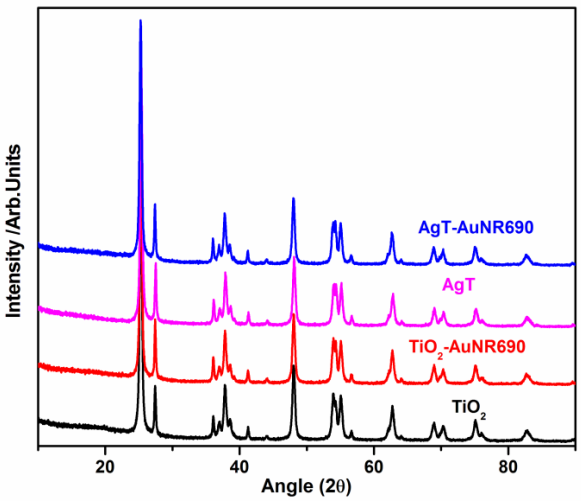

Figure 3.18: XRD pattern of TiO_2, TiO_2-AuNR690, AgT and AgT-AuNR690.

3.6.3 Raman spectroscopy

Raman spectroscopy is a versatile tool to study the structural features as well as the electronic environment of the plasmonic nanocomposites. It has been discussed in sec. 3.1 and earlier reports that deposition of plasmonic metal NPs, like Au and Ag, change the electronic environment surrounding TiO_2 and the same reflects in the surface enhanced Raman spectra (SERS).[17,33-36]It was shown that anatase (101) facets exhibit a favorable binding interaction with Au and Ag NPs which leads to frequency shift in the Raman spectra.[17a] The XRD results of the as synthesized sample indicates the anatase face in TiO_2 as shown in Fig. 3.18. However, because of the low content of Ag and AuNR in the composite material, no peaks correspond to Ag and AuNR was observed in XRD. TEM and HRTEM images of pure TiO_2 are shown in Figure 3.19 further supported the XRD results. Abundant anatase (101) facets available on titania is supported by TEM results. As shown in Figure 3.20, anatase TiO_2 shows six different type of vibrational features appears at a frequency of 145 (E_g), 198 (E_g), 398 (B_{1g}), 516 (A_{1g}+B_{1g}) and 640 cm^{-1} (E_g). Shift as well as broadening was observed with Raman bands for AgT, due to the change in electronic environment surrounding TiO_2 and the increased intensity is due to LSPR of Ag NPs.

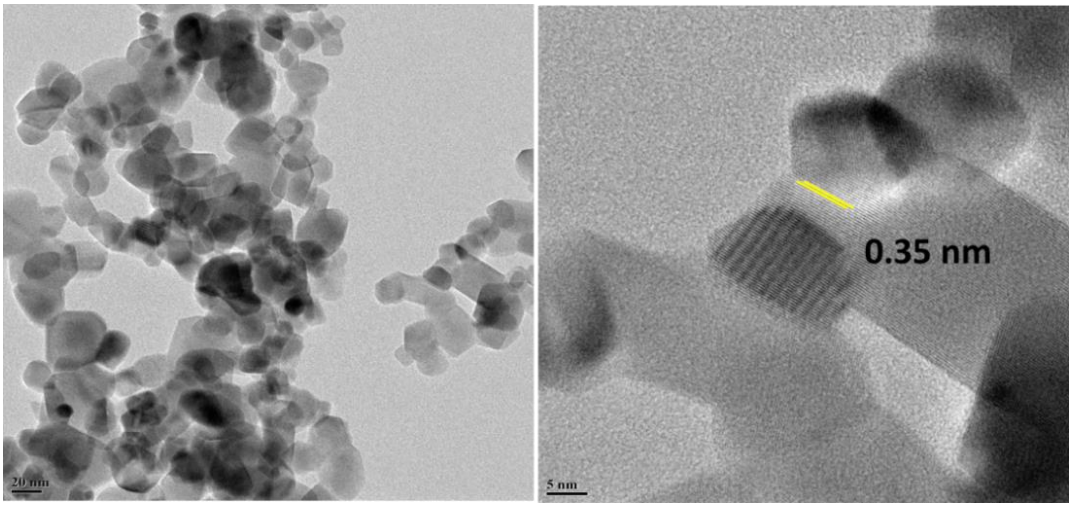

Figure 3.19: TEM and HRTEM image of TiO_2.

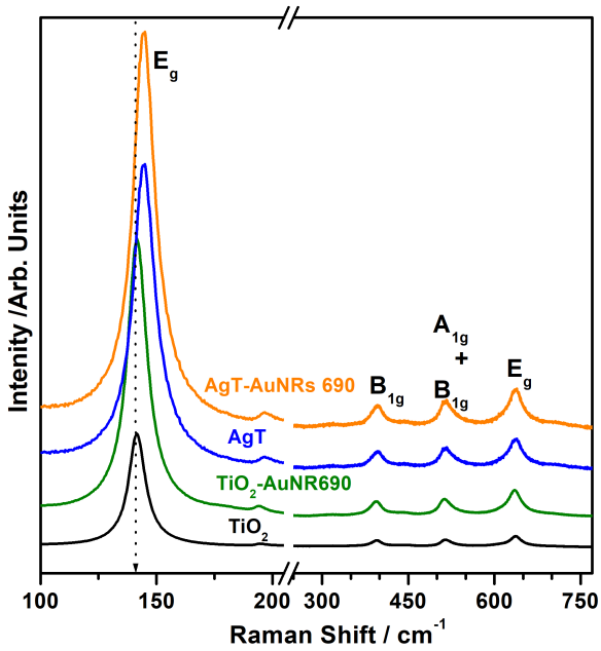

Figure 3.20: Raman spectra of TiO_2, TiO_2-AuNR690, AgT and AgT-AuNR690 composites; latter two show blue shift with increased line broadening after metal deposition.

The same features as that of $AgTiO_2$ was observed after Au NR incorporation in to AgT and the increase in intensity is because of the combined LSPR effect of AgNP and Au NR. As expected, there was no shift observed in TiO_2-AuNR because of the lack of strong electronic interaction between AuNR and TiO_2. However the increased intensity for TiO_2-AuNR as compared to only TiO_2 is attributed to the near field effect of AuNR.

3.6.4 XPS

XPS was employed to explore the electronic state of nanocomposites. As shown in Figure 3.21a, the Ti 2p core level binding energy (BE) appears at 459.4 eV for TiO_2.[21b] However a low BE shift by 1 eV was observed after metal NPs/NR deposition on titania with AgT-AuNR690 and TiO_2-AuNR690. Above shift is attributed to the Fermi level equilibration between TiO_2 and plasmonic metal, and not due to any change in the valence state of titanium. As a result, the electron transfer becomes more favorable between noble metal and TiO_2 conduction band. This result is in good agreement with the Raman spectroscopy results, where frequency shift was observed after silver deposition. Ag 3d core level recorded for AgT-AuNR690 catalyst shows Ag $3d_{5/2}$ core level features at 367.7 eV (Figure 3.21), which indicates the metallic character of Ag.[23]

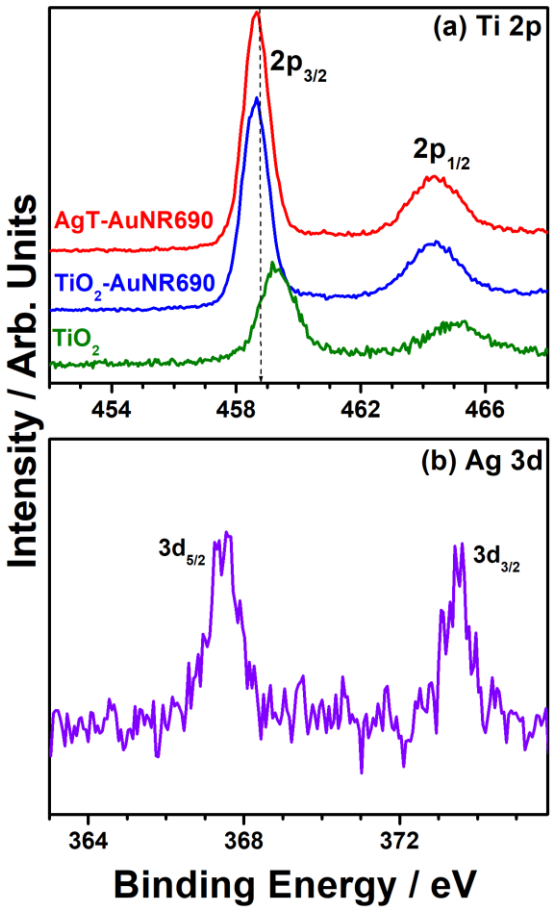

Figure 3.21: XPS results recorded for (a) Ti 2p, and (b) Ag 3d core levels for composites. A shift to lower binding energy was observed with Ti 2p core level, after metal deposition.

3.6.5 Photocatalytic activity

Four different catalysts were prepared by loading AuNR with different aspect ratio on $AgTiO_2$ and surfactant was removed by $HClO_4$ treatment (see sec. 2.2). It is to be re-emphasized that the longitudinal plasmon resonance maximum was different for all the AuNR samples and varied from 600 to 850 nm (Fig. 3.13). The catalysts are denoted as AgT-AuNR645, AgT-AuNR690, AgT-AuNR710, AgT-AuNR770; numbers in the material code corresponds to the longitudinal absorption maximum (at 645, 690, 710, 770 nm) in Fig. 3.13. In all of the materials the amount of Ag content remains the same at 0.85 wt % due to its high photocatalytic H_2 production among the various AgT compositions (Fig 3.22). To identify the longitudinal plasmon contribution to the solar hydrogen generation, the reactions were carried out in one sun conditions as well as with 550 nm cut-off filter ($\lambda \geq 550$ nm) and the results are shown in Figure 3.23 and Table 3.1.

AgT-AuNR690 shows the highest activity of 1097 μmol/h.g under one sun condition with an apparent quantum yield (AQY) 5.12 %. AQY calculation is described in sec. 3.3.3 and and in earlier publications.[33,17b,26,35,38] In contrast, only 448 and 630 μmol/h.g of H_2 was produced from TiO_2-AuNR690 and AgT, respectively, in one sun illumination as shown in Figure 3.23a. In the case of TiO_2-AuNR, the high energy photons (400-500 nm) were not utilized and it results in a decrease in the activity, compared to AgT-AuNR. Since the AuNR is not in direct contact with TiO_2 and no heterojunction is present as evident from the Raman spectroscopy and TEM results, the activity for H_2 evolution under one sun condition is attributed to the near field effect of AuNR. The photocatalytic activity for H_2 evolution for all TiO_2-AuNR composite under one sun condition and $\lambda \geq 550$ nm has been summarized in Table 3.2; no observable hydrogen generation was observed with $\lambda \geq 550$ nm. However in case of AgT-AuNR composite the maximum utilization of visible light photons (both high and the low wavelength region) leads to an improved photocatalytic activity.

To verify the longitudinal plasmon contribution, the reaction was carried out with low energy photons ($\lambda \geq 550$ nm) and the maximum H_2 production of 7 μmol/h.g was achieved with AgT-AuNR690 and AgT-AuNR710 catalyst (Table 2). Under these conditions, we can safely assume that no visible light contribution to SWS arise from the LSPR effect of AuNR along the transverse axis and AgNP. This suggests that only the longitudinal plasmon of AuNR is involved in the photocatalytic H_2 evolution.

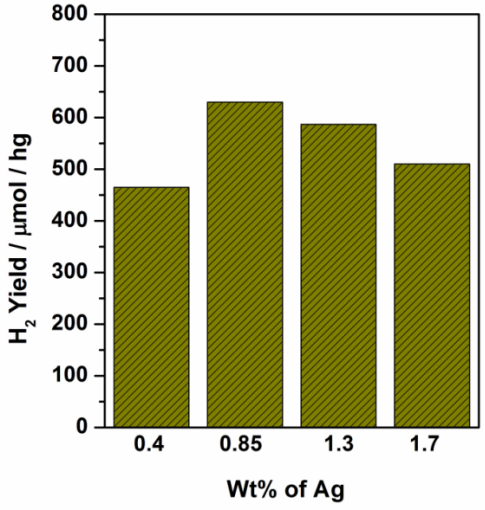

Figure 3.22: Hydrogen yield is shown for different composition of AgT.

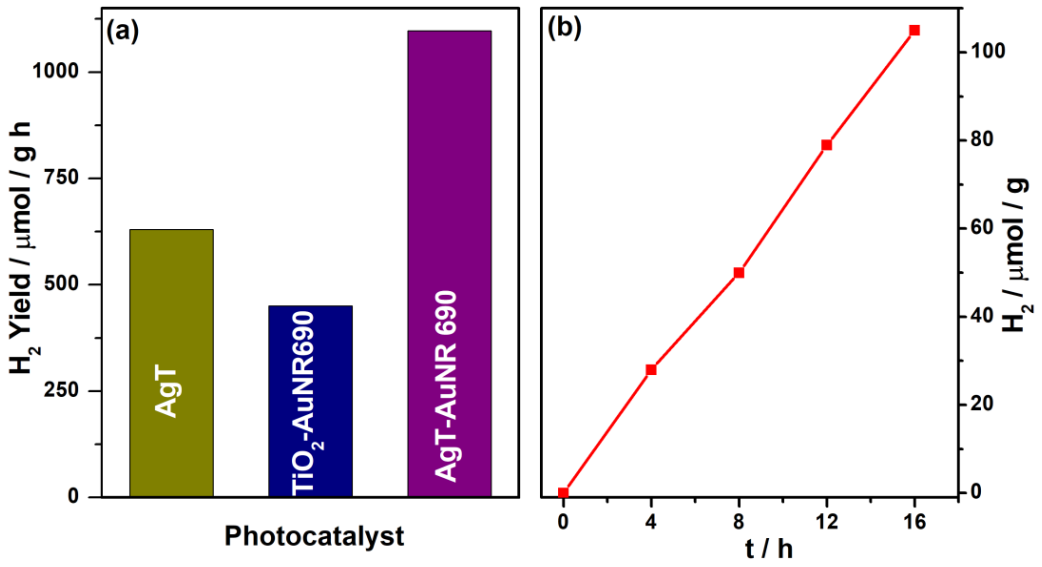

Figure 3.23: (a) Photocatalytic H_2 evolution over AgT, TiO_2-AuNR690 and AgT-AuNR690 catalyst in aqueous methanol solution under one sun illumination, and (b) hydrogen yield as a function of time for AgT-AuNR690 under $\lambda \geq 550$ nm light irradiation.

Table 3.1: Photocatalytic H_2 production over AgT-AuNR catalysts under one sun and $\lambda \geq 550$ nm light irradiation. Apparent quantum yield (AQY) values are given in parenthesis.

Catalyst	H_2 Production μmol/h.g (AQY in %)	
	1 Sun condition (100 mW/cm^2, AM1.5)	$\lambda \geq 550$ nm 60 mW/cm^2
AgT-AuNR645	970 (4.53)	3
AgT-AuNR690	1097 (5.12)	7
AgT-AuNR710	1085 (5.07)	7
AgT-AuNR770	1050 (4.90)	5

$\lambda \geq 550$ nm light was generated with 550 nm cut-off filter supplied from Newport.

The H_2 evolution reaction was carried out with 550 nm cut-off filter for 16 hours and a linear increase in H_2 amount was observed as shown in Figure 3.23b We observed almost the same activity for AgT-AuNR690 and AgT-AuNR710 under one sun and $\lambda \geq 550$ nm light irradiation due to the similar spectral features. Among all catalysts, AgT-AuNR645 exhibited less activity both under one sun and $\lambda \geq 550$ nm light irradiation. This is attributed to the significantly low light absorption in the longitudinal axis due to less asymmetric structure of AuNR645. The enhancement effect decreases for AgT-AuNR770 catalyst, and it is attributed to

the decrease in light intensity of Xe lamp in the near IR region and the low energy associated with them.[39] The same trend in activity was observed in case of TiO_2-AuNR where the light absorption is only due to LSPR of AuNR. However no H_2 evolution was observed under $\lambda \geq 550$ nm light with any TiO_2-AuNR catalysts, (Table 3) due to lack of any Schottky junction between TiO_2 and AuNR. Indeed, electronic integration between Au and TiO_2 makes it as a better catalyst than that of without integration.[17b,26,33,35,36] This result indicates that, a metal-semiconductor junction between plasmonic metal and semiconductor is essential for better utilization of low energy photons in SWS. Even if the near field effect is responsible for changes observed, the extent of transmission of near field effect decrease with increasing distance. Junctions help to increase the transmission of near-field effect to the semiconductors. In case of AgT-AuNR, the AgNP is directly integrated with TiO_2 surface (Fig. 3.16b) and it helps in the transfer of excited electron of the longitudinal plasmon in AuNR to TiO_2. AgNPs acts as a medium to transfer the electrons to TiO_2, generated from $\lambda \geq 550$ nm.

Table 3.2: Photocatalytic H_2 production over TiO_2-AuNR and AgT catalysts under one sun and $\lambda \geq 550$ nm light irradiation.

Catalyst	H_2 Production μmol/h.g	
	1 Sun condition (100 mW, AM1.5)	$\lambda \geq 550$ nm 60 mW
TiO_2-AuNR645	408	0
TiO_2-AuNR690	448	0
TiO_2-AuNR720	445	0
TiO_2-AuNR790	423	0
AgT	630	0
TiO_2	0	0

Hydrogen evolution by AgT-AuNR690 catalyst under one sun illumination as a function of time was measured and the result is shown in Figure 3.24. Experiment was conducted in 5 h cycles, and each cycle was followed by 30 min. degassing and 30 min sonication to remove any dissolved gases, such as O_2, CO_2. After 5 hours of illumination, the catalyst produced 5.5 mMol g^{-1} H_2 and similar activity was maintained for at least next 4 cycles for 20 h of irradiation. This shows the photo stability of the nanocomposite under one sun illumination. It is also to be

underscored that similar Ag+Au combination, but without any specific morphology shows a significantly lower quantity of H_2 generation.[33] 0.25 and 0.14 wt % of Au and Ag, respectively, deposited and integrated with titania (denoted as 40AgAuT) shows a H_2 yield of 0.714 mmol/h.g under one sun conditions. This fact underscores the role of Au NR in the present study can be attributed to the multiplication effect, and not a simple additive effect. A simple comparison of the above H_2 yield to that of the results reported in Figure 3.23 leads to a factor of 1.5. Photocurrent generation also shows an enhancement factor of 2 between the 40AgAuT system reported in sec. 3.2.2and the AgT-AuNR690 (Fig. 3.25).

3.6.6 PEC Measurement

To examine the enhanced SWS activity of the plasmonic photocatalyst under visible light, a set of PEC measurement were carried out in a three electrode system with Ag/AgCl as the references electrode and Pt as the counter electrode. The linear sweep voltammograms (LSV) recorded in 1 M KOH electrolyte solution under one sun illumination is shown in Figure 3.25a.

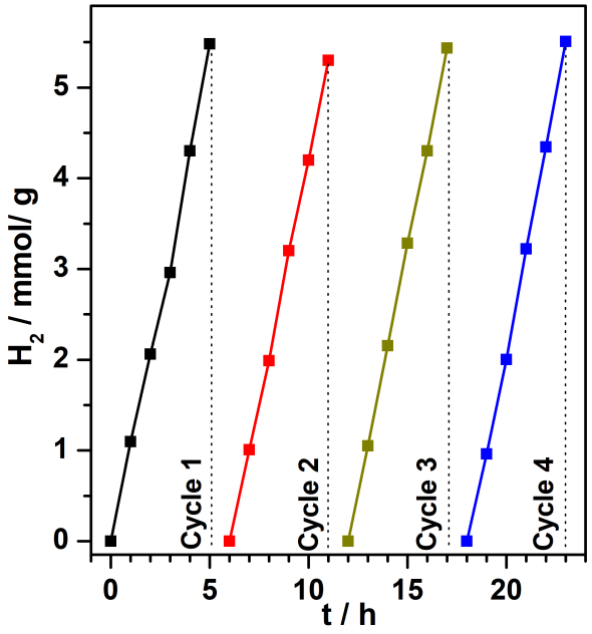

Figure 3.24: H_2 production as a function of time for AgT-AuNR690 under one sun condition.

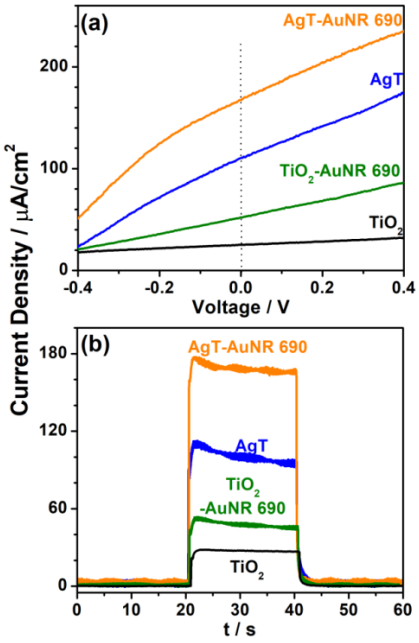

Figure 3.25: (a) Linear sweep voltammogams, and (b) chronoamperometry of TiO_2, AgT, TiO_2-AuNR690 and AgT-AuNR690 electrodes measured in 1 M aqueous KOH solution under one sun condition. Chronoamperometry was also measured at no applied potential and under one sun condition.

A significant enhancement in photocurrent density was observed in AgT-AuNR690 due to the absorption of entire range of visible light range photons. As compared to TiO_2-AuNR690 (50 $\mu A/cm^2$), AgT (90 $\mu A/cm^2$), and AgT-AuNR690 electrodes achieved the enhanced photocurrent density of 175 $\mu A/cm^2$ at no applied potential. The enhanced photocurrent density after AgNPs incorporation shows the effective role of close contact between metal NPs and semiconductor in solar light harvesting application. 40AgAuT reported in sec. 3.2.2 shows a photocurrent of 95 $\mu A/cm^2$ under identical conditions underscoring the multiplier effect of AuNRs from the longitudinal part.

The chronoamperometry curves were measured under one sun illumination and shown in Figure 3.25b. Same current density was observed from the LSV and chronoamperometry study at no applied bias for both TiO_2-AuNR690 and AgT-AuNR690. Zhang et al has reported a photocurrent density of 150 μAcm^{-2} at an applied potential of 1.23 V vs RHE under visible light irradiation.[12] Photocurrent density of 175 $\mu A/cm^2$ observed with AgT-AuNR690 is probably the highest ever reported for any plasmonic $AuTiO_2$ system at zero bias under one sun illumination.

3.7 Mechanism

There are two possible routes to enhance the energy/electron transfer mechanism for a plasmonic-photocatalyst system; one is through plasmon induced resonance energy transfer (PIRET) and the other one is the direct electron transfer (DET) from metal to semiconductor.[8,25a] DET can transfer electrons to the semiconductor when there is a close contact between plasmonic metal and semiconductor. In the present case, even though low energy photons (absorption maximum for Au NR at 650 to 790 nm corresponding to 1.91 to 1.57 eV) were employed, they were sufficient to inject plasmonic state electrons from Au to titania. Indeed this demonstrates that the hot electron transfer from AuNR to TiO_2 is possible as a close contact has been formed at the interface of AgNPs and TiO_2. The mechanism for photocatalytic H_2 generation under $\lambda \geq 550$ nm light irradiation is shown in Figure 3.26a. Hot electrons generated with low energy photons ($\lambda \geq 550$), transfer to TiO_2 through metal-semiconductor Schottky junction formed at the interface of AgNPs and TiO_2.

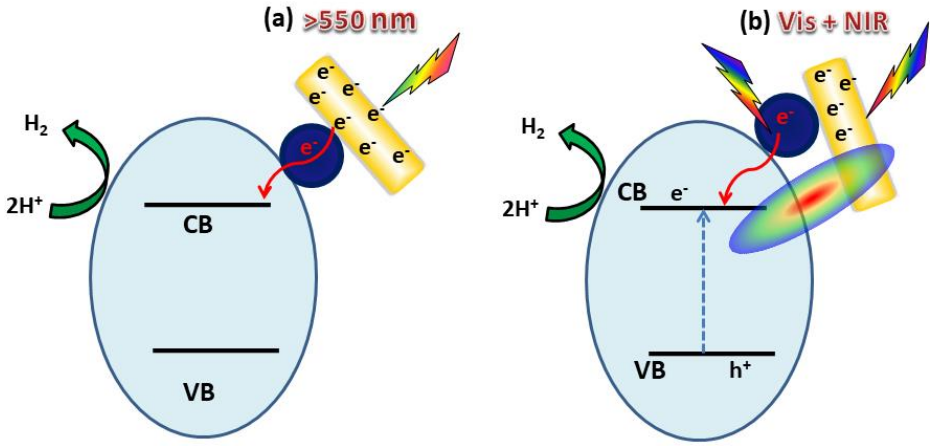

Figure 3.26: Mechanism of photocatalytic H_2 evolution under (a) $\lambda \geq 550$ nm and (b) one sun light irradiation.

Figure 3.26b shows the schematic diagram of the electron transfer process under one sun illumination. Upon visible light irradiation, the AgNPs excited to its surface plasmon state, generating highly energetic hot electrons and injecting them directly in the CB of TiO_2. Although the AuNR is not in direct contact with TiO_2 the PIRET effect can efficiently create electron hole pairs on the nearby TiO_2 nanoparticles. Wherever AuNR is in contact with Ag, DET to TiO_2 CB is also likely to occur. As shown in Figure 3.26a, H_2 evolution take place on TiO_2 CB by utilization of blue, green, and red region of the solar light under one sun condition.

3.8 Conclusion

In summary, an attempt has been made to exploit the entire visible light and limited near IR range photons for solar water splitting. The same has been successfully achieved to a good extent by introducing AgNP and AuNR as plasmonic nano antennas through direct electron transfer and near field effect, respectively. There is significant contribution from the longitudinal plasmon of AuNR to the SWS activity, and it shows a multiplier effect, rather than a simple additive effect. Although the energy harvested exclusively from near IR region is very small, when combined with other high energy green and blue photons under one sun conditions it demonstrates a significantly higher amount of solar light harvesting. Longitudinal absorption of AuNR690 occurs effectively between 580-800 nm; indeed it absorbs both high energy visible and low energy NIR photons with high absorption coefficient. This leads to more hot electrons as well as NIR harvesting simultaneously, and hence the high activity was observed. Whereas, the extent of such synergetic light absorption is less with other size nanorods. As evident from TEM, (111)

facets of AgNPs binds directly to the (101) facets of TiO_2, which facilitate electron transfer in the composite photocatalyst. The design of the electronically integrated plasmonic NPs – semiconductor system gives a new pathway for efficient visible light photocatalyst. An increase in AuNR content in the present system and better electronic integration of AuNR to titania is expected to increase the hydrogen generation from SWS.

Part C: Well Interconnected $AuTiO_2$ an Potential Candidate for High Efficiency Dye Sensitized Solar Cell: Role of Au LSPR on the Efficiency of DSSC

3.9 Introduction

Discovery of Gratzel's solar cell revolutionized the area of DSSC. Mesoporous TiO_2 as photoanode for DSSC was first introduced by Gratzel et al., [45]. After that a lot of efforts has been contributed to improve the light harvesting capacity of photoanode. The limited light absorption by the dye and poor charge separation has been a major hurdle in achieving high efficiency of DSSC.[46,47] Generally the amount of dye absorbed by the photoanode and its spectral features determine the light harvesting efficiency.[48,49] Increasing the thickness of the mesoporous TiO_2 layer leads to improved dye adsorption;[50] however, the diffusion length of the electron also increases simultaneously. As a result, a large fraction of the charge carriers will recombine, rather than improving efficiency of DSSC.[51] Plasmonic metal nanoparticles like silver and gold has been known to improve the light harvesting efficiency of DSSC and water splitting through local surface plasmon (LSP) effect.[13,17,52-55]

Recently, a new approach of involving plasmonic metal nanostructure has received much attention in various fields, like photocatalysis of water splitting,[13,17] plasmonic sensing,[15] SERS [57] and photovoltaic device.[58] Plasmonic nanoparticles have been recognized as a potential candidate to boost the performance of DSSC through LSPs effect.[59-61] The LSPR effect, which refers to the resonance between the electromagnetic field and free-electron oscillation, amplifies the electromagnetic field near the metal nanoparticles,[9] resulting in plasmon enhanced light absorption of photo anode in DSSC. Moreover plasmonic nanostructure morphology can be tuned to possibly absorb the large portion of solar spectrum, especially UV-Vis-NIR. Recently gold nanorod has been used for enhancement of low energy sunlight in DSSC,[62] which exhibited two LSPs peak due to interaction of light along the transverse and longitudinal axis.[38] However most of the previous report based on the physical mixture of metal NPs (Ag or Au), plasmonic core shell nanostructure such as $Au@TiO_2$ and $Au@SiO_2$ incorporated in to photoanode of DSSC, which exhibited enhanced light absorption has also been reported.[61,63] Compared to the above core shell morphology, the metal NPs TiO_2 composite, where they directly connected to

each other, exhibited a stronger localization of plasmonic near field at the metal semiconductor interface, which results in improved light absorption and electron hole pair separation.[5c] The plasmon effect enhances the light harvesting efficiency of dye molecule present within the vicinity of plasmon effect; however, the same decreases as the distance between plasmonic NPs and dye molecule increase. Hupp et al demonstrated by using 36 nm Ag NPs that the effective distance between dye molecule and plasmonic metal NPs is around 5 nm for plasmon enhance photocurrent generation in DSSC.[64] It is well known that the dye adsorption take place only on the TiO_2 surface. Hence it is essential that plasmonic metal NPs should be electronically integrated with TiO_2 (or semiconductor) surfaces, to exploit the full advantage of near field effect. To the best of our knowledge this is the first report, where we used electronically integrated Au-TiO_2 nanocomposite for improved DSSC performance.

In this chapter, we report on electronically integrated Au-TiO_2 nanocomposite with Au particle size of less than 5 nm and 0.042 wt % of Au was prepared by deposition precipitation (DP) method. For comparison purpose, we prepared 2 nm Au NPs using CTAB as the surfactant and $NaBH_4$ as the reducing agent and same amount of Au NPs (0.042 wt %) was mixed with TiO_2 to construct the DSSC photoanode. While the former shows a power conversion efficiency of 7.2 %, the latter shows only 6.4 % and comparable to TiO_2. Different characterization techniques have been employed to investigate the electronic nature of the interface at the Au-TiO_2 heterojunction.

3.10 Results and discussion

3.10.1 UV-Visible spectra

The LSPR effect in $AuTiO_2$ composite was characterized using UV-vis spectroscopy, as shown in Fig. 3.27a. DP method prepared Au-TiO_2 nanocomposites exhibits a plasmon absorption band centered at 550 nm and the absorbance increases with increase in gold content in the composite. As shown in Figure 3.27b, the intensity of absorption as well as the peak broadening occurs after gold deposition. The overlap in the wavelength regime between the LSPR of the Au NPs and the absorption of dyes is one of the key factors for the enhanced performance of DSSCs using Au NPs.[65] The absorption peak for N719 dye in TiO_2 photoanode centered at 520 nm, which has a widest overlapping region with the spectral features of $AuTiO_2$. According to the near field

effect mechanism, the overlapping integral of plasmon resonance and the absorption peak of dye molecule, determine the relative strength of energy transfer.[25a] The relaxation of the LSPR dipole will leads to increase the electron–hole pair separation in the nearby dye molecule resulting in enhanced photocurrent.

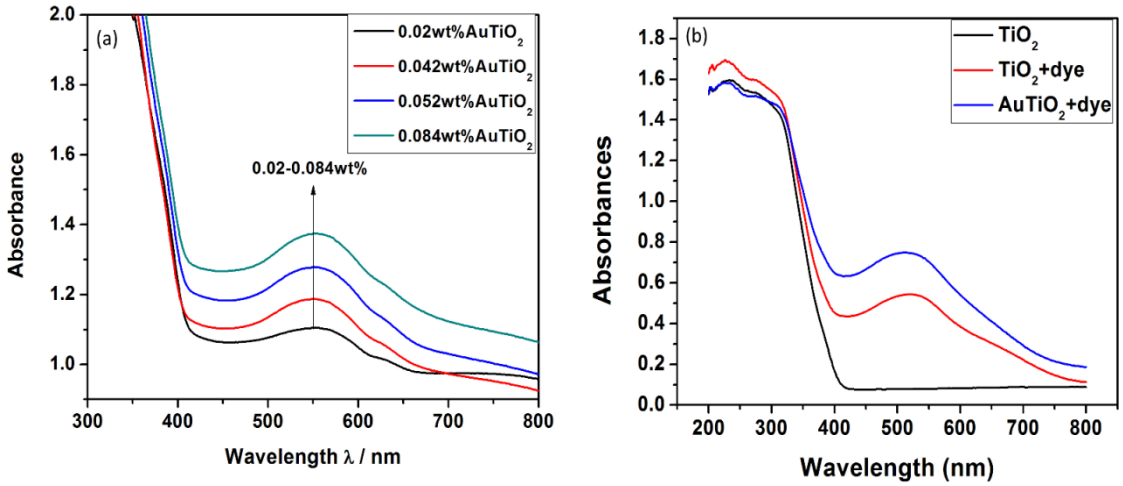

Figure 3.27: UV-Visible absorption spectra of (a) different wt% of $AuTiO_2$, (b) TiO2 and$AuTiO_2$photoanode.

3.10.2 TEM studies

Figure 3.28 shows the HRTEM results recorded for Au-TiO_2 with 0.042 wt % Au. The presence of gold is visible in HRTEM (Figure 3.28a and b). The measured d spacing is 0.24 nm, which corresponds to the (111) facet of metallic Au. The size of the gold particle was found to be between 4-5 nm and many such particles was observed. Au particles seems to deposit preferentially on (110) facet of anatase titania, which is confirmed from the corresponding d-value (0.35 nm). The metal (Au) −semiconductor (TiO_2) (Schottky) junction was observed with $AuTiO_2$; Crystalline nature of the Au and TiO_2 NPs are seen from the different d-spacings of the crystalline lattice. The overlap of lattice fringes clearly indicates the well dispersed nanoscale Schottky junction in the $AuTiO_2$ nanocomposite. More over the Au NPs in the $AuTiO_2$ composite was thermally and structurally stable, as there was no change in crystalline nature, size and morphology even after photoanode preparation. HRTEM images recorded before and after photoanode preparation remains essentially the same.

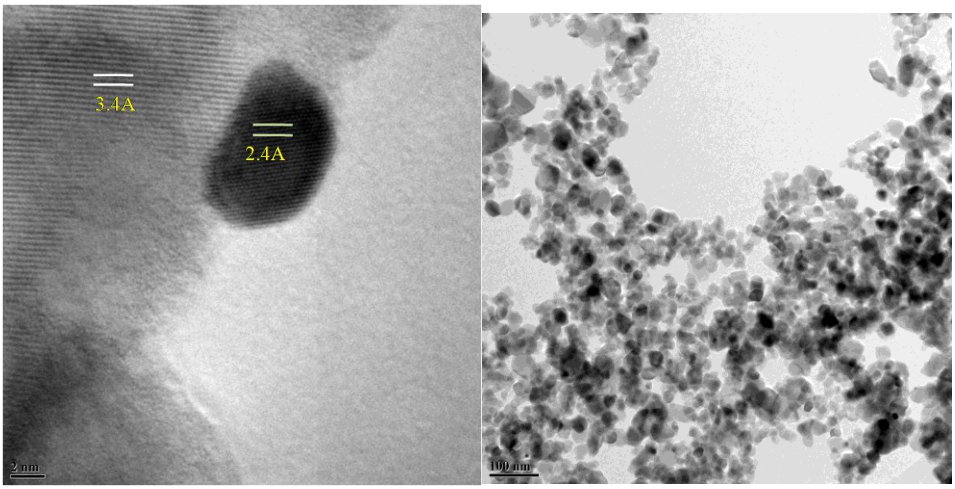

Figure 3.28: HRTEM image of AuTiO2 nanocomposite shows that the Au NPs directly connected to TiO_2surface.

Low weight percent of Au and TiO_2 NPs which is directly connected to the Au NPs provides the support in preventing Au NPs from aggregation. It is worth noting that, due to the proximity and hetero-junction between Au and TiO_2, dye molecule which is attached to the TiO_2 surface would absorb more visible light photon as the Au NPs are also directly connected to the surface.

3.10.3 Raman spectroscopy

The structural features of the composite were studied by Raman spectra as shown in Figure 3.30. All the six Raman active modes observed at 150 (E_g), 198 (E_g), 398 ($B1_g$), 516 ($A1_g$+$B1_g$) and 640 cm^{-1} (E_g) are characteristic features of anatase TiO_2. The crystalline anatase (101) facet exhibits a favorable binding interaction with the Au NPs ,which leads to frequency shift in the Raman spectra.[13] It is very likely that the chemical and electronic environment around the interface of Au and TiO_2 has been changed after Au integration on TiO_2, as a result, shifting as well as peak broadening was observed in the Raman spectra. The increase in intensity of Raman spectra after Au deposition is mainly because of strong local field enhancement around Au NPs. More over in $AuTiO_2$ the peak shifting to higher wave number indicates a possible charge transfer interaction between Au and TiO_2.[59] Any nanocrystalline semiconductor surfaces exhibit many defect sites and particularly oxygen-vacancy sites are associated with electron rich characteristics. These are the sites attracts gold ions in the initial stages of deposition and gold cluster grows at the same site. Very likely, free electrons available at the O-vacancy sites are transferred to Au on deposition and making the interface electronically integrated. Figure 3.29

compare the Raman spectra of TiO_2 and 0.042wt% $AuTiO_2$ prepared by both DP and PM method.

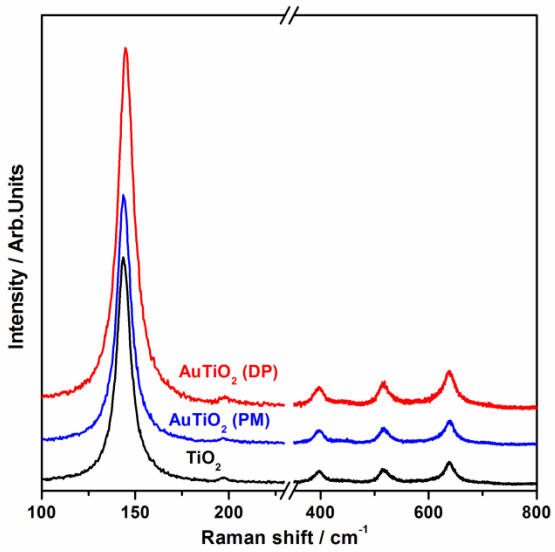

Figure 3.29: Raman spectra of 0.042wt % $AuTiO_2$ prepared by DP and PM.

As compared to $AuTiO_2$ prepared by DP, no shift as well as peak broadening was observed in the PM case in the Raman spectra. More over in the PM, there was very little enhancement in Raman intensity and it is comparable to TiO_2. Above changes in Raman spectrum of PM Au-TiO_2 is attributed to the weak interaction of Au NPs with TiO_2. As a result of weak interaction between Au NPs and TiO_2 the plasmon enhanced absorption of dye decrease because of decaying electromagnetic field. Therefore light harvesting efficiency of plasmonic DSSC using PM is expected to decrease.

3.10.4 DSSC Measurement

To further investigate the role Au LSPR in $AuTiO_2$ prepared by DP, plasmonic DSSCs were fabricated and characterized The complete device fabrication has been given in experimental section 2.3.1. Table 3.3 shows the performance of DSSCs of different compositions. As shown in Table 3.3, compared with efficiency of 5.6% (V_{OC}= 679 mV, J_{sc}= 11.3 mA cm^{-2}, FF= 72) for pure TiO_2, the highest power conversion efficiency of 7.2% (V_{OC}= 686 mV, J_{sc}= 14.1 mA cm^{-2}, FF= 73) has been achieved with 0.042 wt % $AuTiO_2$ photoanode. The table demonstrates that increase in J_{sc} is responsible for enhancement in power conversion efficiency in the presence of Au NPs. The optimum thickness of 12 μm for TiO_2 and 4 μm for

$AuTiO_2$ has been used for the fabrication of photoelectrode. The maximum PEC performance was achieved in device-3 (entry 3), contain 0.042wt% of Au NPs. However, J_{sc} of the devices decrease with further increase in Au loading (0.084 wt% for device 4), which leads to a decline in the PCE. This decrease in performance may be caused by less dye adsorption due to higher gold loading. Since the Au NPs are inlaid on the TiO_2 surface, the surface area of TiO_2 is also expected to decrease to some extent, which would decrease the dye adsorption. The Au NPs can cause intense electromagnetic field enhancement at the $AuTiO_2$ interface, thus increased absorption in the nearby dye molecule. As the Au NPs is directly connected to TiO_2 surface and thus very close to dye molecule, the near field effect is more pronounced. The current density versus voltage characteristics (J–V curves) is shown Fig 3.30. The V_{oc} and FF remain nearly unchanged, while increase in J_{sc} is due to the LSPR enhanced optical absorption in photo anode. As compared to 0.042 wt % $AuTiO_2$ prepared by DP method, a power conversion efficiency of 6.4% (V_{OC}= 703 mV, J_{sc}= 12.8 mA cm^{-2}, FF=71) was realized in PM (entry 6). The size of Au NPs used in PM is around 2-3 nm , which is almost of same size in DP method. The decrease in J_{sc} is a result of weak interaction between Au NPs and TiO_2.

Table-3.3: The performance of DSSC of different composition.

DSSC	**$AuTiO_2$ Ratio**	**J_{sc} (mA cm^{-2})**	**V_{oc} (mV)**	**FF (%)**	**PCE (ɳ%)**
1	0wt%	11.3	679	72	5.6
2	0.02wt%	12.5	698	68	6.0
3	0.042wt%	14.1	686	73	7.2
4	0.052wt%	12.3	687	77	6.4
5	0.084wt%	12.4	693	77	6.7
6 (PM)	0.042wt%	12.8	703	71	6.4

3.10.5 Impedance spectroscopy

Electrochemical impedance spectra (EIS) provide the clear picture of insight operational mechanism. In EIS spectroscopy three semicircles are observed for three different type of process.[48] The resistance elements (1) Rs appears at higher frequency region corresponds to series resistance on counter electrode, (2) R_1 and R_2 represents the charge transfer (CT) resistance

on counter electrode and at the interface of TiO_2/dye/electrolytes, which appears at middle frequency and lower frequency region, respectively. The EIS spectra of TiO_2, 0.042 and 0.084 wt % $AuTiO_2$ are recorded at a bias voltage 0.7 V and the result are shown in Figure 3.31. The measured Nyquist plots are fitted through a transmission line model and inset shows the equivalent circuit. In EIS spectrum Rs of device-1(0 wt % Au), device-3 (0.042wt % Au) and device-5 (0.084 wt % Au) are 8.3, 10.4 and 13.1 Ω, respectively. The diameter of semicircle (R2) represents the CT resistance at TiO_2/dye/electrolyte interface also increase on gold loading. The increase in Rs as well as R_2 is due to incorporation of Au NPS. This resistance has a negative effect on the DSSC performance; therefore an optimum concentration of Au NPs is required to improve the performance of plasmonic DSSC.

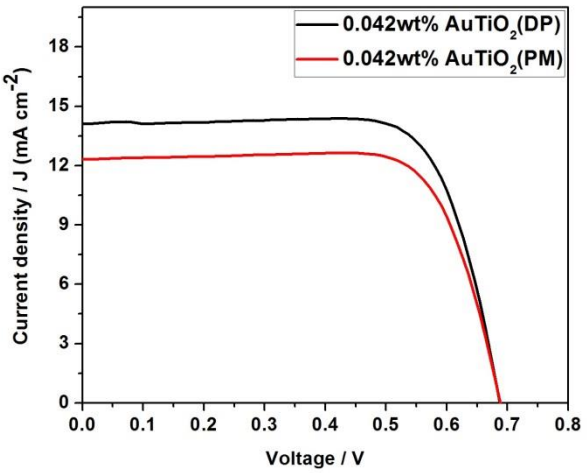

Figure 3.30: The photocurrent density-voltage characteristics (J–V curves) of plasmonic DSCs incorporated with different concentration of Au NPs.

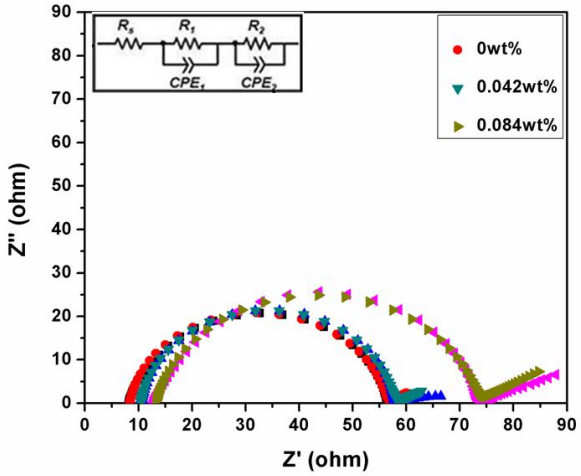

Figure 3.31: Electrochemical impedance spectra of DSSC, incorporated with Au NPs of different concentrations. Inset shows the equivalent circuit.

3.11 Conclusion

In summary electronically integrated $AuTiO_2$ nanocomposite, prepared by DP method, for plasmon enhanced DSSC was proposed and realized. It was demonstrated that plasmon enhanced absorption of dye molecule increase, when Au NPs and TiO_2 are in direct contact with each other as compared to simple physical mixture. As a consequence, for the best DSSC in this study, a PCE of 7.2 % has been achieved with 0.042 wt % $AuTiO_2$, giving an enhancement of 25% in

PCE as compared to only TiO_2. Whereas with same wt% of $AuTiO_2$ prepared by PM exhibits a PCE of only 6.4% . This effect is attributed to the low integration among the constituent components; basically it behaves like a physical mixture. The strong interaction between Au NPs and TiO_2 results in enhanced PCE in plasmonic DSSC.

References:

1. A. Fujishima and K. Honda, *Nature*, **1972**, 238, 37-38.
2. a) A. J. Bard, *Science*, **1980**, 207, 139-144. (b) A. J. Nozik and R. Memming, *J. Phys. Chem.*, **1996**, 100, 13061-13078.
3. S. RajaAmbal, K. Sivaranjani and C. S. Gopinath, *J. Chem. Sci*., **2015**, 127, 33-47.
4. (a) T. Hirakawa and P. V. Kamat, *J. Am. Chem. Soc*., **2005**, 127, 3928–3934. (b) Y. Tian and T. Tatsuma, *J. Am. Chem. Soc*., **2005**, 127, 7632–7637. (c) K. Qian, B. C. Sweeny, A. C. Johnston-Peck, W. Niu, J. O. Graham, J. S. DuChene, J. Qiu, Y.-C. Wang, M. H. Engelhard, D. Su, E. A. Stach and W. D. Wei, *J. Am. Chem. Soc*., **2014**, 136, 9842-9845.
5. (a) Y. Wen, H. Ding and Y. Shan, *Nanoscale.* **2011**, 3, 4411-4417. (b) N. Naseri, *Electrochemica Acta*, **2011**, 56, 1150-1158. (c) Z. W. Seh, S. Liu, M. Low, S.-Y. Zhang, Z. Liu, A. Mlayah and M.-Y. Han, *Adv. Mater.*, **2012**, 24, 2310-2314.
6. T. Sakai and P. Alexandridis, *Chem. Mater.*, **2006**, 18, 2577-2583.
7. K. L. Hardee and A. J. Bard, *J. Electrochem. Soc.*, **1977**, 124, 215-224.
8. S. Linic, P. Christopher and D. B. Ingram, *Nat. Mater*., **2011**, 10, 911-921.
9. K. L. Kelly, E. Coronado, L. L. Zhao and G. C. Schatz, *J. Phys. Chem. B*, **2003**, 107, 668-677.
10. L. M. Liz-Marzan, *Langmuir*, **2006**, 22, 32-41.
11. X. Hong, D. Wang, S. Cai, H. Rong and Y. Li, *J. Am. Chem. Soc.*, **2012**, 134, 18165-18168.
12. Z. Zhang, L. Zhang, M. N. Hedhili, H. Zhang and P. Wang, *Nano Lett.*, **2013**, 13, 14-20.
13. K. Sivaranjani, S. RajaAmbal, T. Das, K. Roy, S. Bhattacharyya and C. S. Gopinath, *ChemCatChem*, **2014**, 6, 522-530.
14. P. Devaraji, N. K. Sathu and C. S. Gopinath, *ACS Catal.*, **2014**, 4, 2844-2853.
15. (a) A. Marimuthu, J. Zhang and S. Linic, *Science*, **2013**, 339, 1590-1593. (b) H. Müller, *Z. Phys. Chem.*, **1996**, 194, 278-279. (c) U. Kreibig, *Appl. Phys. B: Lasers Opt.*, **2008**, 93, 79-89.
16. J. D. Jackson, Classical Electrodynamics, p.220, 3rd Ed., Wiley, 1999.
17. (a) P. A. Bharad, K. Sivaranjani and C. S. Gopinath, *Nanoscale*, **2015**, 7, 11206-11215. (b) A. A. Melvin, K. Illath, T. Das, T. Raja, S. Bhattacharyya and C. S. Gopinath, *Nanoscale*, **2015**, 7, 13477-13488.
18. P. L. Stiles, J. A. Dieringer, N. C. Shah and R. P. Van Duyne, *Annu. Rev. Anal. Chem.*, **2008**, **1**, 601-626.
19. (a) K. Sivaranjani, C. S. Gopinath, *J. Mater, Chem*., 2011, **21**, 2639-2647. (b) A. Fujishima, X. Zhang, D. A. Tryk, *Surf. Sci. Rep*. **2008**, 63, 515 –582.
20. L.-C. Cheng, J.-H. Huang, H. M. Chen, T.-C. Lai, K.-Y. Yang, R.-S. Liu, M. Hsiao, C.-H. Chen, L.-J. Her and D. P. Tsai, *J. Mater. Chem.*, **2012**, 22, 2244-2253.

21. (a) M.Sathish, B.V Viswanathan, R.P .Viswanath, and C.S.Gopinath, *Chem. Mater.* **2005**,17, 6349-6353. (b) M.Sathish, R.P .Viswanath, and C.S. Gopinath, *J. Nanosci. Nanotech.***2009**, 9, 423-432.
22. B. Naik, K. M. Parida, C. S. Gopinath, J. Phys. Chem. C **2010**, 114, 19473-19482.
23. K. Roy, C. P. Vinod, C.S. Gopinath, J. Phys. Chem. C **2013**, 117, 4717-4726.
24. (a) M. Qorbani, et al., *Appl. Catal. B: Environ*., **2015**, 162, 210-216. (b) S. Chen, L.-W. Wang, *Chem. Mater.* **2012**, 24, 3659-3666. (c) Marder, M. P. Condensed Matter Physics, p.633, 2nd Edition, Wiley, 2010.
25. (a) S. K. Cushing, J. Li, F. Meng, T. R. Senty, S. Suri, M. Zhi, M. Li, A. D. Bristow and N. Wu, *J. Am. Chem. Soc.*, **2012**, 134, 15033-15041.(b) X. Ma, Y. Dai, L. Yu and B. Huang, *ACS Appl. Mater. Interfaces*, **2014**, 6, 12388–12394; (c) X. Ma, Y. Dai, L. Yu and B. Huang,*Light: Science & Applications*, **2016**, **5**, e16017.
26. A. A. Melvin, P. A. Bharad, K. Illath, M. P. Lawrence and C. S. Gopinath, *ChemistrySelect*, **2016**, 1, 917-923.
27. M. G. Walter, E. L. Warren, J. R. McKone, S. W. Boettcher, Q.Mi, E. A. Santori, N.S. Lewis, *Chem. Rev*. **2010**, *110*, 6446−6473. (b) S. Y. Moon, E. H. Gwag, J. Y. Park, *Energy Tech.*, **2017** (DOI: 10.1002/ente.201700409)
28. L. K. Preethi, T. Mathews, M. Nand, S. N. Jha, C. S. Gopinath, S. Dash, *Appl. Catal. B: Environ.* **2017**, *218*, 9-19.
29. (a) Y. Lee, C. Chi, S. Liau, *Chem. Mater.*, **2010**, *22*, 922–927. (b) K. M. Parida, N. Biswal, D. P. Das, S. Martha, *Int. J. Hyd. Energy* **2010**, 35, 5262-5269. (c) C. Cheng, S. K. Karuturi, L. Liu, J. Liu, H. Li, L. T. Su, A. L. Y. Tok, H. J. Fan, *Small*, **2012**, *8*, 37-42.
30. G. Cui, W. Wang, M. Ma, J. Xie, X. Shi, N. Deng, J. Xin, B. Tang, *Nano Lett*. **2015**, *15*, 7199−7203.
31. B. W. Deyu Liu, S. Mubeen,T. T Chuong, M. Moskovits, G. D. Stucky, *J. Am. Chem. Soc*., **2016**, *138*, 1114−1117.
32. X-C. Ma, Y. Dai, L. Yu, B-B. Huang, *Light: Science & Applications*, **2016**, *5*, e16017.
33. K. K. Patra, C. S. Gopinath, *ChemCatChem* **2016**, *8*, 3294‑3301.
34. S. RajaAmbal, M. Mapa, C. S. Gopinath, *Dalton Trans*., **2014**, *43*, 12546-12554.
35. P. K. Jain, K. S. Lee, I. H. El-Sayed, M. A. El-Sayed, *J. Phys. Chem. B*, **2006**, *110*, 7238-7248.
36. (a) S. E. Lohse and C. J. Murphy, *Chem. Mater*. **2013**, 25, 1250−1261 (b) X. Huang, S. Neretina, and M. A. El-Sayed, *Adv. Mater*. **2009**, 21, 4880–4910.
37. (a) R. Trevisan, P. Rodenas, V. Gonzalez-Pedro, C. Sima, R. S. Sanchez, E. M. Barea, I. Mora-Sera, F. Fabregat-Santiago, S. Gimenez, *J. Phys. Chem. Lett.***2013**, *4*, 141-146 . (b) K. K. Patra, B. D. Bhuskute, C. S. Gopinath, *Sci. Rep.* **2017**, *7*, 6515.
38. L. Liu, S. Ouyang, J. Ye, *Angew. Chem. Int. Ed.* **2013**, *52*, 6689‑6693.
39. K. C. Ng, W. Cheng, *Nanotech.*, **2012**, *23*, 105602.
40. J. Lee, S. Mubeen, X. Ji, G. D. Stucky, M. Moskovits, *Nano Lett*. **2012**, *12*, 5014−5019.
41. S. Mubeen, J. Lee1, N. Singh, S. Kramer, G. D. Stucky, M. Moskovits, *Nature Nanotech.*, **2013**, *8*, 247-251.
42. K. Park, L. F. Drummy, R. C. Wadams, H. Koerner, D. Nepal, L. Fabris, and R. A. Vaia *Chem. Mater*. **2013**, *25*, 555−563.
43. N. R. Jana, L. Gearheart, and C. J. Murphy, *Adv. Mater*. **2001**, *13*, 1389-1393.
44. S. Link and M. A. El-Sayed, *J. Phys. Chem. B*, **2005**, *109*, 10531-10532.
45. B. O. Regan and M. Grätzel, *Nature*, 1991, **353**, 737-740.

46. S. Ito, P. Liska, P. Comte, R. Charvet, P. Pechy, U. Bach, L. Schmidt-Mende, S. M. Zakeeruddin, A. Kay, M. K. Nazeeruddin and M. Grätzel, *Chem. Commun.* , **2005**, 34, 4351-4353
47. F. Huang, D. Chen, X. L. Zhang, R. A. Caruso and Y.-B. Cheng, *Adv. Funct. Mater.*, 2010, **20**, 1301-1305.
48. J.-Y. Liao, B.-X. Lei, D.-B. Kuang and C.-Y. Su, *Energy Environ. Sci.*, 2011, **4**, 4079-4085.
49. X. Wu, G. Q. Lu and L. Wang, *Energy Environ. Sci.*, 2011, **4**, 3565-3572.
50. S. Ito, P. Chen, P. Comte, M. K. Nazeeruddin, P. Liska, P. Pechy and M. Grätzel, *Prog. Photovoltaics*, 2007, **15**, 603-612.
51. A. Hagfeldt, G. Boschloo, L. Sun, L. Kloo and H. Pettersson, *Chem. Rev.*, 2010, **110**, 6595-6663.
52. W. L. Barnes, A. Dereux and T. W. Ebbesen, *Nature (London, U. K.)*, 2003, **424**, 824-830.
53. H. A. Atwater and A. Polman, *Nat. Mater.*, 2010, **9**, 205-213.
54. J. A. Schuller, E. S. Barnard, W. Cai, Y. C. Jun, J. S. White and M. L. Brongersma, *Nat. Mater.*, 2010, **9**, 368.
55. M. A. Green and S. Pillai, *Nat. Photonics*, 2012, **6**, 130-132.
56. P. K. Jain, X. Huang, I. H. El-Sayed and M. A. El-Sayed, *Acc. Chem. Res.*, 2008, **41**, 1578-1586.
57. K. Kneipp, Y. Wang, H. Kneipp, L. T. Perelman, I. Itzkan, R. R. Dasari and M. S. Feld, *Phys. Rev. Lett.*, 1997, **78**, 1667-1670.
58. A. P. Kulkarni, K. M. Noone, K. Munechika, S. R. Guyer and D. S. Ginger, *Nano Lett.*, 2010, **10**, 1501-1505.
59. Y. Li, H. Wang, Q. Feng, G. Zhou and Z.-S. Wang, *Energy Environ. Sci.*, 2013, **6**, 2156-2165.
60. Q. Xu, F. Liu, Y. Liu, K. Cui, X. Feng, W. Zhang and Y. Huang, *Sci Rep*, 2013, **3**, 2112.
61. J. Qi, X. Dang, P. T. Hammond and A. M. Belcher, *ACS Nano*, 2011, **5**, 7108-7116.
62. S. Chang, Q. Li, X. Xiao, K. Y. Wong and T. Chen, *Energy Environ. Sci.*, 2012, **5**, 9444-9448.
63. H. Choi, W. T. Chen and P. V. Kamat, *ACS Nano*, 2012, **6**, 4418-4427.
64. S. D. Standridge, G. C. Schatz and J. T. Hupp, *J. Am. Chem. Soc.*, 2009, **131**, 8407-8409.
65. Q. Wang, T. Butburee, X. Wu, H. Chen, G. Liu and L. Wang, *J. Mater. Chem. A*, 2013, **1**, 13524-13531.

4A: Possibly Scalable Solar Hydrogen Generation with Quasi-Artificial Leaf Approach.

4B: Quasi Artificial Leaf for Solar Hydrogen Generation with Earth Abundant Co-Catalyst.

4C: Photocatalytic and Cocatalytic Behavior of MoS_2-mild oxidized Graphite (MoS_2-mGO) Nanocomposite on a TiO_2/PbS/CdS Quasi Artificial Leaf for Solar Hydrogen Production: Dual Role of MoS_2-mGO.

Part A: Possibly scalable solar hydrogen generation with quasi-artificial leaf approach

4.1 Introduction

Like Steve Jobs, it may be essential to know `how to connect the seemingly (un)related dots ?` that could lead to a possible solution to the complex scientific problems. SWS is one such "Holy Grail" problem, as described by Alan Bard et al.,[1] which needs to network such seemingly (un)related dots. The conversion of solar energy into chemical energy through solar hydrogen production by artificial photosynthesis[2-3] is a highly promising approach, but an equally complex problem.[4] In this context, semiconductor oxide materials are the inevitable components for photocatalytic hydrogen generation. The efficiency of hydrogen production depends on the extent of light absorption, charge separation, charge migration, charge utilization at redox sites, and integrating all these factors in an efficient way.[5,6] The optimization of all processes in a single photocatalyst that works in solar light with high activity, scalability, and sustainability has not been reported yet.[6,7] Also the choice of the workable photocatalyst is limited to a few wide band gap semiconductors, like TiO_2, which absorb in the ultraviolet (UV) region of the solar spectrum, and limiting the overall efficiency. Hence it is crucial to integrate (or network) the various components of light harvesting in an efficient manner towards higher efficiency.

As predicted by Alivisatos on 1996,[8] quantum dots (QDs) with tunable band gaps are currently employed for light emitting applications. Though QD is considered as a potential candidate for the light harvesting applications, such as SWS, it is yet to be established with high efficiency. Sensitization of a wide band gap semiconductor by a narrow band gap QD has been developed as a potential method for hydrogen generation[9] due to light absorption in a broad wavelength (visible and near infrared) range. QDs are mostly used as a sensitizer due to large light absorption cross section, and shape and size dependent optical properties. Another way to improve the light absorption capacity of wide band gap semiconductor is to use plasmonic metal nanostructure, such as nanogold.[10] Such plasmonic metal nanostructure has been used to improve the efficiency of dye-sensitized solar cell (DSSC) and SWS.[11-12] The enhancement in efficiency is due to the localized surface plasmon resonance (LSPR) of the metal nanoparticles (NPs). The frequency of LSPR oscillation depends on the shape and size of the metal nanostructure and dielectric constant of the surrounding medium.[13,14] The oscillating electric field enhance the

photocurrent generation in photoanodes by transferring its energy to the surrounding molecules or lattice. It is well known that the energy transfer from metal to semiconductor occurs by plasmon induced resonance energy transfer (PIRET) process.[13-15] PIRET occurs through a non-radiative energy transfer process from the dipole of the plasmonic metal NP to the dipole of the excited semiconductor in a limited area; hence it is critical that semiconductors must be in the immediate vicinity of plasmonic metal NP. It would be an added advantage if energy transfer from plasmon state can be utilized.

To take advantage of the above PIRET enhancement mechanism, we prepared a composite, in which the AuNPs are in physical proximity with titania as well as chalcogenides QDs for better solar light harvesting. QDs that are placed spatially very close to the AuNPs enhance the localized electric field surrounding the AuNPs and hence an increase in the photocurrent and solar hydrogen was observed by generating more electron-hole pairs in QDs. For this purpose, $AuTiO_2$ nanocomposite was employed, where the plasmonic AuNPs are electronically integrated to the porous TiO_2 surface, and further sensitized by PbS and CdS QDs.[15,16] By using this concept, a wireless photochemical cell or quasi-artificial leaf (QuAL) was prepared to generate hydrogen without applying any potential. The success of this approach possibly would help to design better light harvesting synthetic architectures to produce solar fuels.

4.2 Results and Discussion

4.2.1 Structural and Spectral characterization

AuNPs (~5 nm) was electronically integrated with TiO_2 by following deposition-precipitation method.[17] The crystallographic facets of TiO_2 remain unchanged before and after gold deposition, which is evident from the XRD results (Fig. 4.1). No features due to gold were discernible indicating the possibility of fine distribution of gold clusters on titania support. Au loading on titania was varied between 0.02 and 0.084 wt% to explore the optimum amount of gold required for activity optimization. 0.052 wt % Au containing $AuTiO_2$ gives the maximum H_2 yield (1.05 mMol/h.g) with methanol as sacrificial agent (Fig. 4.2), and hence this particular composite was used for the photoanode fabrication. PbS QDs was deposited on $AuTiO_2$ electrode followed by CdS QDs by successive ionic layer adsorption and reaction (SILAR) technique.[16] By its very nature, SILAR method allows the physical proximity of chalcogenide

QDs around Au nanoparticles. ZnS layer deposited finally on CdS QDs for providing stability to the photoanode, and it protects from photocorrosion. Detailed procedure for $AuTiO_2$, photoanode fabrication, solar hydrogen production and various PEC measurements (experimental section 2.5) is given experimental section 2.3 (Chap. 2). Various control photoanodes were also fabricated and evaluated.

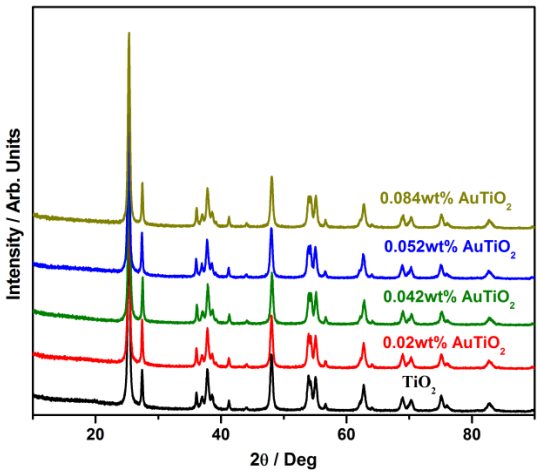

Figure 4.1: Powder XRD patterns shows, the TiO_2 and Au/TiO_2 samples with different weight percent of gold. No Au peak was observed in XRD patterns of Au/TiO_2 due to small amount gold well-dispersed on the TiO_2 surface.

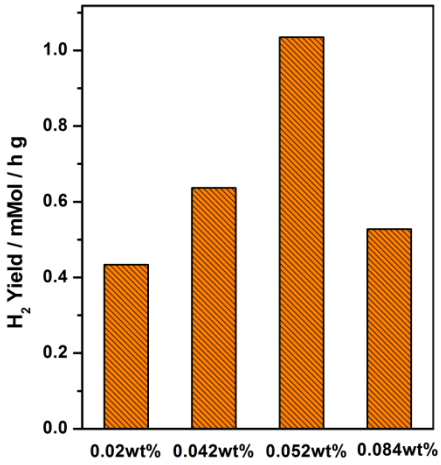

Figure 4.2: SWS activity was measured with $AuTiO_2$ powder with different Au-content. The SWS was carried out by using 20 mg catalyst, 30 ml water and 10 ml methanol in a 50 ml quartz RB under one sun condition. The maximum activity of 1.05 mMol/g/h of H_2 was observed with 0.052 wt % of Au and the same wt % were used for the device fabrication.

Electronic integration of AuNPs to the TiO_2 surface is fully supported by Schottky junction from the representative HRTEM (Fig. 4.3a and b) and Raman spectroscopy (Fig. 4.3c) studies. HRTEM image shows the majority of lattice fringes corresponds to (101) crystallographic planes of anatase phase titania (d_{101} = 0.35 nm) (Fig. 4.3a). Fig. 4.3b shows HRTEM image centered around a single gold nanoparticle surrounded by several titania particles. Uniform d = 0.24 nm value observed throughout the Au nanoparticle suggests the growth was along (111) facet. Au particle size varied in 6-8 nm range. As shown in Figures 4.3b the metal-semiconductor heterojunction was observed with all composites, where the (111) facet of metal is in direct contact with (101) facets of several particles of anatase TiO_2. It is known that heterojunction is an essential feature for separation of electron-hole pairs at the metal-semiconductor interface.[5,14] Another advantage of Au-TiO_2 heterojunction is the generation of

additional charge carriers through PIRET process, which is expected to enhance photocurrent and hydrogen generation.

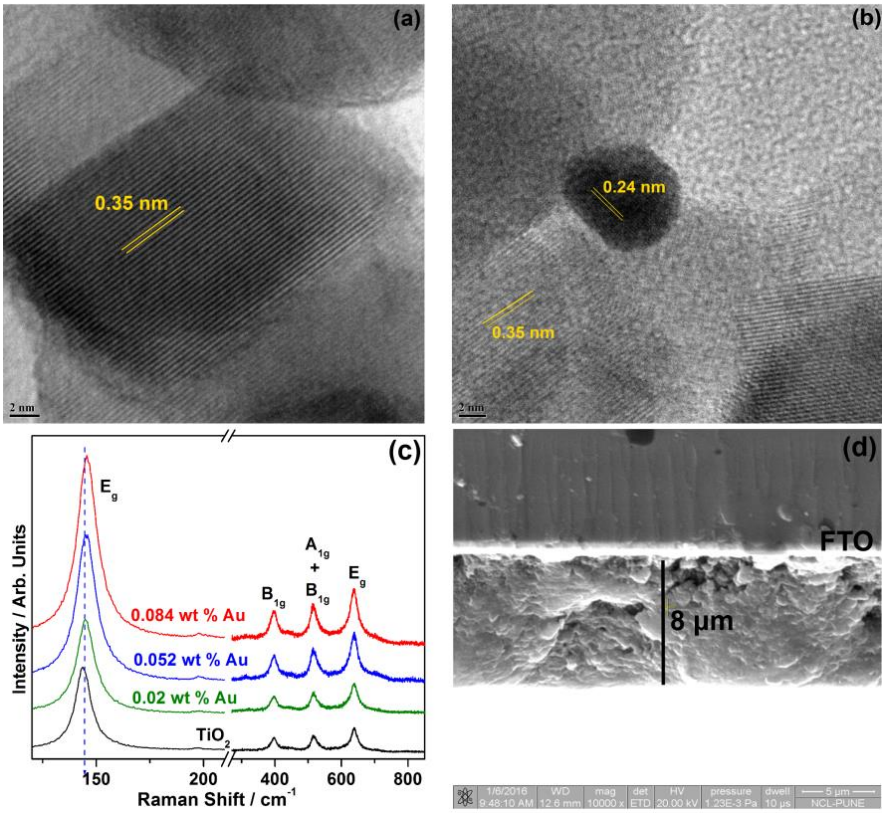

Figure 4.3. (a and b) HRTEM image of the $AuTiO_2$ exhibiting the heterojunction between Au and TiO_2. TiO_2 particle exposes (101) facets predominantly. Scale bar in both images is 2 nm. (c) Raman spectra of pure TiO_2 and Au-TiO_2. Enhancement in the intensity of titania features and shift in E_g mode suggests the active role of PIRET process. (d) Representative image of freshly cleaved 8 µm thick surface of $AuTiO_2$/PbS/CdS electrode recorded by SEM. The bright thick white line is due to FTO, coated on glass.

Raman active modes of anatase (145 (E_g), 198 (E_g), 398 (B_{1g}), 516 (A_{1g}+B_{1g}) and 640 cm^{-1} (E_g)) and rutile (420-460 (E_g) and 610 (A_{1g})) are observed in Fig. 4.3c; however, the frequency shift in the Raman spectra is attributed to the favorable binding interaction, particularly between (101) facet of anatase titania with the AuNPs. The electronic environment at the Au and TiO_2 interface has been modified after Au integration, as a result of strong enhancement in intensity was observed for all anatase features in the Raman spectra. The increased intensity in Raman spectra after Au deposition is attributed to PIRET process resulting in a strong electronic interaction between Au and TiO_2 which induces electron-hole pair separation in QDs efficiently.

The total thickness of the photoanode is ~8 µm, which is evident from the SEM analysis of *in situ* cleaved surface (Fig. 4.3d). Thickness varies in a narrow range of 8±0.5 µm. It is to be particularly noted that no separate layers for deposited components were observed, rather a smooth layer above FTO layer was observed. This uniform layer is in contrast to the separate layers found for different components in the earlier literature report.[16] We attribute this to the porous network of titania, which allows diffusion of Cd^{2+}, S^{2-} and Pb^{2+} ions and hence the formation of CdS and PbS in the neighborhood of Au and TiO_2 in Au-TiO_2. Chemical mapping of Au, Cd, Ti, S, and Pb was measured on a freshly cleaved AuTiO_2/PbS/CdS photoanode by FESEM-EDX, and the results are shown in Fig. 4.4. Throughout the cleaved photoanode film surface, all of the constituent elements can be seen; this fully supports the diffusion of Cd^{2+}, S^{2-} and Pb^{2+} ions and chalcogenide formation occur in the pores of Au-TiO_2. Relatively dense sulfur distribution from PbS and CdS ensures the Au is inevitably in their neighborhood. Uniform distribution fully asserts the physical proximity of Au and chalcogenide particles in the porous titania. Further, the physical proximity of various components in the confined pores suggests the formation of the abundant bulk heterostructure, which is expected to enhance solar light to current conversion efficiency.

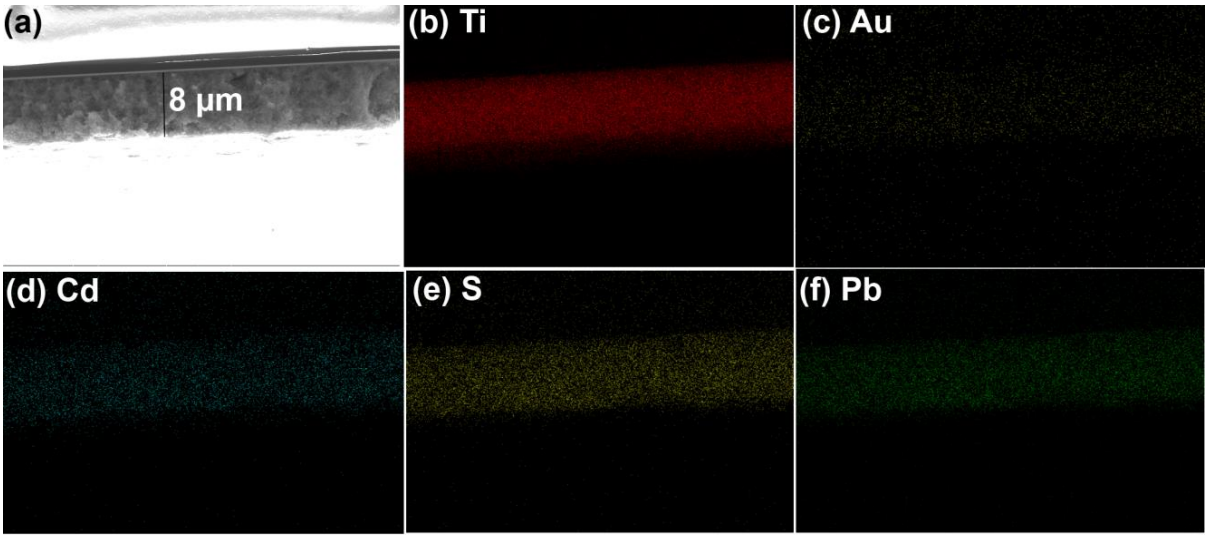

Figure 4.4: FESEM-EDX chemical mapping analysis carried out to show the uniform distribution of chalcogenides, and Au on TiO_2 in AuTiO_2/PbS/CdS photoanodes. Due to small amount of gold, faint yellow color can be seen throughout the film.

Further support was obtained from the textural analysis of TiO_2 and Au-TiO_2, by low magnification TEM and porosity measurements by adsorption isotherms and the results are

shown in Fig. 4.5. Mesoporous nature (type IV isotherm with H1 hysteresis) is clearly evident from the adsorption isotherm as well as TEM analysis. A marginal reduction in surface area and pore-size was observed from titania to $AuTiO_2$ while maintaining the average pore size to be 8 nm.

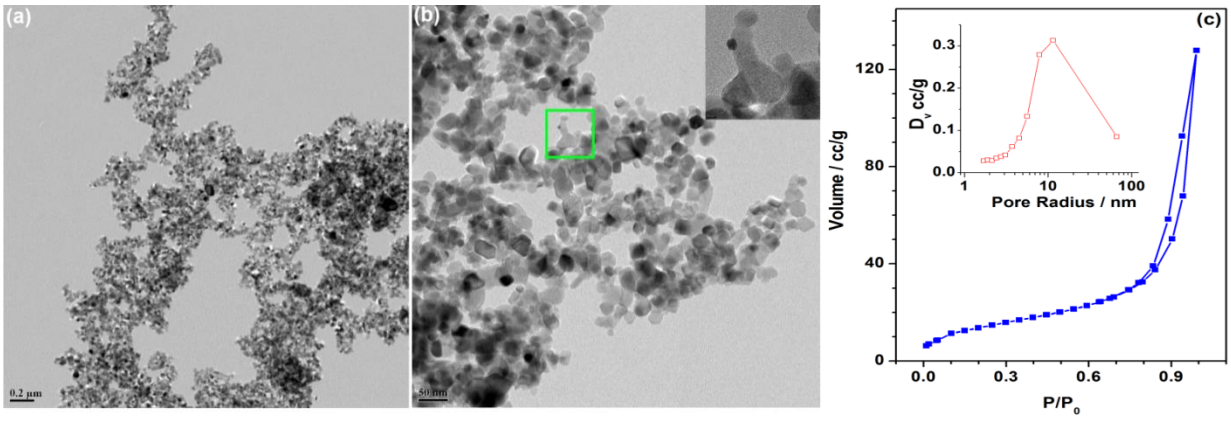

Figure 4.5: (a-b) Low resolution TEM images shown to support the porosity of the (a) titania, and (b) Au-TiO_2 employed in the present studies. Green square area (inset in b) was imaged separately to show the Au deposited on titania particle. (c) Adsorption-desorption isotherm (type IV with H1 hysteresis loop) and pore-size distribution measured at 77 K for titania fully demonstrates its mesoporous nature with majority of pore sizes between 4-12 nm. Au-TiO_2 also shows very similar pattern. Surface area for titania is 59 m^2/g, while that of Au-TiO_2 is 55 m^2/g. Average pore diameter was observed at 8 nm in both cases. However, a minor pore volume reduction occurs from 0.24 cc/g to 0.23 cc/g, without and with gold, respectively.

4.2.2 UV-Visible spectroscopy

Figure 4.6 shows the UV-Visible absorption spectra of various photoanodes prepared with TiO_2 and $AuTiO_2$. Pure $AuTiO_2$ shows an absorption band at 550 nm corresponding to the LSPR of the AuNPs. A broad absorption band centered at 450 nm corresponds to the CdS QD. LSPR peak of Au NPs was observed to be shifted as well as broadened to high λ regime in chalcogenide containing photoanode compared to $AuTiO_2$; this is likely due to the change in the dielectric constant of the surrounding environment.[15,18] In fact, light absorption up to ~700 nm was observed directly supports the electronic interaction of chalcogenide layers with nano-Au. $AuTiO_2$/PbS and $AuTiO_2$/CdS films prepared separately shows a systematic shift and broadening of Au-LSPR absorption to higher λ reiterates the influence of electronic interaction of PbS or CdS with Au in $AuTiO_2$. TiO_2 being a mesoporous substrate with a surface area of 59 m^2/g, dispersion of chalcogenide QDs into titania is expected, which increases the interaction among

them. Inset in Fig. 4.6 displays a digital photograph to show the changes in the colour of the photoanodes, from (1) purple for Au-TiO_2, (2) yellow for TiO_2/PbS/CdS to (3) greenish-yellow for $AuTiO_2$/PbS/CdS.

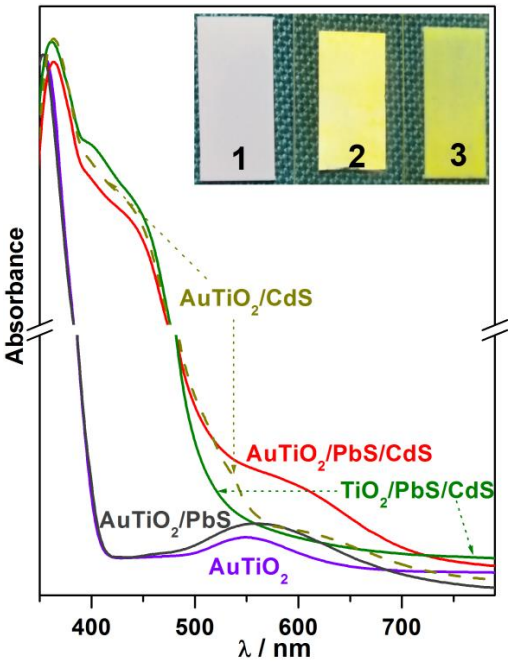

Figure 4.6. UV-Vis absorption spectra of the $AuTiO_2$, $AuTiO_2$/PbS, $AuTiO_2$/CdS, TiO_2/PbS/CdS, and $AuTiO_2$/PbS/CdS photoanodes. Note the shift in absorption onset from $AuTiO_2$ at 560 nm to about 700 nm for $AuTiO_2$/PbS/CdS. The inset shows a digital photograph of the colors associated with photoanode films, (1) $AuTiO_2$ and (2) TiO_2/PbS/CdS, and (3) $AuTiO_2$/PbS/CdS.

4.2.3. Photocatalytic H_2 evolution from QuAL device

8 µm thick wireless photochemical cells were constructed with Au-TiO_2 (Au-TiO_2/PbS/CdS) or TiO_2 (TiO_2/PbS/CdS), and evaluated for solar hydrogen production. The total area of the photoactive material over FTO plate is 10×10 mm^2. Pt was deposited as a strip (4x10 mm^2) on the other half of the FTO plate, and it acts as a co-catalyst which provides the active sites for H_2 evolution. The overall photochemical cell was immersed in the electrolyte (Na_2S/Na_2SO_3) solution and illuminated under one sun condition (AM 1.5 filter, 100 mW/cm^2) from the front side of the FTO plate. The weight of the photoanode material was carefully measured, and used to calculate the normalized photoactivity per gram with an assumption that the activity increased linearly. Fig. 4.7a shows the H_2 evolution rate (HER) by the wireless photochemical cells. The $AuTiO_2$/PbS/ CdS wireless photochemical cell exhibited highly

enhanced H_2 evolution rate (HER) at 490±25 µmol/h and a PCE of 5.6 %. Above HER value corresponds to 12±0.5 ml/h H_2 with 1 cm^2 cell. A movie recorded under the measurement conditions (A movie recorded (Movie1.avi) is shown in the attached CD) demonstrates the instant evolution of H_2 bubbles predominantly from the Pt and Pt-photoactive material interface. Inverted gas burette was employed to collect H_2 gas for quantification. Assuming a linear increase in HER with large area photoanodes, it is expected to provide about 6 L H_2 for a gram of photoanode material coated over about 23x23 cm^2. Even if there is a 50 % (67 %) decrease in HER at bigger size photoanodes (which is expected as in DSSC), it would still lead to 3 L (2 L) H_2 $h^{-1}.g^{-1}$. It is to be underscored that the hydrogen yield expected after efficiency reduction considerations is still very significant and worth pursuing further. Nonetheless, higher area photoanodes needs to be systematically fabricated and evaluated, and we will address these issues in one of the future manuscripts. In the same manner solar hydrogen generation activity of TiO_2/PbS/CdS was measured, and the result shows a significantly lower HER (0.3 mMol/h;

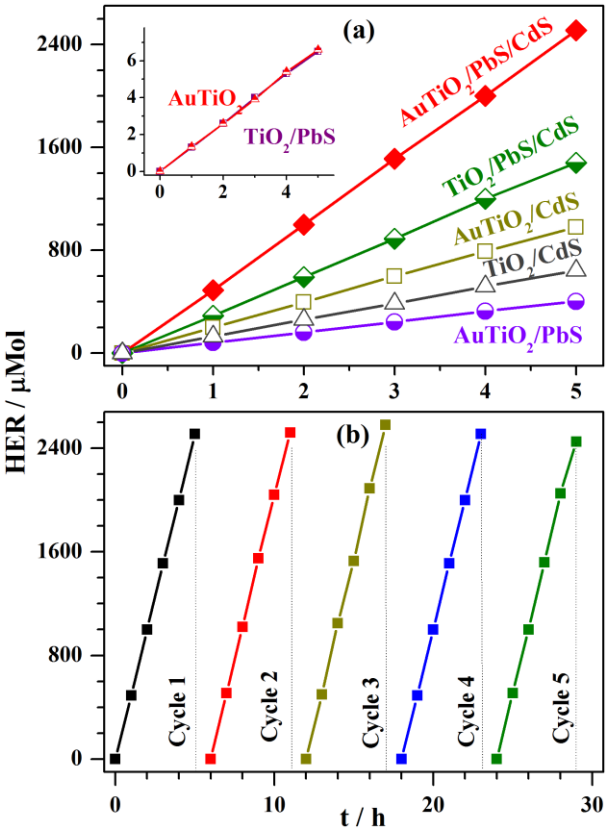

Figure 4.7: (a) Photocatalytic H_2 evolution rate of wireless devices is shown under one sun illumination. Photochemical cell was immersed in the electrolyte (Na_2S/Na_2SO_3) solution. (b) Photostability of the $AuTiO_2$/PbS/CdS wireless device is demonstrated by performing the experiment for five cycles.

7.4±0.4 ml/h from 1 cm^2 cell). Similar work reported by Trevisan et al.[16] shows only 0.18 ml/h H_2 from 1 cm^2 TiO_2/PbS/CdS cell, indicating the efficacy of the present preparation method with optimized parameters.

Various control photoanodes prepared were also evaluated for HER, and the results are given in Fig. 4.7a. While TiO_2/PbS and $AuTiO_2$ shows a negligible HER (1.5 μmol/h; Fig. 4.7a inset), PbS on $AuTiO_2$ demonstrating a quantum jump in HER (80±5 μmol/h) underscores the role of PIRET process. Similarly, CdS on $AuTiO_2$ also shows higher HER (200±10 μmol/h) than on TiO_2 (125±10 μmol/h) again underscores the role of Au LSPR.

The stability of the wireless $AuTiO_2$/PbS/CdS device was studied and the HER evaluated is shown in Figure 4.7b. The device was continuously irradiated for 25 h, with about 1 h break after every five hours to replenish with the fresh sacrificial agent solution. Same activity was maintained in all cycles indicating that the photochemical cell is intact and devoid of any photocorrosion. Indeed, this is important observation indicating the sustainability or stability of the device, given the presence of chalcogenide in the photochemical cell.

4.2.4. Photoelectrochemical measurement

The PEC performance of the photoanodes was studied in a three-way electrode system with Ag/AgCl as the reference electrode and Pt as the counter electrode, and the results are shown in Fig. 4.8a and b. All PEC studies are measured in an aqueous Na_2S/Na_2SO_3 solution. The $AuTiO_2$/PbS/CdS working electrode exhibited 4.3 mA/cm^2 photocurrent at zero applied voltage (vs Ag/AgCl) and one sun illumination (AM1.5 filter, 100mW/cm^2). The onset potential, derived from the J-V curves, was -1.19 V and -1.26 V for TiO_2/PbS/CdS and $AuTiO_2$/PbS/CdS (vs Ag/AgCl), respectively. 70 mV negative shift is expected to enhance the H_2 evolution due to Fermi level (E_F) equilibration[14,19] between AuNPs and semiconductors. E_F equilibration occurs since the QDs are distributed throughout the $AuTiO_2$ matrix, and hence the Au-TiO_2 is in direct contact with the liquid electrolyte. The negative shift in the onset potential of $AuTiO_2$/PbS/CdS also indicates a better charge separation, and it improves the PEC performance.

An immediate photo response of the photoanode was studied by chronoamperometry at no applied voltage, and the results are shown in Figure 4.8b. As compared to TiO_2/PbS/CdS (2.7 mA/cm^2), $AuTiO_2$/PbS/CdS exhibits high photocurrent density of 4.3 mA/cm^2. An increase in

photocurrent generation with latter photoanode by 160 % than that of the former highlights the efficient light harvesting by a combination of $AuTiO_2$ as well as chalcogenide QDs. The increase in the current is attributed to the PIRET process, which in turn increase the generation of charge carriers. It is also to be noted that HER increases linearly with photocurrent generated in both photoanodes underscoring the charge utilization are to a similar extent.

The performance of the PEC cell was studied in both wired, and wireless configurations to produce H_2, but at no applied potential under one sun illumination (Fig. 4.8c and d). In the wired configuration either of the photoanode was connected to the Pt as the counter electrode. Under illumination, photocurrent flows from the working electrode to Pt to produce H_2. Fig. 4.8c shows the chronoamperometry result measured for 1 hour.

Solar hydrogen was measured, as in Fig. 4.7, but with the above two electrode configuration at no applied potential. Amount of H_2 evolved was measured with GC periodically

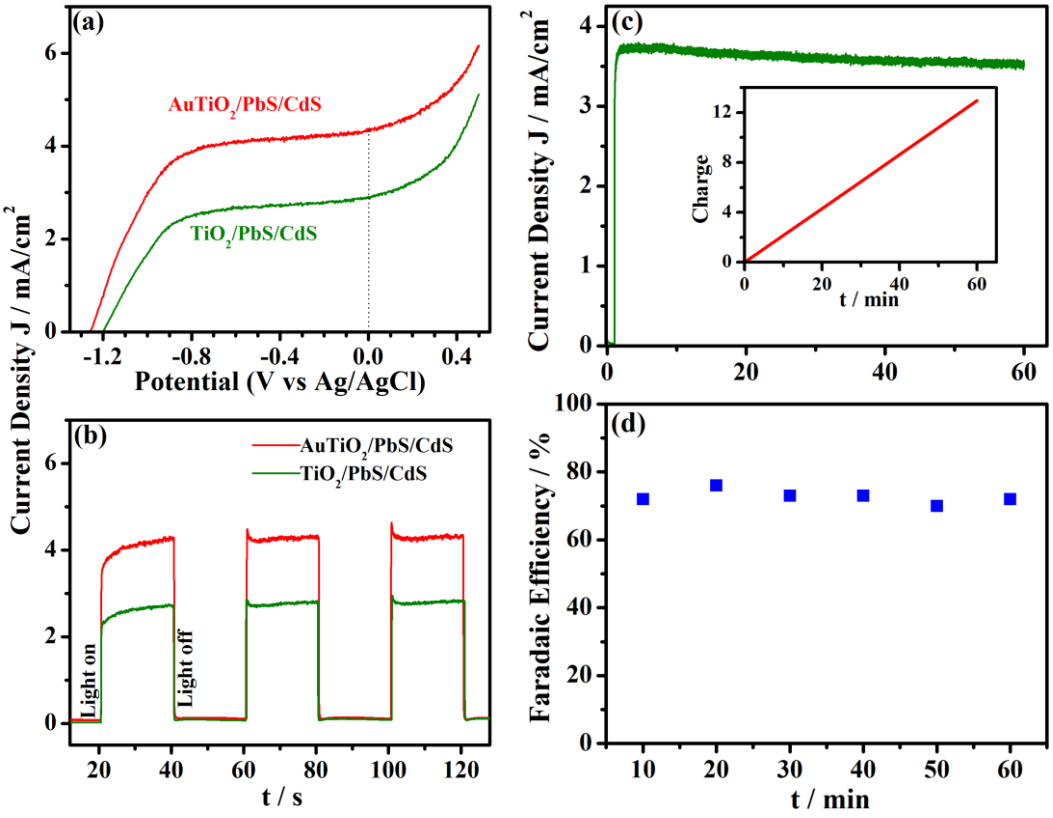

Figure 4.8: Photoelectrochemical performance of the $AuTiO_2$/PbS/CdS and TiO_2/PbS/CdS photoanode under one sun illumination. (a) j-V curves obtained under linear sweep voltammetry; (b) Chronoamperometry measurement at 0 V. (c) Chronoamperometry measurement shows the stability of photoanode for 1 h in the wired configuration. Inset shows the amount of charge

passed through the external circuit for 1 h. (d) Faradaic efficiency of the process calculated by comparing the amount of charge passed through the circuit and the amount of H_2 gas evolved. for every 10 min.

Figure 4.9 displays the H_2 evolution by the $AuTiO_2$/PbS/CdS in the wired configuration, and a linear increase in H_2 production represents the stable catalyst performance. However, under identical conditions, HER decreased dramatically to an order of magnitude with wired configuration (48 µmol/h) compared to the wireless configuration (490 µmol/h). In fact, the photoanode exhibited a photon to energy conversion (PEC) efficiency of 0.5 % in the wired configuration. Resistance associated with the external circuit, and the Pt foil used (against nano-Pt coated on the wireless configurations) is the two important reasons for the decrease in H_2 production in the wired configuration.

The total amount of charge passed through the external circuit, and the amount of H_2 evolved determined the Faradaic efficiency. The Faradaic efficiency of photoanode with respect to time is plotted in Figure 4.8d, and a steady efficiency of 72±2% was observed. This result reiterates that HER occurs at an order of magnitude higher under no applied bias in the wireless configuration. No significant H_2 generation was found with TiO_2/PbS/CdS photoanode in the wired configuration.

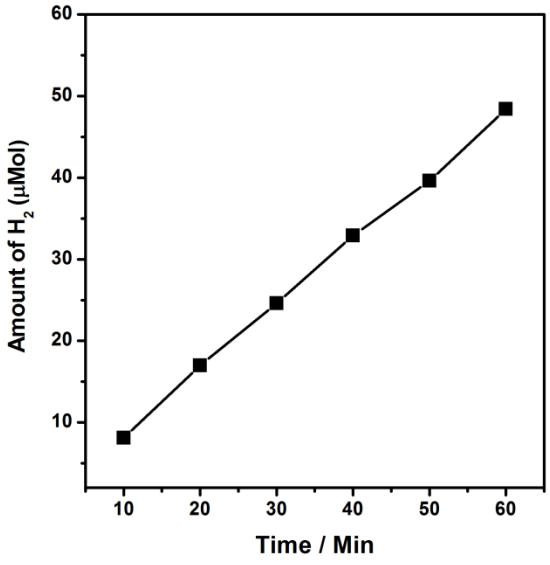

Figure 4.9: Solar driven hydrogen production with the $AuTIO_2$/PbS/CdS in the wired configuration at zero applied bias and the amount of H_2 gas evolved was measured by GC.

PIRET effect is expected to increase the incident photoelectron conversion efficiency (IPCE) in the case of $AuTiO_2$/PbS/CdS compared to TiO_2/PbS/CdS. The IPCE spectrum was measured for both photoanodes at no applied voltage, and the result is shown in Figure 4.10. An

introduction of the Au nanoparticles improved the IPCE action spectrum markedly in the entire wavelength range from 400 to 900 nm. Optical absorption spectrum of $AuTiO_2$/PbS/CdS (Fig. 4.10, blue trace) plotted fully supports the role of plasmon enhancement in IPCE. The IPCE at 450 nm was 27.4 % and 15.2 % for the photoanodes with and without Au nanoparticles,

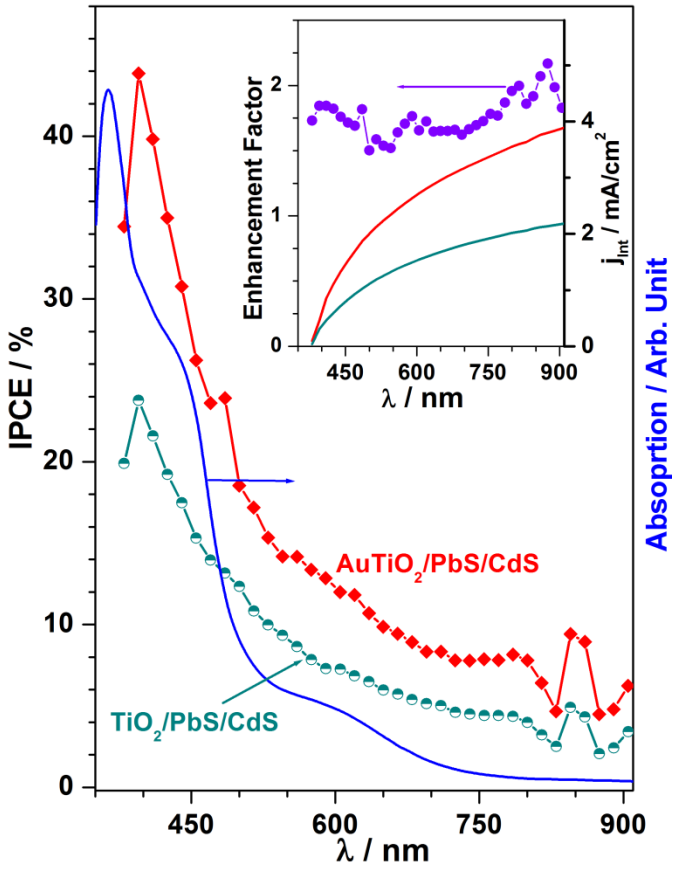

Figure 4.10: Wavelength dependent IPCE performance of the $AuTiO_2$/PbS/CdS and TiO_2/PbS/CdS photoanodes. Optical absorption of $AuTiO_2$/PbS/CdS photoanode is also plotted for correlation between IPCE and light absorption. Inset shows the IPCE enhancement of $AuTiO_2$/PbS/CdS over TiO_2/PbS/CdS. An enhancement factor of 1.7-2 was observed over the entire absorption regime reiterates the active PIRET role in improving the current and HER. Integrated current obtained from IPCE for both photoanodes are also given.

respectively. Critically, in the broadened nano gold plasmon absorption regime (500-700 nm), there is an improvement in IPCE with $AuTiO_2$/PbS/CdS compared to TiO_2/PbS/CdS. A good correspondence between IPCE and absorption spectrum is evident for $AuTiO_2$/PbS/CdS and fully supports the role of PIRET in enhancing the IPCE between 500 and 700 nm. Significant contribution to IPCE (3-9 %) from $\lambda > 800$ nm is also evident from the present results for both photoanodes, underscoring the near IR absorption. Integration of the IPCE spectrum over the

entire wavelength region is shown in Figure 4.9 (inset) leads to the total photocurrent of 3.9 and 2.2 mA/cm^2 for $AuTiO_2$/PbS/CdS and TiO_2/PbS/CdS, respectively. This is in good agreement with the values (4.3 and 2.7 mA/cm^2 for $AuTiO_2$/PbS/CdS and TiO_2/PbS/CdS, respectively) obtained in Fig. 4.8a. Inset in Figure 4.10 also shows the IPCE enhancement factor, which was obtained by dividing the IPCE value of Au-containing photoanode to that of without Au at a given wavelength. An overall increase in enhancement factor was observed at all wavelengths up to 900 nm. Enhancement factor increases between 1.7 and 2. Notably an enhancement factor of 2 was observed for PbS and near IR absorption regimes further supporting the effective conversion of high λ light, which is good correspondence with that of ref. 16.

4.3 Mechanism

Based on the H_2 generation and characterization results obtained, a possible working mechanism of light harvesting is suggested in Figure 4.11. The HRTEM and Raman spectral results (Fig. 4.3) reveal that the AuNPs is electronically integrated to the TiO_2 surface and the PbS/CdS QDs are deposited on the TiO_2 surface. Metal-semiconductor junction observed between Au and titania suggests the Schottky junctions, which helps in electron-hole pair separation. The shift in E_g band of titania to high wave number observed on Au deposition on TiO_2 in Raman underscores the electronic integration among them. Visible light absorption from the entire visible light spectrum by Au-SPR and CdS, near-IR by PbS, at various wavelength ensures the maximum light absorption; without Au, this is restricted only to the corresponding wavelength regime. IPCE measurements are shown in Figure 4.10 fully demonstrate the PIRET effect in the photoanode system with Au particles. The critical factor that increases the light absorption capacity of the photoactive material is due to the close spatial proximity of the QDs to the intensifying electric field surrounding the AuNPs in $AuTiO_2$/PbS/CdS; this is shown in Figure 4.10 with a VIBGYOR ellipsoid extending on all semiconductors.[20,21] The oscillating electric field thus generated enhance the photocurrent generation in photoanodes by transferring its energy to the surrounding chalcogenide and titania lattice. Due to the porous titania with gold particles anchored firmly on it, and the SILAR method employed for chalcogenide intercalation into those pores, gold is inevitably surrounded by one of the above components; it is evident from EDX chemical mapping given in Fig. 4.4. This factor ensures the gold nanoparticles efficiently transfer the energy through PIRET process and hence an overall increase in IPCE was

observed throughout the visible and NIR wavelength range. Indeed this factor is entirely missing without Au. Porosity with TiO_2 and SILAR method employed for PbS/CdS enhances the proximity of all components. As a result, the light absorption and electron-hole pair separation is also improved in the QDs, which leads to high catalytic activity with Au. The enhancement effect is attributed to the PIRET from the excited plasmonic NPs to the QDs.

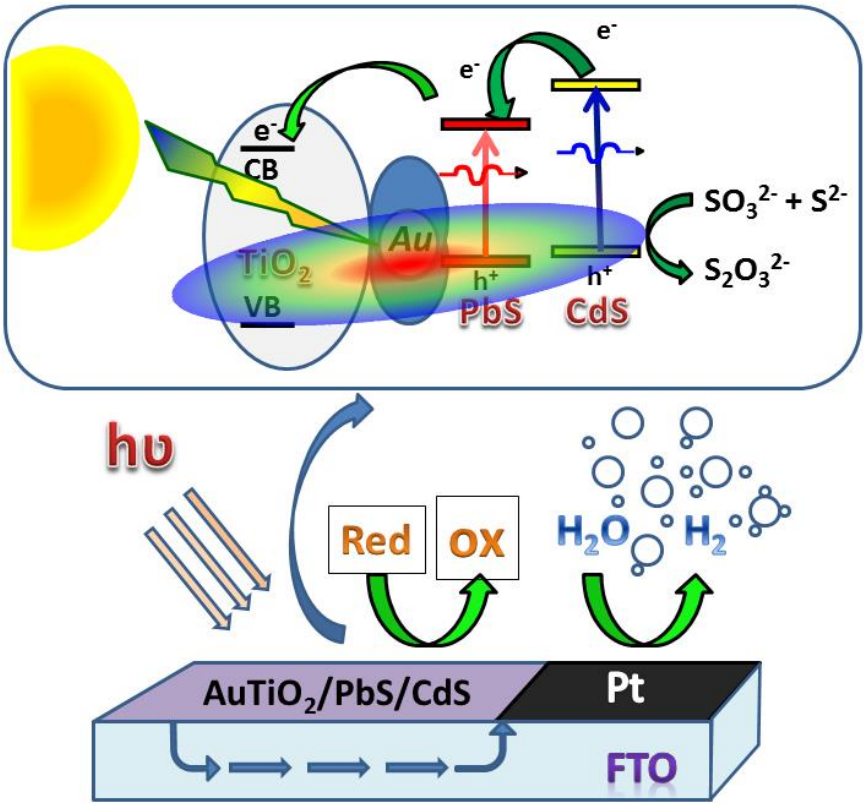

Figure 4.11. Schematic diagram for solar driven hydrogen evolution and the energy levels of different components. Au LSPR effect is represented by an ellipsoid.

4.4 Conclusion

In conclusion, an attempt has been made to network the known factors that positively enhance light absorption to charge carrier utilization in the present communication. Current research efforts focus on using the AuNPs as a plasmonic sensitizer along with PbS/CdS QDs for designing wireless photochemical cell at no applied potential. It is also demonstrated that quasi-artificial leaf in wireless configuration harvests the solar light and converts it to H_2 very efficiently than the wired configuration. Moist H_2 produced from the quasi-artificial leaf can be directly fed to applications, like a fuel cell. Generally, the electronic integration of the plasmonic

AuNPs and TiO_2 with QDs sensitization provides a new pathway for better solar light harvesting. Further improvement in the more light absorption capacity of photoanode and earth-abundant co-catalyst would make the wireless photochemical cell more cost effective. Increasing the gold content, but without compromising the particle size, is expected to increase photocurrent generation and hydrogen in the present system. Replacement of Au by cheaper SPR metal, such as Ag, is a potential method to make it more economical. Fine tuning the porosity of titania could help further to improve the SWS efficiency by distributing the various light absorption components and its integration with titania. Simultaneous efforts are required to systematically scale up the photoanode size and evaluate them for longer period of time for moving towards real-world applications.

It is also essential to develop the counterpart of the present photoanode system to utilize the holes for oxygen generation. This would make the system complete towards overall water splitting and without any sacrificial agents. However, consistent efforts are required towards this direction.

Part B: Quasi Artificial Leaf for Solar Hydrogen Generation with Earth Abundant Co-Catalyst

4.5 Introduction

The artificial photosynthetic system produces hydrogen via water splitting using solar energy, which can be collected directly or combine with CO_2 to form synthetic liquid fuels.[23] The water splitting reaction includes the water oxidation half reaction and proton reduction half reaction to generate O_2 and H_2 respectively. The water oxidation is a four electron process, requires 1.23 V and hence it is an energetically uphill reaction. For the efficient hydrogen production, the semiconductor usually coupled with a cocatalyst and a hole scavenger. Cocatalyst provides the active sites for the half reactions and highly reduces the photoexcited electron–hole pair recombination. Pt is the most well known cocatalyst for its lower overpotential towards hydrogen evolution reaction (HER) and chemically inert nature. However due to high cost and scarcity finding an alternative solution for cocatalyst made of inexpensive earth abundant material is highly necessary.

Quantum dots (QDs) has been used as sensitizer because of their high light absorption cross section and shape and size depended optical property. Generally upon illumination, the excited electron in the QDs transfer to the conduction band of semiconductor and the holes get oxidized by the redox electrolyte. The combination of a wide band gap semiconductor with QDs has been seen as an effective way to improve light absorption capacity in many systems such as photocatalytic water splitting and quantum dot sensitized solar cell (QDSSC). Another option to improve the light absorption of wide band gap semiconductor is to use plasmonic metal nanostructure.

In natural system, the reduction of proton takes place through Mn_4O_4 unit and many efforts has been contributed to mimic through inorganic chemistry.[24] Many molecular complexes of earth abundant element like Mo, Co, Ni have been developed for H_2 evolution.[25,26] This metal based molecular complex is used in homogeneous photocatalytic H_2 production by combining them with a photosensitizer. However it has been demonstrated that heterogeneous catalysts are having higher catalytic efficiency as compared to homogeneous catalysts. In the present study we prepared a non-precious Ni/Cu based alloy system and successfully incorporated into the

wireless photochemical device as cathode for H_2 evolution reaction. Nocera and coworker have reported an artificial photosynthetic device composed of Si solar cell as light absorbing material, with NiFeLDH as cocatalyst for H_2 evolution with high efficiency. However, across the globe, researchers used Pt or one of the metal as co-catalyst/cathode for hydrogen production. As such the efforts to produce new, efficient and low-cost co-catalysts are very rare and this area deserves good attention.

Herein we report a wireless photochemical device consists of TiO_2/PbS/CdS composite and NiCu as cocatalyst for photocatalytic hydrogen evolution in water under one sun condition. We focused on the electrocatalytic activity of NiCu catalyst and incorporation of those NPs on the photochemical device. Fermi level of electrocatalyst is an important parameter to understand the electrocatalytic and photocatalytic reaction, and efforts are directed towards understanding this aspect. To the best of our knowledge, such wireless photochemical device consisting of earth abundant catalyst with high efficiency it yet to be reported.

4.6 Results and Discussion

4.6.1 XRD

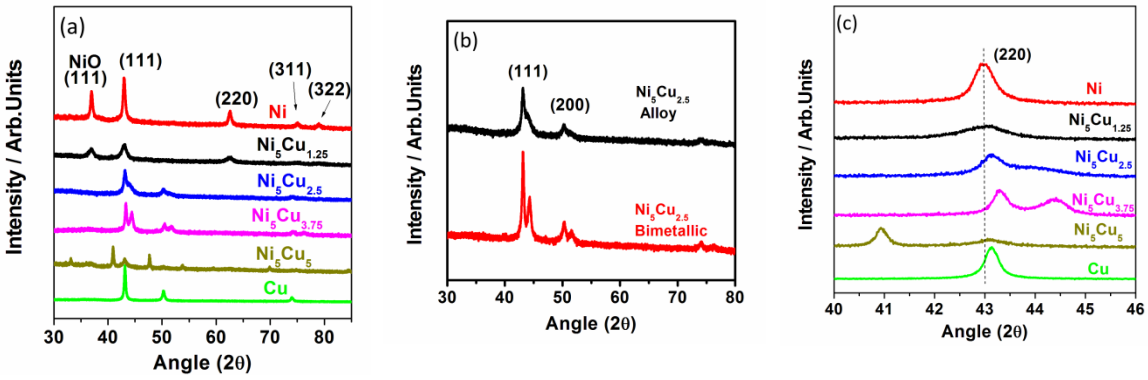

Figure 4.12. (a) XRD pattern of Ni-Cu nanoparticle with different stoichiometry (b) Difference in XRD pattern of $Ni_5Cu_{2.5}$alloy and $Ni_5Cu_{2.5}$ bimetallic forms. (c) Shift in the (220) plane of Ni to higher 2θ value after Cu incorporation.

The XRD pattern with different composition of NiCu (alloy and bimetal) has been shown in Figure 4.12a. The Ni without any Cu shows a diffraction peak around $2\theta = 37^0$ corresponds to (111) plane of NiO. The intensity of (111) plane of NiO decreases significantly in $Ni_5Cu_{1.25}$ and finally disappears in $Ni_5Cu_{2.5}$ and $Ni_5Cu_{3.75}$. The diffraction peak (111) and (200) in $Ni_5Cu_{2.5}$ corresponds to the characteristic features of an alloy. However the same diffraction peak

in $Ni_5Cu_{3.75}$ corresponds to the characteristic features of a bimetallic structure. In this two composition there were no diffraction lines corresponds to XRD features of pure Ni and Cu. As shown in Figure 4.12c, the diffraction peak for (200) planes of Ni becomes broader and a gradual shift in peak towards higher 2θ value was observed with increase in Cu concentration. A different XRD pattern was observed with Ni_5Cu_5 and some of the features are identified to be from individual Ni and Cu NPs; however we are not able to assign few other peaks and thorough analysis is required. Based on the XRD results it is clear that an alloy of NiCu can be obtained with a certain composition of 5:2.5 molar ratios of Ni and Cu. However it does not form an alloy with higher concentration of Cu. We also synthesized the $Ni_5Cu_{2.5}$ bimetallic NPs and Figure 4.12b shows the difference in XRD pattern of $Ni_5Cu_{2.5}$ for alloy and bimetallic NPs.[27]

4.6.2 X-ray photoelectron spectroscopy

To further validate the nature of surface XPS analysis was performed for the $Ni_5Cu_{2.5}$ alloy and $Ni_5Cu_{2.5}$ bimetallic NPs. As expected, the alloy form shows significant amount of metallic Ni features and the binding energy corresponds to 852 eV (Figure 4.13a) represents the metallic nature of Ni. However the binding energy at 855 eV in Ni 2p spectra as shown in Figure 4.13a corresponds to the presence of hydroxide species on the surface of NP and it is in

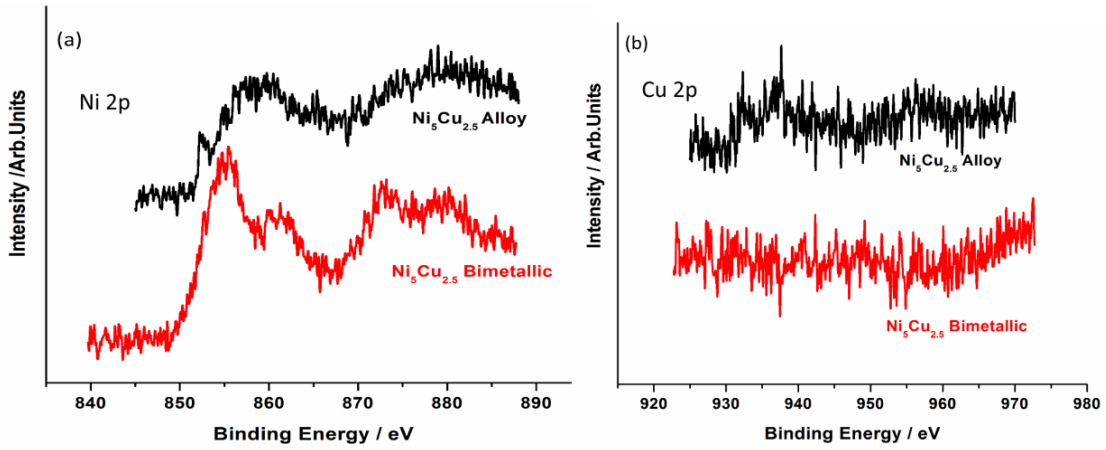

Figure 4.13:. XPS results of $Ni_5Cu_{2.5}$ for (a) Ni 2p and (b) Cu 2p core levels in in alloy and bimetal form.

good agreement with literature reports.[28] The XPS spectra shown in Figure 4.13b indicates the presence of metallic Cu and hydroxide species on the surface of alloy NP. However bimetallic

$Ni_5Cu_{2.5}$ shows the NiO features on the surface of NP as evident from the Ni 2p spectra, shown in Figure 4.13a, where as we have not observed any Cu features on the surface as shown in Figure 4.13b. The absence of any Cu on the surface in bimetallic $Ni_5Cu_{2.5}$ allow the Ni atoms to oxidise easily, where as in alloy form the adjacent Cu atom hindered the formation of oxide.

4.6.3 Ultraviolet photoelectron spectroscopy

To probe electron density near Fermi level, we carried out ultraviolet photoelectron spectroscopy (UVPES) and the complete spectra is given in Fig. 4.14. The Fermi level of electrocatalyst is a characteristic features direct indicates the catalytic activity.[29]. Qualitatively, from the valence band spectra shown in Figure 4.14, we observed that the $Ni_5Cu_{2.5}$ alloy sample has higher electron density near the Fermi level as compared to $Ni_5Cu_{2.5}$ bimetallic sample. This higher electron density is a direct indication of more metallic character of alloy (than bimetal) on the surface, which is in good agreement with XPS results. Moreover, the work function of alloy appears to be lower by 0.5 eV than that of bimetal, as shown in Figer 4.14b. The above observations indicates that the alloy NPs has higher potential for proton reduction as compared to bimetallic form.

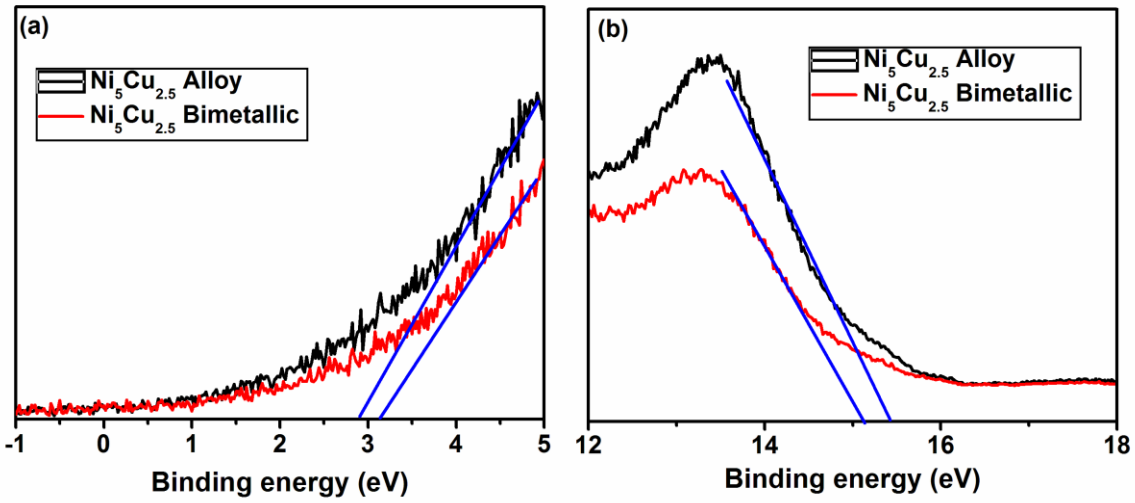

Figure 4.14: UVPES plots for the $Ni_5Cu_{2.5}$ alloy and $Ni_5Cu_{2.5}$ bimetallic sample.

4.6.4 Electrochemically-measured HER activity

The electrocatalytic activity of different composition of NiCu materials was studied in N_2 saturated 0.5 M H_2SO_4 using three electrode system. All the catalyst was coated on a glassy carbon electrode and the amount of catalyst loading was 5 µg cm^{-2} in each experiment. As shown in Figure 4.15a, Ni exhibits very little HER activity. However the Cu incorporation into Ni accelerate the HER activity and with high concentration of Cu again the activity decreases. The polarization curve recorded on $Ni_5Cu_{2.5}$ alloy shows an over potential of 280 mV to achieve a current density of 10 mA cm^{-2}. On the contrast, $Ni_5Cu_{2.5}$ bimetallic shows an over potential of

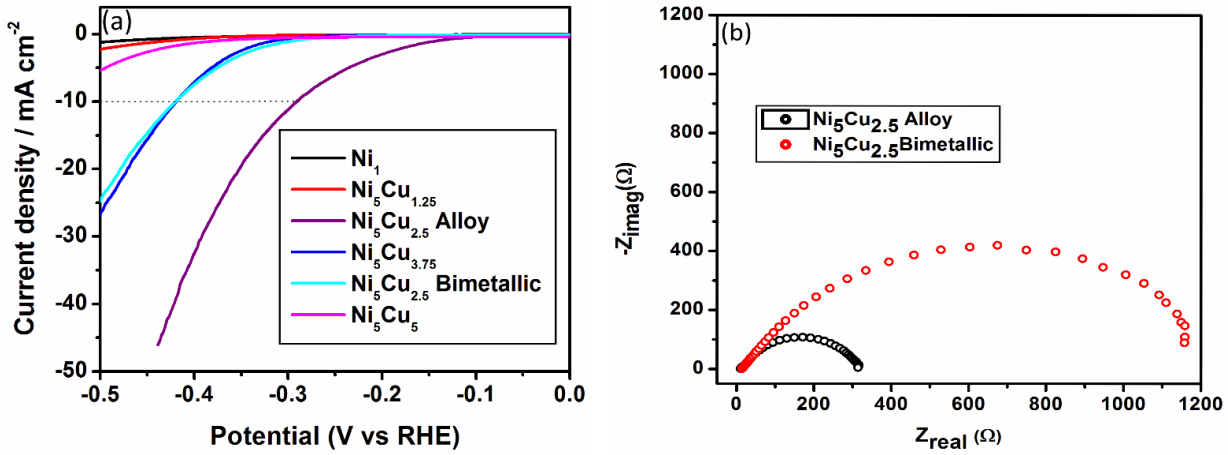

Figure 4.15 (a) HER polarization curve obtained on different catalyst (b) Electrochemical impedance spectroscopy data were collected in 0.5 M H_2SO_4 at an HER over potential of 130 mV vs RHE.

400 mV to achieve a current density of 10 mA cm^{-2}. The significant improvement in catalytic activity for $Ni_5Cu_{2.5}$ alloy is also evident from the positive shift in the onset potential to -130 mV vs RHE as compared to bimetallic form. Nevertheless the lower charge transfer resistance for $Ni_5Cu_{2.5}$ alloy as compared to its bimetallic form (shown in Figure 4.15b) indicates an enhanced electrocatalytic performance. Hence the chemical coupling between Ni and Cu which is more prominent in alloy can provide a less resistance pathway for electron transfer and consequently enhance the HER activity on its surface. The higher proton reduction current of $Ni_5Cu_{2.5}$ alloy confirming the critical role of HER catalyst in our artificial leaf device.

4.6.5 Photocatalytic hydrogen evolution

Hydrogen production activity for all composites has been studied systematically with Ni-Cu as a cocatalyst. All the photoanodes have been prepared, as described in chapter 2 (sec. 2.3.2). The synthesis of NiCu catalyst (experimental section 2.2.5) and the complete device fabrication has been explained in chapter 2 (sec.2.3). The photochemical cell immersed in the Na_2S/Na_2SO_3 electrolyte solution and illuminated with one sun light from the front side of the FTO plate. The photocatalytic H_2 evolution was studied for various compositions of NiCu NPs and the results are shown in Fig 4.16. A H_2 production rate of only 0.2 mL/h was observed with Ni and the activity increases to 0.5 mL/h after the small amount of Cu incorporation in $Ni_5Cu_{1.25}$. There is a huge improvement in activity with further addition of Cu incorporation at $Ni_5Cu_{2.5}$. Nevertheless, the activity decreases with further increase in Cu-content in $Ni_5Cu_{3.75}$ and Ni_5Cu_5. Hence an optimum concentration of Cu in NiCu is required to achieve better H_2 evolution. As shown in Figure 4.16, the wireless photochemical cell exhibited highly enhanced H_2 production rate of 312 µmol h^{-1} (corresponds to 7 mL H_2 h^{-1}) and a PEC of 3.6 % with $Ni_5Cu_{2.5}$ alloy. The photochemical device produces a large amount of hydrogen gas bubbles with $Ni_5Cu_{2.5}$ alloy which can be observed with the naked eyes. A movie recorded (Movie 2.avi) is shown in the attached CD.

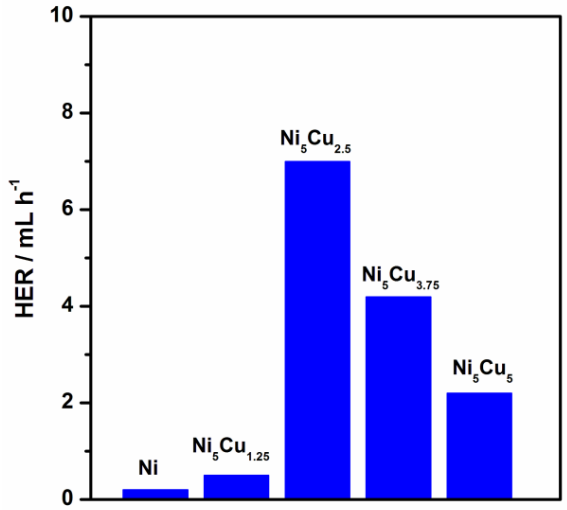

Figure 4.16: Photocatalytic H_2 evolution from QuAL device made from TiO_2/PbS/CdS and different composition of Ni-Cu.

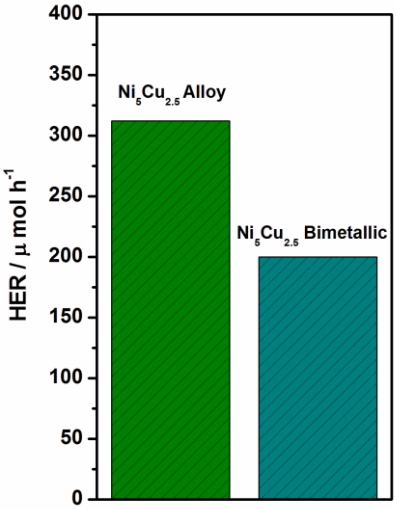

Figure 4.17: Hydrogen production of TiO_2/PbS/CdS with Ni-Cu alloy and Ni-Cu bimetallic NPs as cocatalyst.

Moreover the photocatalytic activity of the device, with same Ni and Cu composition in bimetallic form exhibited 200 µmol h^{-1} (corresponds to 3.5 mL H_2 h^{-1}) and a PEC of 2.5 % (Fig 4.17). The decrease in activity with the bimetallic NPs is attributed to the formation of oxide features on the surface as evident from the XPS result. However the alloy NPs shows both metallic and oxide features on the surface. This result is in agreement with our electrochemical HER studies, where $Ni_5Cu_{2.5}$ alloy is more catalytically active than bimetallic $Ni_5Cu_{2.5}$. The $Ni_5Cu_{2.5}$ alloy NPs exhibits spherical morphology and an average particles size of 15 nm was observed in TEM studies are shown in Figure 4.18. Inter-plananr distance of 0.195 nm observed supports the formation of alloy as shown in Figure 4.17 c.

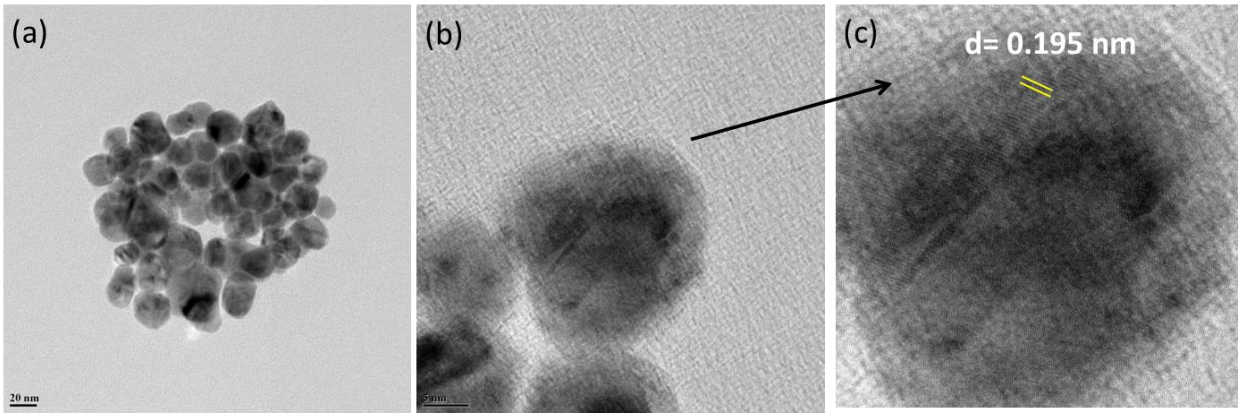

Figure 4.18: (a) TEM image of $Ni_5Cu_{2.5}$ alloy NPs (b) high resolution TEM image of a typical $Ni_5Cu_{2.5}$ alloy NP and (c) enlarge area of the NP shown in b.

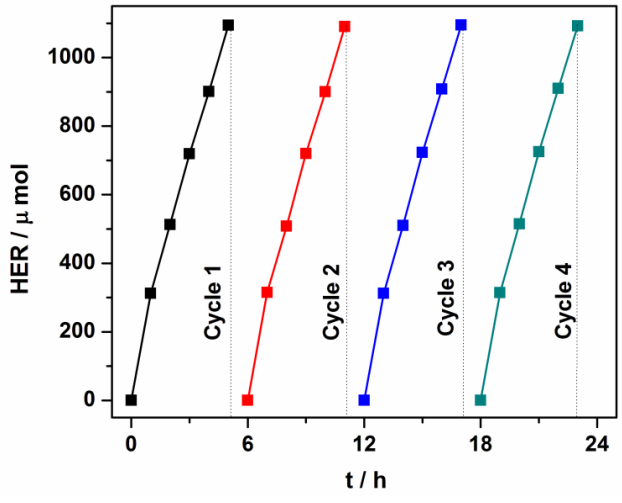

Figure 4.19: Photostability of the wireless device with TiO_2/PbS/CdS and Ni-Cu alloy is demonstrated by performing the experiment for four cycles.

The stability of the photochemical device for H_2 generation with $Ni_5Cu_{2.5}$ alloy was studied and the amount of gas evolved was measured by GC and the results are shown in Figure 4.19. The device produced 4.4 mmol of H_2 after 20 hour of continuous irradiation and no significant decrease in activity was observed. This indicates the robustness of the present artificial photosynthetic device under visible light irradiation.

4.7 Conclusion

In conclusion, a visible light driven wireless photochemical cell using TiO_2/PbS/CdS as light harvesting material and NiCu as cocatalyst for photocatalytic H_2 evolution at no applied potential was successfully developed and demonstrated. We demonstrate that the nature of cocatalyst surface control the HER kinetics; indeed a tight control of surface nature could enhance the the photocatalytic activity further. In other words, arrangement of atoms on the co-catalyst seems to affect the activity to a large extent. UVPES studies reveals that the Fermilevel upshifting of $Ni_5Cu_{2.5}$ alloy makes it an efficient cocatalyst as compared to its bimetallic form. Further careful investigations by different methods can provide a rational guidelines to improve solar light harvesting efficiency.

Part C: Photocatalytic and Cocatalytic Behavior of MoS_2-mild Oxidized Graphite (MoS_2-mGO) Nanocomposite on a TiO_2/PbS/CdS Quasi Artificial Leaf for Solar Hydrogen Production: Dual Role of MoS_2-mGO.

4.8 Introduction

In recent years, great efforts have been made to develop carbon free clean energy fuels, especially hydrogen energy. The photocatalytic hydrogen production through water splitting has been considered as the most powerful tool for production of clean renewable energy. However there is a long road ahead before it becomes a reality for practical application. In this regard, the construction of artificial photosynthetic device is highly desirable in transforming solar light in to hydrogen fuel.[2] In natural system, the leaf converts the solar energy in to chemical energy by water splitting and CO_2 reduction to carbohydrates through photosynthesis process. The primary step for water splitting in natural system involves the absorption of light by photosystem-II and subsequent separation of electron hole pair. The holes in the photosystem-II oxidize water in to oxygen with the release of four electrons and four protons. Hydrogen generated is stored in the form of NADPH from ferredoxin-$NADP^+$ reductase (nicotinamide adenine dinucleotide phosphate) in photosystem-I, where ferredoxin provides the active sides for reduction reaction. A wireless current flows from the photosystem-II to photosystem-I during the overall process.[23] Inspired by the natural photosynthesis process, in this current thesis, we have designed a QuAL, which consists of TiO_2/PbS/CdS as light absorption unit and MoS_2-mGO composite as co-catalyst for H_2 evolution over a FTO plate. The role of ferredoxin is simulated by the co-catalyst. Unlike natural system, a photocurrent flows from the light absorption unit to co-catalyst unit, through the FTO plate.

The efficiency of hydrogen production depends on the extent of light absorption, charge separation, charge migration, and charge utilization.[30] Many precious metals, such as Pt, Rh and Pd have been used as a catalyst for photocatalytic hydrogen evolution reaction (HER).[31] However, it is vital to find the cost effective co-catalyst, made up earth abundant material for any practical utility. Molybdenum disulfide (MoS_2) attracts huge attention as a potential catalyst in electrocatalytic HER due to its reactive sulfur edges sites.[32,33] However bulk MoS_2 shows poor catalytic activity towards HER due to its inherent and highly stacked MoS_2 layers, which significantly decreases the amount of exposed edges sites.[34] Generally two methods are used to

improve the catalytic activity of MoS_2: (1) chemical exfoliation, to increase the number of active sites; (2) improve the charge transport by incorporating graphene or graphene oxide (GO) layers suitably. The presence of oxygen functional groups on the surface of GO, generally, facilitated the nucleation and subsequent growth of nanoparticles.[35] Recently many efforts have been made to synthesize MoS_2/GO composites by hydrothermal, microwave and solvothermal methods, which exhibit high catalytic activity as compared to only MoS_2.[36] However the MoS_2/GO composites show photocatalytic HER only in the presence of a sensitizer or when it combines with another semiconductor like TiO_2, where it provides the active sites for HER, and it does not absorb solar light on its own.[37,38] Wu et al have reported a nanoscale p-n junction of p-type MoS_2 and n-type nitrogen doped reduced graphene oxide (NRGO) composites for solar hydrogen generation and demonstrates H_2 production activity of 24.8 μM $h^{-1}g^{-1}$.[39] Herein, we report a visible light active exfoliated MoS_2-mGO composite, which mainly acts as a co-catalyst in our QuAL device. The photochemical cell generates 83 μmol h^{-1} of H_2 with MoS_2-mGO (3:1), which corresponds to a photon to energy conversion efficiency (PEC) of 0.94 % under one sun illumination.

4.9 Results and discussion

4.9.1 Optical properties of MoS_2-mGO composite

Synthesis details of MoS_2-mGO are given in chapter 2 (sec. 2.2.6) The optical property of MoS_2 and MoS_2-mGO composite were characterized by UV-Vis spectra. The indirect band gap of bulk MoS_2 is 1.2 eV and the direct band gap of exfoliated MoS_2 is 1.9 eV. As shown in Figure 4.20, MoS_2 shows an absorption pattern corresponding to indirect band gap between Γ and the middle of the Brillouin zone between Γ and K.[39,40] On intercalation of mGO into MoS_2, 1:1 and 2:1 composites shows two absorption peaks at 480 and 670 nm. A big change in absorption occurs at the ratio of 3:1 and it shows a broad absorption centered around 700 nm. Up on increasing the ratio to 4:1, again the absorption shifts and features are observed at 425 and 610 nm. The absorption peak observed at high energy (between 425 and 480 nm) in MoS_2-mGO (1:1, 2:1 and 4:1 and bulk MoS_2) are arising due to direct transition from deep valence band to conduction band. Only the MoS_2-mGO (3:1) composite shows a strong absorption peak in the visible region (at ~700 nm). Inset in Fig. 4.20 shows the colour change associated with different composition of MoS_2-mGO. It is worth noting that, only the 3:1 (4:1) composition shows the

intense (pale) blue colour, which is in good agreement with the UV-Vis spectra. It is very likely that 3:1 MoS_2-mGO ratio is at optimum to exhibit maximum exfoliation and it is speculated that the absorption at 700 nm may be due to plasmon absorption. However, this needs to be confirmed by other methods.

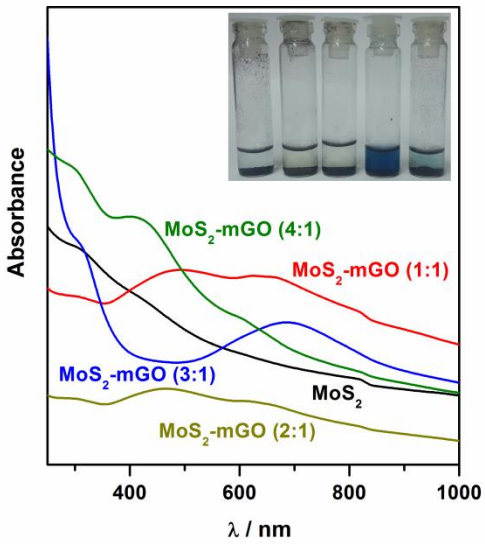

Figure 4.20: UV-Visible absorption of the dispersion of MoS_2-mGO composites in water.

The origin of the intense blue colour may also arise due to strong direct inter-band transition at the K point, as suggested in ref.40. As a result of direct band gap nature of exfoliated MoS_2, photon energy greater than the band gap energy can be absorbed and emit different frequency of light. The monolayer MoS_2 is known to exhibit strong photoluminescence (PL) due to its direct band gap nature, whereas bulk MoS_2 is PL inactive.[41] As shown in Figure 4.21, five to six time enhancements in PL intensity was observed in MoS_2-mGO composite compared to MoS_2 at an excitation wavelength of 414 nm. Enhancement in intensity is attributed to the surface recombination of charge carriers due to the quantum confinement phenomenon of few layers of MoS_2. Figure 4.22 shows the excitation wavelength dependent PL spectra of MoS_2-mGO (3:1), which confirms the polydisperse nature of MoS_2.[42] Up on increasing the excitation wave length from 370 to 430, a red shift in PL spectra was observed. Excitation wavelength of 390 nm begins to broaden the emission and it fully broadens at an excitation of 410 nm. Further increase in excitation wavelength decreases the broadening and a low intensity sharp feature was observed at 430 nm excitation. These observations reiterate the polydisperse nature with exposure of

different facets of MoS_2 and leads to excitation dependent emission spectra. However, further careful studies along with life time measurements are likely to provide more details.

4.9.2 XRD

The crystal characteristic of MoS_2 and MoS_2-mGO composite is shown in Figure 4.23 . As for the pure MoS_2, XRD results shows two peaks at 2θ = 24.0° and 33.8°. After mGO intercalation the new peaks appears at a 2θ value of around 14.5, and 58° corresponds to (002) and (008) planes of hexagonal MoS_2.[42] 002 and 008 facets demonstrates the exfoliation occurs along the z-axis, as expected. Hence the basal plane of hexagon (only sulfide ions present) and the atoms along the z-axis (sulfide and Mo) would be exposed and available for reaction. The diffraction pattern observed at 2θ of 26.4° for all MoS_2-mGO composites corresponds to (002) planes of mGO, which is similar to graphite features and indicating low degree of oxidation.[43]

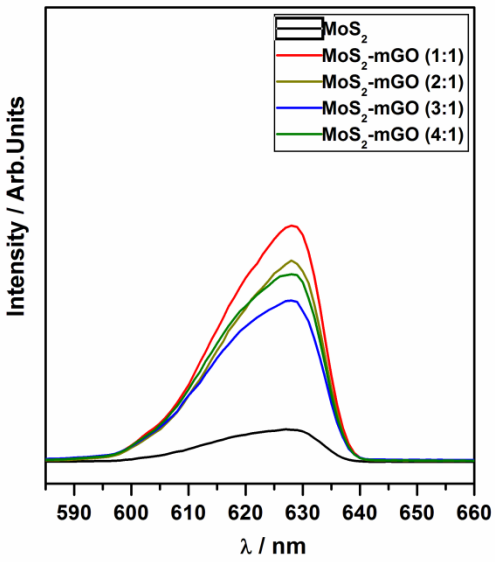

Figure 4.21: Photoluminescence spectra of MoS_2-mGO composites at an excitation wave length of 414 nm.

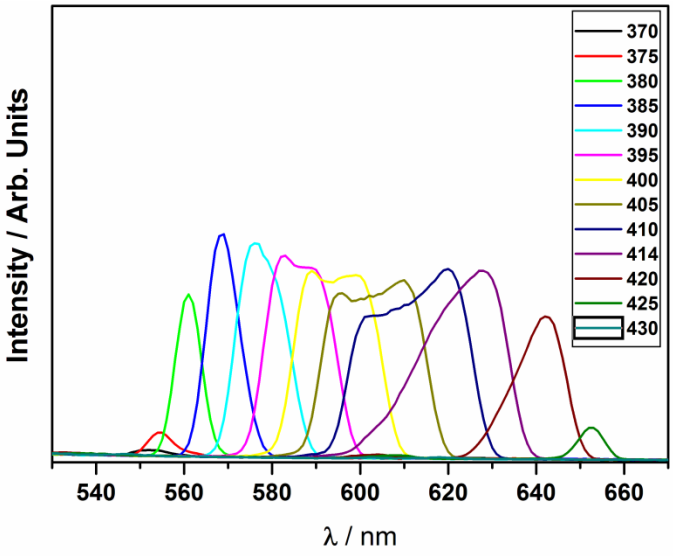

Figure 4.22: Excitation dependent PL spectra of MoS_2-mGO (3:1) indicate the polydisperse nature of the composite.

Moreover the peak broadening observed at 2θ = 14.5 and 33.8° in MoS_2-mGO composite demonstrates the low stacking with smaller crystallite size, and suggesting a low crystallinity of MoS_2.[35] It is to be noted that both the components exhibiting broad peaks underscores the stacking of very few layers and nano-crystallinity.

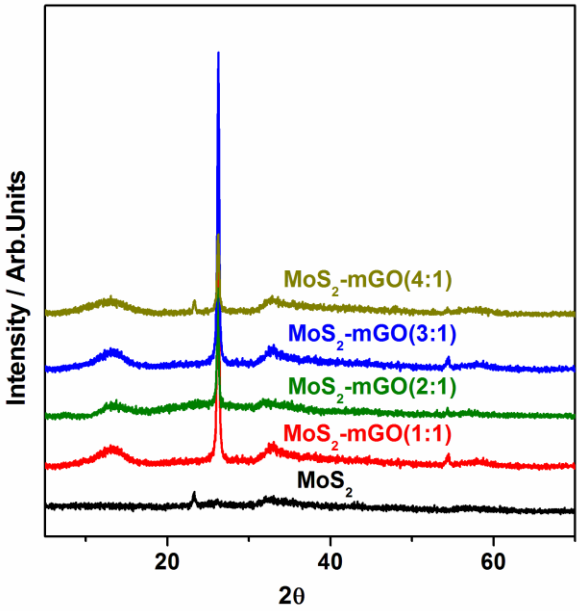

Figure 4.23: XRD characterization of different composition of MoS_2-mGO composite indicates the exfoliated nature of MoS_2.

4.9.3 Raman spectroscopy

The Raman spectra of MoS_2 and MoS_2-mGO (3:1) composite is shown in Figure 4.24.. Two peaks appear at 372 and 401 cm^{-1} corresponds to the E^1_{2g} and A_{1g} vibrational modes of 2H phase of hexagonal MoS_2, respectively.[34] The E^1_{2g} mode ascribed to the opposite vibration of two S atoms with respect to Mo and A_{1g} mode ascribed to the out of plane vibration of two S atoms. However, for MoS_2-mGO (3:1) the corresponding peak appears at 375 and 401 cm^{-1} respectively. It is well known that the decrease in difference between E^1_{2g} and A_{1g} vibrational modes indicates the decrease in MoS_2 layers or less stacking.[35] Hence the decrease in frequency difference in MoS_2-MGO composite as compared to MoS_2 confirms that the composite composed of few-layer features of MoS_2 and indicates the interaction between MoS_2 and mGO. Moreover the additional Raman band at 281 cm^{-1} in MoS_2-MGO composite associated with E_{1g} vibrational modes of 1T MoS_2.[44] The 2H phase is the most thermodynamically stable state and generally found in natural MoS_2, where two layers of S-Mo-S are sharing edges and forms MoS_6 trigonal prism structure as shown in Figure 4.26. In contrast, 1T phase is less stable where a single S-Mo-S layer sharing edges forming MoS_6 octahedral structure and it is mostly found after chemical exfoliation of bulk MoS_2.[45]

Figure 4.25 shows the vibrational mode of graphite oxide (GO) in the raw mGO and MoS_2-mGO (3:1) composite. The D band appears at 1350 cm^{-1} corresponds to A_{1g} symmetry and G band appears at 1581 cm^{-1} corresponds to E_{2g} symmetry of sp^2 hybridized carbon atoms. The peak intensity ratio of D to G band (I_D/I_G) for mGO and MoS_2-mGO(3:1) composite were estimated to be 0.56 and 0.19, respectively. The decreased I_D/I_G ratio for the composite material as compared to raw mGO indicates that significant reduction has taken place on mGO due to hydrothermal synthesis process. Furthermore, a large blue shift of 7 cm^{-1} in D and G band of mGO was observed in MoS_2-mGO (3:1) composite as a result of electron transfer to MoS_2.[38]

4.9.4 XPS

The chemical state and composition of the MoS_2 and MoS_2-mGO composite was investigated by XPS and the results are shown in Fig. 4.26. , Two prominent peaks for Mo $3d_{5/2}$ (227.8 eV) and $3d_{3/2}$ (231.2 eV) core levels observed are characteristic of 4+ oxidation state (Figure 4.27a).[46] No other peaks corresponding to MoO_3 or MoO_4^{2-} was observed, which might result due to aerial oxidation of the catalyst .

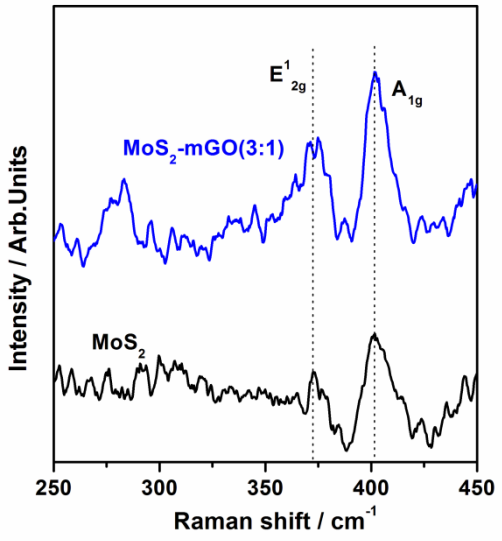

Figure 4.24: Raman spectra of MoS_2 and MoS_2-mGO (3:1) show the characterstic E^1_{2g} and A_{1g} band.

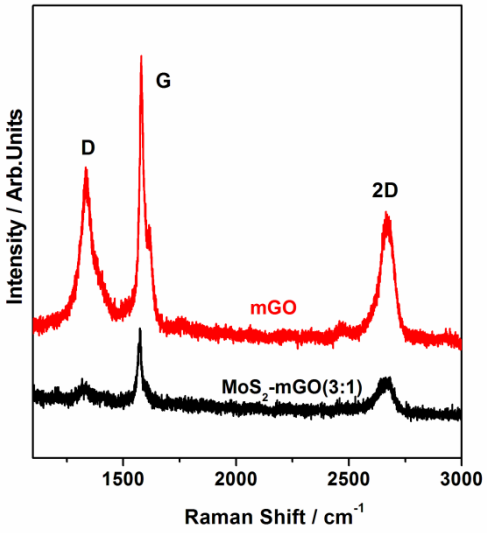

Figure 4.25: Raman spectra of mGO and MoS_2-mGO (3:1) shows the characteristic D, G, and 2D band.

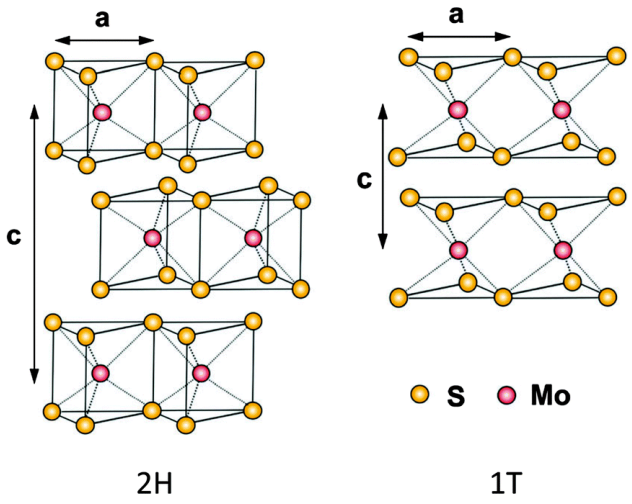

Figure 4.26: Schematic illustration of the 2H and 1T phase of MoS_2. (Reproduced with permission from RSC Publishers).

A broad peak appearing at 225 eV is due to S 2s core level. S 2p core level results are shown in Fig. 4.26b. The doublet appears at binding energy of 160.7 and 161.7 eV (Figure 4.27 b) corresponding to the $2p_{3/2}$ and $2p_{1/2}$ lines of MoS_2. In addition to the sulfide features, a peak at 168 eV is observed for MoS_2-mGO suggesting the presence of SO_4^{2-} species, which might originate from H_2SO_4 employed in the preparation of mGO. A thorough washing of the composite again removed the feature to a large extent, hinting the sulfate is an impurity feature present only on the surface.

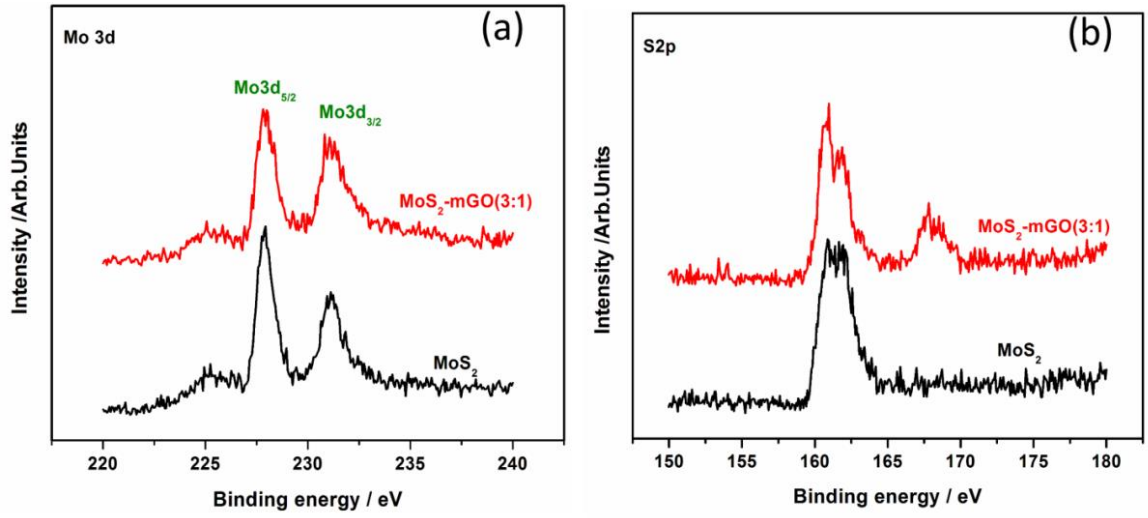

Figure 4.27: XPS spectra of (a) Mo3d and (b) S2p of MoS_2 and MoS_2-mGO (3;1) composite.

4.9.5 TEM

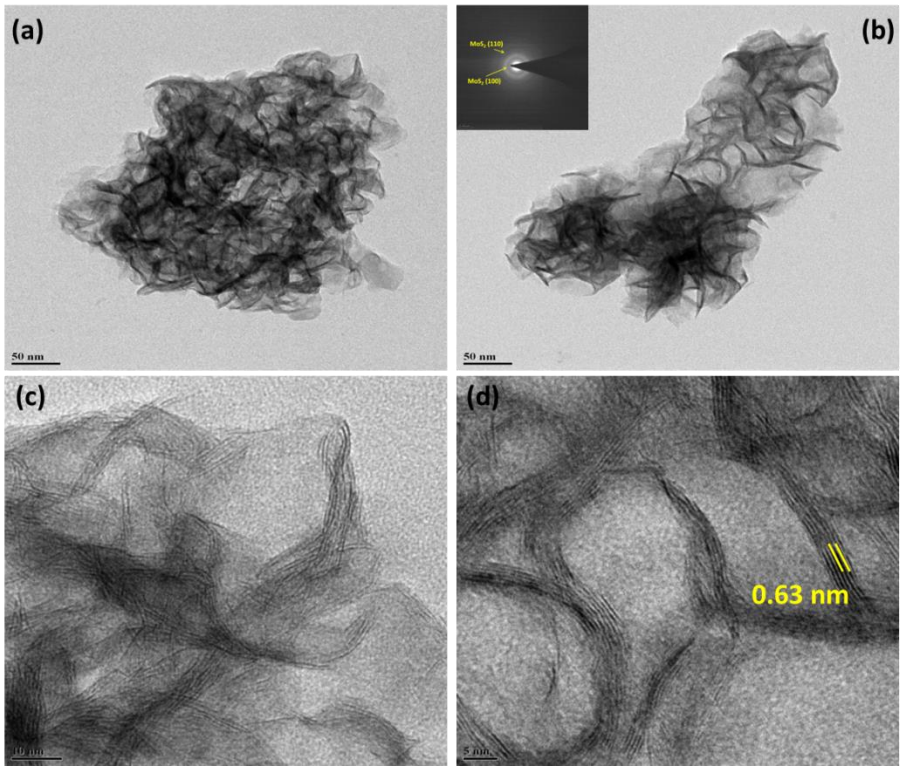

Figure 4.28: TEM images of (a) MoS_2 and (b-d) MoS_2-mGO (3:1) composite.

The morphology of the MoS_2-mGO composite was further investigated by TEM and the results are shown in Figure 4.27. As shown in Figure 4.28a, the MoS_2 nanosheets are aggregated together in free MoS_2. However in MoS_2-mGO the MoS_2 nanosheets are homogeneously distributed (or exfoliated) on the surface of mGO(Figure 4.28b). The nature of the nanosheets in MoS_2-mGO was further confirmed by SAED pattern (inset in Figure 4.28b), where the two separated diffraction rings corresponds to (100) and (110) planes of MoS_2.[47] No diffraction spot was observedfor mGO and this can be due to either low content or weak scattering power of mGO. Figure 4.28c shows the HRTEM image of MoS_2 where more stacking of MoS_2 nanosheets was observed. Furthermore, lattice fringes with interlayer spacing of 0.63 nm was observed from the HRTEM image (Fig 4.28d), indicating the MoS_2 nanosheets mainly composed of few-layers (a maximum of 4 layers) MoS_2.

4.9.6 Electrocatalytic HER Activity of MoS_2-mGO composites

The electrocatalytic activity towards HER was investigated on glassy carbon electrode and measured in a three electrode system in N_2 saturated 0.5 M H_2SO4 solution (see sec. 2.6.2).

The polarization curves in a cathodic potential window of 0 to -0.3 V vs RHE is shown in Figure 4.29. MoS_2 alone exhibits a very low HER activity with an onset potential of 200 mV and low cathodic current density. However a large enhancement in HER activity was observed after mGO incorporation. The polarization curve recorded on MoS_2-mGO (3:1) shows an over potential of 113 mV to achieve a current density of 10 mA cm^{-2}. In contrast, MoS_2-mGO (1:1) and MoS_2-mGO (2:1) shows an over potential of 143 and 132 mV respectively to achieve a current density of 10 mA cm^{-2}.

The significant improvement in catalytic activity for MoS_2-mGO (3:1) can be also seen from the positive shift in the onset potential to -38 mV vs RHE as compared to only MoS_2. Moreover the MoS_2 and MoS_2-mGO (4:1) shows almost similar HER activity and this is due to higher MoS_2 content in the composite, which results in less exfoliation. The large enhancement in cathodic current density with very low onset potential in MoS_2-mGO (3:1) composite may arise from the synergetic effect of exposed edge sites and the more conductive pathway for charge carriers provided by the mGO. Furthermore, the less charge transfer resistance of MoS_2-mGO (3:1) composite as compared to MoS_2 indicates the enhanced electrocatalytic performance in the composite material (Figure 4.30).

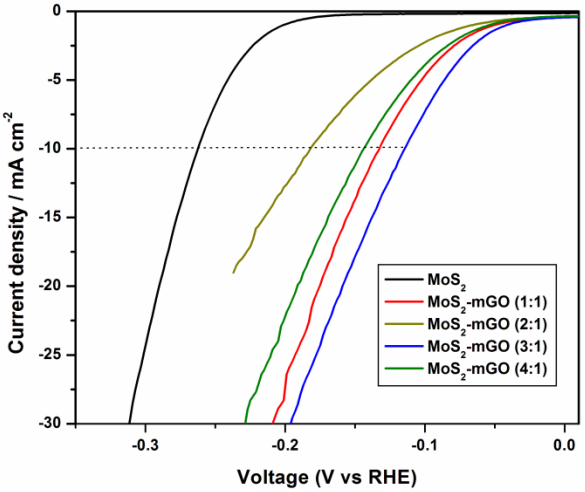

Figure 4.29: Electrochemical measurement of MoS_2-mGO composites in a cathodic potential window.

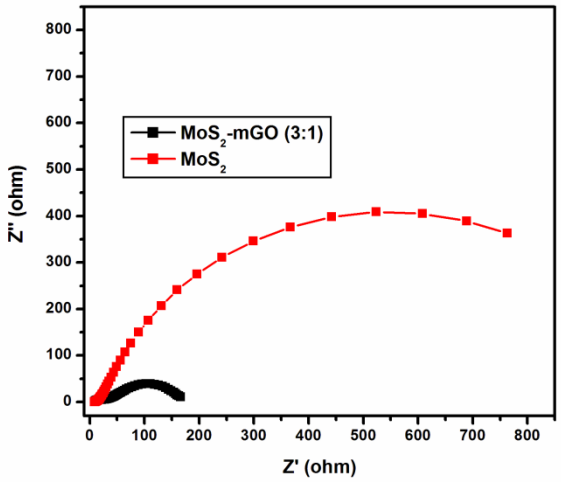

Figure 4.30: Nyquist plot of MoS_2 and MoS_2-mGO (3:1) composite.

4.9.7 Photocatalytic HER activity of MoS_2-mGO composites

TiO_2/PbS/CdS photochemical cell was constructed and evaluated for solar H_2 production. The thickness as well as total area of the photoactive material is 8 µm and 10 x 10 mm^2 respectively over FTO plate. MoS_2 and MoS_2-mGO composites was deposited as a strip (4 x 10 mm^2) on the other half of the FTO. The photocatalytic H_2 evolution experiment was conducted by immersing the overall photochemical cell in the Na_2S/Na_2SO_3 electrolyte and illuminated under one sun condition (AM 1.5 filter, 100 mW/cm^2). The rate of H_2 evolution from the photochemical cell with different MoS_2-mGO cocatalyst is shown in Figure 4.31. Bulk MoS_2 show very negligible photocatalytic hydrogen evolution of 17 µmol/h. The TiO_2/PbS/CdS photochemical cell with MoS_2-mGO (3:1) exhibited the highest H_2 evolution rate of 84 µmol/h and a PEC of 0.94%. A movie recorded under similar experimental condition with MoS_2-mGO (see Movie3.avi in the attached CD) demonstrates the generation of H_2 bubbles from the cocatalyst surface. The total amount of photoactive material deposited on FTO plate over 1 cm^2 area is 2 mg. A linear extrapolation of the above results could lead to hydrogen production of 84 mMol/h.g over an area of ~23x23 cm^2. In the same manner the rate of H_2 evolution with MoS_2-mGO (1:1), MoS_2-mGO (2:1) and MoS_2-mGO (4:1) was measured to be 56, 60 and 18 µmol/h, respectively. The improved H_2 generation in 3:1 composition is due to the combined effect of more visible light absorption and highly exposed HER active edge sites in the composite material, which are in good agreement with our UV-Visible and electro catalytic HER studies.

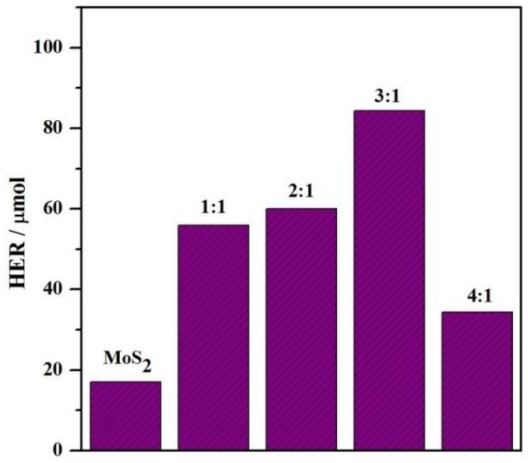

Figure 4.31: Photocatalytic H_2 evolution in TiO_2/PbS/CdS photochemical cell containing MoS_2-mGO as cocatalyst

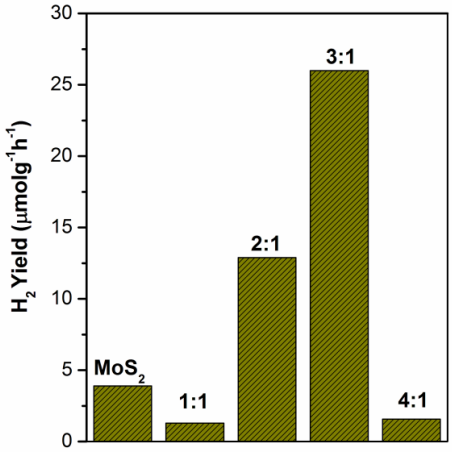

Figure 4.32: Photocatalytic H_2 evolution in powder catalyst.

To further gain insight in to the photocatalytic behavior of bare MoS_2-mGO, all the MoS_2-mGO composite were tested in aqueous Na_2S/Na_2SO_3 solution under one sun illumination. The 3:1 composition shows the highest activity of 26 µmol $g^{-1}h^{-1}$ due to more visible light absorption as evident from the UV-Visible spectra (Figure 4.32). The decrease in activity in 1:1 composition as compared to MoS_2 is mainly because of the 50% mGO content, which hinders the light absorption in the composite material.

4.10 Mechanism of photocatalytic HER

As in many literature reports, S atoms at the edges of MoS_2 is responsible for catalytic activity. Yugang et al. has demonstrated that the improved catalytic activity of exfoliated MoS_2 is mainly because of the presence of unsaturated S atoms present in MoS_2.[48] The unsaturated S atoms at the edges of MoS_2 have a strong affinity toward H^+ adsorption in the solution, which can easily reduce to H_2 by electrons. More over nanoscale MoS_2 is visible light active due to its direct band gap nature. The MoS_2-mGO (3:1) showed high catalytic activity due to more exposed edge sites with unsaturated S atoms and also harvest visible light photons for photocatalytic HER. Figure 4.33 shows the schematic representation for photocatalytic H_2 evolution in TiO_2/PbS/CdS phtochemical cell with MoS_2-mGO (3:1) as cocatalyst.

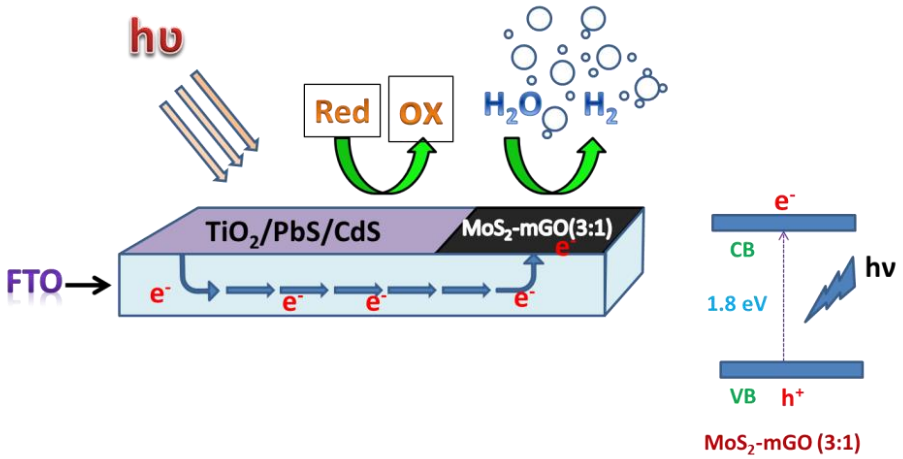

Figure 4.33: Schematic representation for photocatalytic H_2 evolution in QuAL device.

Under visible light irradiation, photogenerated electrons from PbS and CdS QDs transferred to TiO_2 conduction band and finally injected in to the FTO surface. These photogenerated electrons flow through the FTO surface and reach the active sides of MoS_2-mGO (3:1) catalyst, where it

reduced the adsorbed H^+ ions to H_2. Moreover, the electron density further increases on the MoS_2-mGO (3:1) catalyst surface due to its ability to harvest visible light photons, which boost the H_2 production efficiency.

4.11 Conclusion

In summary, a novel MoS_2-mGO catalyst was developed, which acts both as a cocatalyst and photocatalyst for H_2 production in QuAL device. Decent catalytic activity of the composite material with 3:1 composition could be ascribed to the combined effect of exposed edges sites on the catalyst surface as well as the ability to absorb visible light photons. A detailed electrocatalytic study of the catalyst and correlating the results with photocatalytic H_2 evolution from QuAL device can provide us with further insight in to the design of cost effective artificial photosynthetic architectures. It is also essential to find a way for better deposition of catalyst on the QuAL device, which will make the present system even more effective towards H_2 production. Reduction in charge carrier recombination on the surface of MoS2 could further improve the photocatalytic activity.

References

1. A. J. Bard, G. M. Whitesides, R. N. Zare, and F. W. McLafferty, *Acc. Chem Res.* **1995**, 28, 3 .
2. S. Y. Reece, J. A. Hamel, K. Sung, T. D. Jarvi, A. J. Esswein, J. J. H. Pijpers, and D. G. Nocera *Science.*, **2011**, 334, 645-648.
3. A. J. Bard, and M. A. Fox, *Acc. Chem. Res.* **1995**, 28, 141-145.
4. Z. Zou, J. Ye, K. Sayama, and H. Arakawa, *Nature.* **2001**, 414, 625-627.
5. P. A. Bharad, K. Sivaranjani, and C. S. Gopinath, . *Nanoscale*. **2015**, **7**, 11206-11215 .
6. S. Rajaambal, K. Sivaranjani, K. and C. S. Gopinath, . *J. Chem. Sci.* **2015**, 127, 33-47.
7. F. E. Osterloh, . *Chem. Soc. Rev.* **2013**, 42, 2294-2320.
8. A. P. Alivisatos, *Science* **1996**, 271, 933-937.
9. P. Sheng, W. Li, J. Cai, X. Wang, X. Tong, Q. Cai and C. A. Grimes*J. Mater. Chem. A* **2013**, 1, 7806-7815 .
10. S. Mubeen1, J. Lee1, N. Singh, S. Kramer, G. D. Stucky and M. Moskovits, *Nature Nanotech.* **2013**, 9, 2341-2347.
11. A. A. Melvin, K. Illath, T. Das, T. Raja, S. Bhattacharyya and C. S. Gopinath, *Nanoscale*, **2015**, 7, 13477-13488.
12. Y. Li, H. Wang, Q. Feng, G. Zhou, G. & Z.-S. Wang, *Ene. Envir. Sci.* **2013**, 6, 2156-2165.

13. S. K. Cushing, J. Li, F. Meng, T. R. Senty, S. Suri, M. Zhi, M. Li, A. D. Bristow and N. Wu, *J. Am. Chem. Soc.*, **2012**, 134, 15033-15041
14. K. K. Patra, K. K. & C. S. Gopinath, *ChemCatChem* **2016**, 8, 3294-3311 .
15. J. Li, S. K. Cushing, P. Zheng, T. Senty, F. Meng, A. D. Bristow, A. Manivannan, and N. Wu. *J. Am. Chem. Soc.* **2014**, 136, 8438-8449.
16. R. Trevisan, P. Rodenas, V. Gonzalez-Pedro, C. Sima, R. S. Sanchez, E. M. Barea, I. Mora-Sera, F. Fabregat-Santiago, S. Gimenez, *J. Phys. Chem. Lett.* **2013**, *4*, 141-146 .
17. R. Zanella, S. Giorgio, C. R. Henry, & C. Louis, . *J. Phys. Chem. B* **2002**, 106, 7634-7642.
18. M. A. Mahmoud, M. Chamanzar, A. Adibi, & M. A. El-Sayed, . *J. Am. Chem. Soc.* **2012**, 134, 6434-6442 .
19. V. Subramanian, E. E. Wolf, & P. V. Kamat, *J. Am. Chem. Soc.* **2004**, 126, 4943-4950 .
20. Z. W.Seh, S. Liu, M. Low, S. Y. Zhang, Z. Liu, A. Mlayah, *Adv. Mater.* **2012**, 24, 2310-2314.
21. Sivaranjani, S. RajaAmbal, T. Das, K. Roy, S. Bhattacharyya and C. S. Gopinath, *ChemCatChem*, **2014**, 6, 522-530.
22. K. Sivaranjani, S. Agarkar, S. B. Ogale, & C. S. Gopinath , *J. Phys. Chem. C.* **2012**, 116, 2581-2587 .
23. D. G. Nocera. The artificial leaf. *Acc. Chem. Res*., **2012**, 45, 767–776.
24. D. Mersch, C. Y. Lee, J. Z. Zhang, K. Brinkert, J. C. Fontecilla-Camps, A. William Rutherford, and E. Reisner. *J. Am. Chem. Soc.*, **2015**, 137, 8541−8549.
25. E. S. Andreiadis, P. A. Jacques, P. D. Tran, A. Leyris, M. C. Kerlidou, B. Jousselme, M. Matheron, J. Pecaut, S. Palacin, M. Fontecave and V. Artero. *Nature Chem.*, **2013**, 5, 48-53.
26. H.W. Liang , S. Bruller , R. Dong, J. Zhang, X. Feng and K. Mullen. *Nature Commun.*, **2015**, 6, 7992.
27. Li , M. Lua, K. Aragaki , M.Koike , Y. Nakagawa , K. Tomishige . *Appl. Catal., B,* **2016**, 192, 171–181.
28. S. Velu, K. Suzuki, M. Vijayaraj, S. Barman and C.S. Gopinath, *Appl. Catal. B – Environ.*, **2005** , 55, 287-299.
29. W. Bi, L. Zhang, Z. Sun, X. Li, T. Jin, X. Wu, Q. Zhang, Y. Luo, C. Wu and Y. Xie. *ACS Catal*. **2016**, 6, 4253−4257.
30. A. Kudo and Y. Miseki, *Chem. Soc. Rev.*, **2009**, 38, 253–278.
31. K. Maeda and K. Domen, *J. Phys. Chem. Lett*. **2010**, 1, 2655–266.
32. J. D. Benck, T. R. Hellstern, J. Kibsgaard, P. Chakthranont, and T. F. Jaramillo, *ACS Catal.*, **2014**, 4, 3957−3971.
33. J. Kibsgaard, Z. Chen, B. N. Reinecke and T. F. Jaramillo, *Nature Mater*., **2012**, 11, 936-969.
34. A. B. Laursen, S. Kegnæs, S. Dahl and Chorkendorff , *Energy Environ. Sci.*, **2012**, **5**, 5577-5591.
35. X. Zheng, J. Xu, K. Yan, H. Wang, Z. Wang, and S. Yang, *Chem. Mater.* **2014**, 26, 2344−2353.
36. H. L. Wang, J. T. Robinson, G. Diankov, H. J. Dai, *J. Am. Chem. Soc.* **2010**, 132, 3270–3271.

37. S. Min and G. Lu *J. Phys. Chem. C*, **2012**, 116, 25415−2542.
38. U. Maitra, U. Gupta, M. De, R. Datta, A. Govindaraj, and C. N. R. Rao *Angew. Chem. Int. Ed.* **2013**, 52, 13057 –13061.
39. F. Meng, J. Li, S. K. Cushing, M. Zhi, and N. Wu, *J. Am. Chem. Soc.* **2013**, 135, 10286−10289.
40. M. Ye, D. Winslow, D. Zhang, R. Pandey and Y. K.Yap**,** *Photonics,* **2015**, *2*, 288-307.
41. G. Eda, H. Yamaguchi, D. Voiry, T. Fujita, M. Chen and M. Chhowalla, *Nano Lett*., **2011**, 11, 5111–5116.
42. D. Gopalakrishnan, D. Damien, and M. M. Shaijumon, *ACS Nano*, **2014**, 8, 5297–5303.
43. T. S. Sahu and S. Mitra, *Sci. Rep*, **2015***,* 12571.
44. H. Y. He, *Sci. Rep*., **2017**, DOI: 10.1038/srep45608.
45. X. Huang, Z. Zeng and H. Zhang, *Chem. Soc. Rev.*, **2013**, 42, 1934–1946.
46. Y. Wang, D. Chen, X. Yin, P. Xu, F. Wu, and M. He, *ACS Appl. Mater. Interfaces*., **2015**, 7, 26226−26234.
47. A. Xie, M. Sun, K. Zhang, W. Jiang, F. Wu and M. He, *Phys. Chem. Chem. Phys.*, **2016**, 18, 24931-24936.
48. Y. Sun, F. Alimohammadi, D. Zhang, and G. Guo, *Nano Lett.* **2017**, 17, 1963−1969.

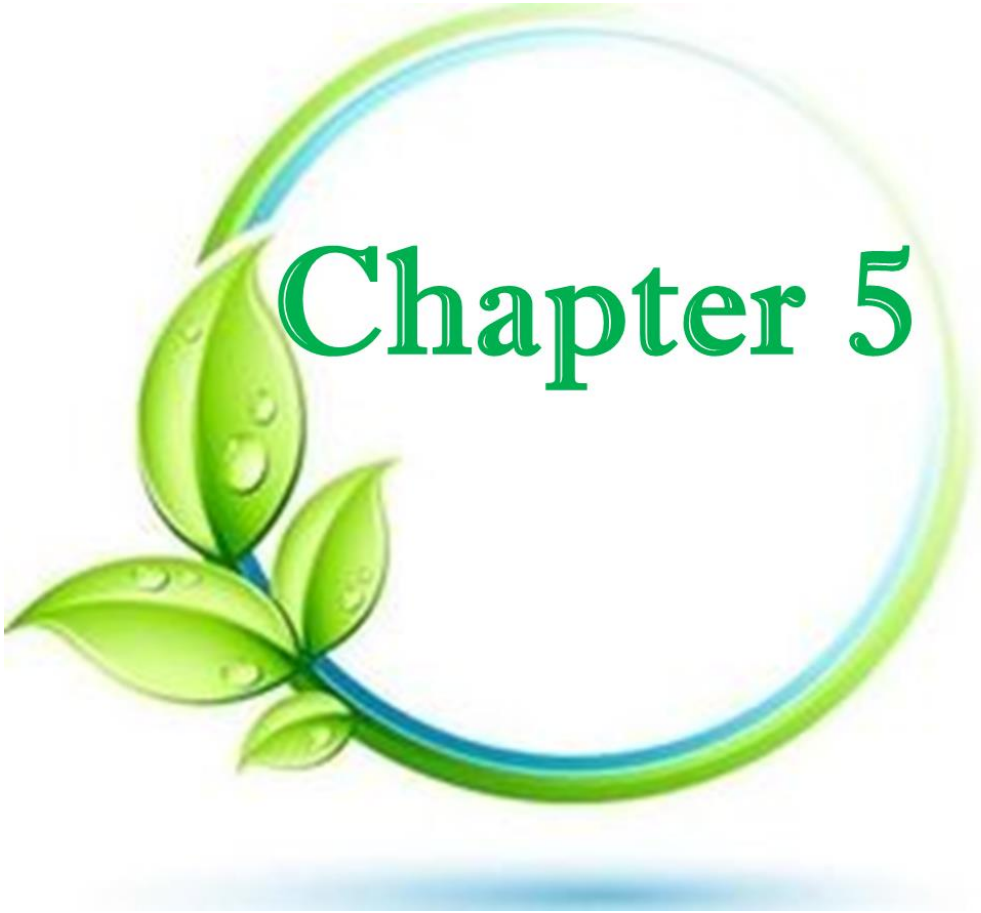

Conclusions and Future Scope of the Work

Conclusions and Future Scope of the Work

This chapter summarizes the present thesis work and describes the possible future scope .

Chapter 1 presents a brief introduction to photocatalytic water splitting reactions and the importance of transition metal oxide semiconductors. It describes the scope of the plasmonic metal-semiconductor composites in solar light harvesting. It gives explanation on the use of plasmonic metal NPs like Au, Ag and its structure-activity correlations. It also describes the importance of cocatalyst in SWS reaction and the electrochemical characterization technique to understand the charge transfer mechanism at the cocatalyst-electrolyte interface. Finally this chapter gives a brief introduction in to quasi artificial leaf approach for solar hydrogen production by transferring the knowledge of electrocatalysis in to photocatalysis.

Chapter 2 mainly describes the synthesis methods involved in materials preparation. The synthesis of plasmonic metal-TiO_2 composites, which shows predominant absorption of visible light regime for improved solar water splitting, has been discussed. It also describes the synthesis of different aspect ratio of AuNR for SWS application. The complete device fabrication and synthesis of different components of QuAL has been discussed in this chapter.

Chapter 3A deals with predominant absorption of entire visible light regime by using more than one plasmonic metal on titania for improved solar water splitting. It is to be emphasized that the electronic integration among the constituent components is the key aspect for better solar light harvesting, apart from absorption of wide wavelength range of sunlight. Fermi level equilibration between metal and titania, and Schottky junction formation is an important aspect and a part of electronic integration. The strong electronic interaction between Ag and Au, and with TiO_2 is evident from its electron rich character. Electronic factor seems to be responsible for the high rate of hydrogen production. We suggest the integration of one or two more different components suitably to improve the light absorption as well as to enhance the SWS activity.

Chapter 3B describes the utilization of the red-green-blue (RGB) and near IR photons for solar hydrogen evolution (SHE) in a single plasmonic nanocomposite. Here we demonstrate the use of $AgTiO_2$ (AgT) decorated with Au nanorods (AgT-AuNR) to enhance the absorption of entire visible light and limited near IR wavelength range in the sunlight for SHE from photocatalytic water splitting reaction. The longitudinal plasmon resonance of AuNR in AgT-AuNR induces SHE between 550 and 800 nm, whereas TiO_2-AuNR or AgT shows no activity in this wavelength range. The key aspect of achieving the high photocatalytic activity of AgT-AuNR in the solar spectrum is the electronic integration among metal NPs as well as with TiO_2, and the heterojunctions among them. This is reiterated again in this section. Gold nanorod also exhibits field effect and further enhances light harvesting. Here we observed that the absolute amount of energy harvested only from near IR photons is low, however when combined with high energy visible light photons within one sun conditions, it shows a multiplier effect rather than a simple additive effect. How can we improve the absorption of small amount of UV as well as significant amount of near IR photons could lead to further improvement in activity.

Chapter 3C describes the role of localized surface plasmons (LSPs) on the efficiency of dye sensitized solar cell (DSSC), when the plasmonic gold nanoparticles (Au NPs) of size less then 5 nm directly attached to TiO_2 surface as compared to the widely reported simple physical mixture of Au and TiO_2. Herein, using 4μm-thick and well-interconnected Au-TiO_2 as photo anode, a power conversion efficiency of 7.2 % was achieved, giving an enhancement of 25% in power conversion efficiency (PCE) as compared to only TiO_2. It is proposed that if can we increase the Au-content, while retaining the gold distribution but without agglomeration, a significant improvement in SWS could be achieved. New synthesis methods are needed in this direction.

Chapter 4 is divided in to Part A, Part B and Part C. Chapter 4A describes a wireless device based on quasi-artificial leaf concept (QuAL), comprising Au on porous TiO_2 electrode sensitized by PbS and CdS quantum dots (QD), was demonstrated to show sustainable solar hydrogen (490±25 μmol/h (corresponds to 12 ml H_2 h^{-1}) from ~2 mg of photoanode material coated over 1 cm^2 area with aqueous hole (S^{2-}/SO_3^{2-}) scavenger. A linear extrapolation of the above results could lead to hydrogen production of 6 L/h.g over an area of ~23x23 cm^2. A direct coupling of all components within themselves enhances the light absorption in the entire visible

and NIR region and charge utilization. Further improvement in the light absorption capacity of photoanode and earth-abundant co-catalyst would make the wireless photochemical cell more cost effective. Increasing the gold content, but without compromising the particle size, is expected to increase photocurrent generation and hydrogen in the present system. Replacement of Au by cheaper SPR metal, such as Ag, is a potential method to make it more economical. Fine tuning the porosity of titania could help further to improve the SWS efficiency by distributing the various light absorption components and its integration with titania. Simultaneous efforts are required to systematically scale up the photoanode size and evaluate them for longer period of time for moving towards real-world applications. It is also essential to develop the counterpart of the present photoanode system to utilize the holes for oxygen generation. This would make the system complete towards overall water splitting and without any sacrificial agents. However, consistent efforts are required towards this direction.

As a continuation of Chap. 4A, efforts have been directed to synthesize new and cheap co-catalysts. Chapter 4B describes a QuAL device with TiO_2/PbS/CdS composite and NiCu as new cocatalyst for viable solar hydrogen production. The device generates efficient hydrogen production activity of 7 mL/h with $Ni_5Cu_{2.5}$ alloy, which corresponds to a photon to energy conversion efficiency (PEC) of 3.6% under one sun illumination. The electrocatalytic activity of NiCu catalyst displays 10 mA cm^{-2} current density at a overpotential of 280 mV vs RHE. For the first time we used spectroscopic technique like XPS, UVPES, combined with electrocatalytic studies and correlating the results with photocatalysis which gives a new pathway to design better solar light harvesting architectures. However, how to increase the activity of co-catalyst should be addressed, so that a cheap alternative to Pt could be possible soon.

Chapter 4C describes the use of a novel multifunctional MoS_2/mildly oxidized graphite (mGO) elctrocatalyst as well as photocatalyst on a QuAL device composed of TiO_2/PbS/CdS for solar hydrogen production. The device generates hydrogen production activity of 83 µmol $h^{-1}$with MoS_2-mGO (3:1), which corresponds to a photon to energy conversion efficiency (PEC) of 0.94 % under one sun illumination. The enhanced catalytic performance by mGO intercalation can be attributed to the more number of exposed active sites, visible light active and superior conductivity of MoS_2-mGO composite. In contrast to the better activity expected from the present 2D MoS2-mGO composite, somewhat low activity was observed. However, there is scope to improve the activity by increasing the interaction among the components.